TAMPEREEN TEKNILLINEN YLIOPISTO
TAMPERE UNIVERSITY OF TECHNOLOGY

OTTO-VILLE MESKANEN

FLOW-INDUCED NOISE IN ELEVATOR LANDING DOOR

Master of Science Thesis

Supervisor: Prof Reijo Karvinen
Examiner: Prof Pentti Saarenrinne
Examiner and topic approved by the
Faculty Council of the Faculty of
Engineering Sciences
on 31st May 2017

ABSTRACT

OTTO-VILLE MESKANEN: Flow-Induced Noise in Elevator Landing Door
Tampere University of Technology
Master of Science Thesis, 87 pages, 3 Appendix pages
May 2018
Master's Degree Programme in Mechanical Engineering
Major: Fluid Dynamics
Supervisor: Prof Reijo Karvinen
Examiner: Prof Pentti Saarenrinne
Keywords: Elevator landing door, Fire labyrinth, CFD, Noise measurement, Leakage flow

Stack effect is a phenomenon that is potential especially in high-rise buildings generating a significant high pressure difference between the elevator shaft and the outdoors. This will force the air to flow through the fire labyrinths of the elevator landing doors.

In this thesis, the object was to investigate flow-induced noise in the fire labyrinths. The aim was to locate the noisy structures by means of experiments and to produce a development proposal. In addition, the target was to experimentally investigate the leakage flow rate up to a differential pressure of 300 Pa across the landing door and to examine the suitability of various turbulence models for estimating the leakage flow rate by CFD simulation.

The theory section focuses on the basic concepts of noise and on various common cases generating noise by gas flow. Further, the governing equations of fluid flow, as well as turbulence models and near-wall treatments, are presented to understand the basis of flow simulation.

The landing door was not processed in the laboratory as a whole, but small sections, subassemblies, were constructed from different parts of the fire labyrinths. The 1/3-octave band measurements were performed in the door laboratory of KONE Corporation in Hyvinkää. Estimates of the flow rate and the sound power radiating from the whole door was derived based on the measurements.

The door under consideration creates noise that is accompanied by pure tones. Such narrowband components are considered to be highly disturbing human hearing perception. By modifying the structure of the fire labyrinth, a pure tone was eliminated and the sound power level of the door decreased by 5 dB. CFD simulation proved to be a useful tool for estimating leakage flow rate through the fire labyrinths.

TIIVISTELMÄ

OTTO-VILLE MESKANEN: Hissin tasonoven virtausmelu
Tampereen teknillinen yliopisto
Diplomityö, 87 sivua, 3 liitesivua
Toukokuu 2018
Konetekniikan koulutusohjelma
Pääaine: Virtaustekniikka
Ohjaaja: Prof. Reijo Karvinen
Tarkastaja: Prof. Pentti Saarenrinne
Avainsanat: hissin tasonovi, labyrinttitiiviste, virtauslaskenta, melumittaus, vuotovirtaus

Korkeissa rakennuksissa on mahdollista, että ulko- ja sisäilman lämpötilaeron, nosteen sekä ilmanvaihdon yhteisvaikutuksesta syntyy merkittävän suuri paine-ero hissikuilun ja ulkoilman välille. Tämä ilmiö (engl. *stack effect*) aiheuttaa vuotovirtauksen hissin tasonovien labyrinttitiivisteiden lävitse.

Tässä työssä tavoitteena oli tutkia virtauksen aiheuttamaa melua hissin tasonoven labyrinttitiivisteissä. Päämääränä oli löytää meluisat rakenteet kokeellisesti ja esittää kehitysehdotus rakenteiden hiljentämiseksi. Lisäksi tavoitteena oli kokeellisesti tutkia oven vuotomäärää 300 Pa paine-eroon asti sekä tutkia eri turbulenssimallien soveltuvuutta vuotovirtauksen arvioimiseksi virtaussimuloinnilla.

Teoriaosuudessa keskitytään melun peruskäsitteisiin ja erilaisiin yleisiin tapauksiin, joissa kaasuvirtaus synnyttää melua. Lisäksi esitellään yleiset virtausta hallitsevat yhtälöt sekä työssä käytetyt turbulenssimallit ja seinämäkäsittelytavat, jotta lukija ymmärtää virtaussimuloinnin perusteita.

Tasonovea ei käsitelty laboratoriossa kokonaisena, vaan mittauksia varten rakennettiin useita pienempiä labyrinttikokoonpanoja eri osista ovea. Terssikaistamittaukset suoritettiin KONE Oyj:n ovilaboratoriossa Hyvinkäällä. Mittaustuloksista laskettiin vuotomäärä ja äänitehotaso kokonaiselle ovelle.

Tarkasteltava tasonovi synnyttää kohinaluontoista melua, joka sisältää kapeakaistaisia komponentteja. Kapeakaistaista melua pidetään erittäin häiritsevinä ihmisen kuuloaistimuksessa. Muuttamalla labyrinttitiivisteen rakennetta saatiin merkittävin kapeakaistainen piikki eliminoitua ja koko oven äänitehotaso laski 5 dB. Virtaussimulointi osoittautui hyödylliseksi työkaluksi vuotovirtauksen arvioimiseksi.

PREFACE

This thesis was written at Tampere University of Technology as a commission from KONE Corporation. Experimental work was engineered and implemented during 2016. The flow simulation and the actual writing process was made during 2017.

I would like to thank Prof Reijo Karvinen for supervising the work and evoking my interest in thermodynamics. Special thanks also to Professor Pentti Saarenrinne for providing guidance in the latter part of the process. Great thanks also to advisors from KONE, Jukka Turpeinen and Harri Anttila, as well as to the entire door laboratory in Hyvinkää.

In addition to studying, I used to spent a lot of time in TTMK, the motoring club of TUT. Its colourful membership will never fade into oblivion. Without you, the years might have seemed long.

During my studies, there was a particularly memorable and unexpected moment I want to share. I was building a motorcycle in my parents' garage when someone knocked on the door. There were two missionaries who asked me if I was familiar with the second law of thermodynamics. When they realized it was my expertise they soon gave up converting me.

Finally, I would like to express my gratitude to my family and close friends for supporting me during this process.

Raisio, 20.6.2018

Otto-Ville Meskanen

CONTENTS

LIST OF FIGURES

LIST OF TABLES

LIST OF ABBREVIATIONS AND SYMBOLS

CFD	Computational Fluid Dynamics
Direction 1	Flow direction from lobby to shaft
Direction 2	Flow direction from shaft to lobby
DNS	Direct Numerical Simulation
FFT	Fast Fourier transform
HVAC	Heating, ventilation, and air conditioning
LES	Large Eddy Simulation
MDF	Medium-density fibreboard
NPL	Neutral pressure level
RANS	Reynolds Averaged Navier-Stokes
RMS	Root mean square
SPL	Sound pressure level
SST	Menter's Shear Stress Transport turbulence model
SWL	Sound power level

Symbol	Meaning
A	Sound absorption area
A_o	Orifice cross-sectional area
A_0	Variable in realisable k-ε model
A_S	Variable in realisable k-ε model
a, b, c	Constants due to geometric overlapping in equation 7.1
a_1	Variable in SST k-ω model
b_T	Temperature lapse rate
C	Constant in logarithmic law of the wall
C_p	Dimensionless wind pressure coefficient
C_μ	Variable in k-ε-based turbulence models
$C_{1\varepsilon}$, $C_{2\varepsilon}$	Constants in standard k-ε model
C_2	Constant in realisable k-ε model
$CD_{k\omega}$	Variable in SST k-ω model
c	Speed of sound
c_p	Specific heat capacity at constant pressure
c_v	Specific heat capacity at constant volume
D	Depth of rectangular cavity
E	Empirical constant (= 9.793) in standard wall functions

F_x	Force in x-direction
$F_{x,surf}$	Surface force in x-direction
$F_{x,grav}$	Gravitational force in x-direction
F_1, F_2	Variables in SST k-ω model
f	Frequency
f_n	Natural frequency
G_k	Generation of turbulence kinetic energy
g	Gravitational acceleration
H	Height above reference plane
HH	Clear height of entrance
K	Environmental correction factor
k	Turbulence kinetic energy
k_P	Turbulence kinetic energy at the wall-adjacent cell centroid
k_v	Shear layer velocity ratio ($= U_c/U$)
L	Characteristic length
LL	Clear opening width of entrance
L_p	Sound pressure level
$L_{p,tot}$	Overall sound pressure level
$\overline{L_{pA}}$	A-weighted surface sound pressure level
L_W	Sound power level
$L_{W,tot}$	Overall sound power level
L_{Aeq}	A-weighted, equivalent continuous sound pressure level
L_{eff}	Effective neck length of the orifice
L_o	Neck length of orifice
l_1, l_2, l_3	Dimensions of the reference surface in noise measurement
l_ε	Length scale of turbulence dissipation rate
M	The Mach number
m	Dimensionless mode number
N	Number of microphone positions
P_T	Stack effect parameter
P_U	Reference wind parameter
p	Pressure
p_w	Wind pressure
p_0	Maximum amplitude of sound pressure
Q_{tot}	Total volume flow rate of combined openings
q	Volume flow rate
R	Gas constant for air
Re	Reynolds number
Re_y	Wall-distance-based Reynolds number

r	Radius of hemispherical surface
S	Area of sound measurement surface *or* strain rate magnitude
$\widetilde{S}, S_{ij}$	Variables in realisable k-ε model
St	Strouhal number
S_V	Total area of the surface of test room
s	Shelter factor for the particular wind direction
T	Absolute temperature *or* length of time period
t	Time
U	Average flow velocity
U_c	Shear layer velocity
U_H	Local wind speed
U_P	Mean velocity at the wall-adjacent cell centroid
U^*	Dimensionless velocity in standard wall functions
u, v, w	Velocity components in the x, y, z-direction
u', v', w'	Velocity fluctuations
u_τ	Friction velocity
u^+	Dimensionless velocity
$\mathbf{V}$	Velocity vector
V_c	Cavity volume
W	Sound power *or* width of the opening
x, y, z	Coordinate axes
y	Distance to the wall
y_P	Distance from the centroid of the wall-adjacent cell to the wall
y^+	Dimensionless wall distance
y^*	Dimensionless distance to the wall in standard wall functions
$\tilde{y}^*$	Limiter function
y^*_{limit}	Limiting factor in scalable wall functions
z	Vertical distance from ground level

Greek letters

α	Mean acoustic absorption coefficient *or* coefficient in power law
α'	Coefficient in power law
α_1, α_2	Constants in SST k-ω turbulence model
β	Exponent in power law
β_1, β_2, β^*	Constants in SST k-ω turbulence model
γ	Ratio of specific heats (isentropic expansion factor)
Δp	Pressure difference
δ	Boundary layer thickness

δ_{ij}	Kronecker delta
ε	Turbulence dissipation rate
ε_P	Dissipation at the wall-adjacent cell centroid
η	Variable in realisable k-ε model
μ	Dynamic viscosity
μ_t	Turbulence eddy viscosity
ν	Kinematic viscosity ($= \mu/\rho$)
ν_t	Kinematic eddy viscosity
ξ	Empirical constant in Rossiter's model
ρ	Density
σ_k	Constant in ε-based turbulence models
σ_ε	Constant in ε-based turbulence models
σ_ω	Constant in ω-based turbulence models
σ_{k1}, σ_{k2}	Constants in SST k-ω turbulence model
$\sigma_{\omega1}$, $\sigma_{\omega2}$	Constants in SST k-ω turbulence model
σ_{ij}	Total stress tensor
τ_{ij}	Viscous stress tensor
τ_w	Wall shear stress
ϕ	Variable in turbulence models
κ	von Kármán constant ($= 0.4187$)
Ω_{ij}	Rate-of-rotation tensor
$\widetilde{\Omega}_{ij}$	Variable in realisable k-ε model
$\overline{\Omega_{ij}}$	Mean rate-of-rotation tensor
ω	Specific turbulence dissipation rate

Subscripts

A	A-weighting
F	Fast time weighting
E	External
I	Internal
i	Opening identifier or index of summation
NPL	Under neutral pressure level conditions
P	Wall-adjacent cell centroid
ref	Reference value
S	Slow time weighting
0	Ground level conditions

1. INTRODUCTION

The first chapter of the thesis deals with the background and the reasons that have led to the research problem under discussion and the methods to investigate it.

1.1 Background

The growth of the population in the world as well as the migration from countryside to urban areas have increased the size and population of cities. This has led to higher and higher buildings. For example, the total number of 200-meter-plus buildings in the world was 1,168 at the end of 2016, when the number was 265 in year 2000 [1]. Naturally, in order to provide fluent and efficient movement of people, elevator manufacturers are competing of superiority of high-rise solutions.

However, as the height of an elevator increases, some unexpected physical phenomena may arise causing displeasing issues. The stack effect is a buoyancy-driven phenomenon that commonly occurs in high-rise buildings. Typically, the potential of this phenomenon arises in regions experiencing extreme climatic conditions, since the main driver behind it is the temperature difference between the external environment and the interior of the building.

As a result of the stack effect phenomenon, the elevator landing doors are subjected to pressure difference, which forces air to flow through the labyrinth seals of the door. This has been recognized to induce irritating noise, which potential increases where the height of the building increases. In this thesis, the leakage flow through the landing door and the noise caused thereby are examined.

Leakage flows has a major effect on the ventilation of the building, since a high building contains several floors, and thereby a lot of landing doors as well. Therefore, a better knowledge of the leakage flow rate contributes HVAC engineers to design the ventilation and air condition systems more precisely to reduce the magnitude of the stack effect phenomenon.

KONE Corporation is willing to provide reliable and complete product information

for its customers. Computational fluid dynamics (CFD) gives an insight into flow patterns that are difficult, expensive or impossible to study using experimental techniques. KONE is interested in the possibility of using this tool as a part of product development in future.

1.2 Research Problems

It has been noticed that the present KES 800 landing door induces unpleasant noise when the door is both closed and subjected to a pressure difference across the door. In such a situation, air has a tendency to flow from the high-pressure side to the low-pressure side via labyrinth sealing. It is assumed that the noise is exclusively generated by turbulent fluctuations of air flowing through the labyrinth sealing.

In this thesis, the main questions are:

- How to design the labyrinth seal geometry, so that flow-induced noise will be reduced?
- What is the leakage flow rate of the door up to a pressure difference 300 Pa?
- Is it possible to simulate the leakage flow of KES 800 landing reliably by commercial CFD software, and if so, can CFD be used in the product development of landing doors in general?

Because stack effect can produce a pressure difference in whichever direction across the landing door, the aspects mentioned above are desired to consider in both flow directions.

1.3 Methods

To examine flow-induced noise of the landing door, the intention is to design and build a test platform that enables noise measurement. Because the interest is also in the leakage flow rate as a function of pressure difference across the door, both of these quantities must be measured continuously. Measuring a full-size elevator door requires a large test facility. To avoid this, the elevator door is split into subassemblies. The purpose is to test new labyrinth seal designs in order to find a noise reducing solutions. Leakage flow through the landing door is also investigated by CFD simulation. To find a turbulence model to describe the flow as well as possible,

earlier studies and literature are explored. CFD calculations will be performed by a commercial software ANSYS® Fluent®. The obtained results will be compared with the measurements and so the potential of various turbulence models to predict the leakage flow rate will be validated.

1.4 Structure of the Report

The structure of the thesis is as follows. First, in Chapter 2, the stack effect and the driving forces behind the phenomenon are explained. The structure of the landing door under consideration is also introduced in Chapter 2. Next, in Chapter 3, basic physical concepts of sound are described. In addition, some potential cases in which gas flow causes noise are presented. The theory of computational fluid dynamics is crucial in order to perform reliable simulation results. Hence, turbulence models and governing equations of fluid dynamics are introduced in Chapter 4 . The actual flow simulation process with the details is described in Chapter 5. Experimental work including noise measurement, flow rate measurement, and the construction of tested assemblies is explained in Chapter 6. Finally, in Chapter 7 the results are summarised, and further development of the landing door is discussed in Chapter 8.

1.5 KONE Corporation

KONE Corporation, established in 1910, employs over 52,000 personnel worldwide, making it one of the global leaders in the elevator and escalator industry. The corporation operates in more than 60 countries around the world, serving over 400,000 customers. Besides supplying new elevators and escalators as well as automatic building doors, KONE provides solutions for maintenance and modernization. In 2016, the company had annual net sales of EUR 8.8 billion. The headquarters, located in Helsinki, Finland, as well as the locations of eight global R&D centers and seven production sites are shown in Figure 1.1. [2]

KONE's key customer groups include builders, building owners, facility managers and developers. In addition, architects, authorities and consultants are also key parties in the decision-making process regarding elevators and escalators. KONE has segmented the market according to the purpose of the building. The main segments are residential buildings, hotels, office and retail buildings, public transportation, airports, infrastructure, and medical buildings. KONE serves also special buildings such as leisure and education centres, industrial properties and ships.

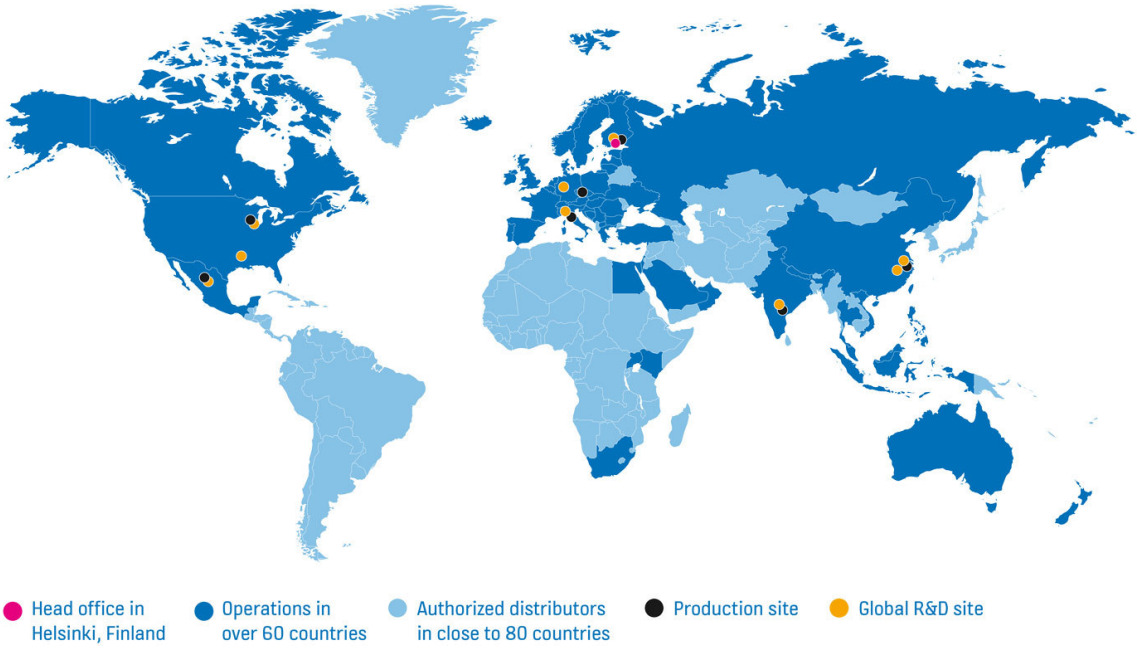

Figure 1.1 *KONE Corporation located in the world [2]. Copyright © KONE Corporation.*

1.5.1 Vision and Strategy

Around 200,000 people move into cities around the globe daily. The equipment of KONE moves over one billion users each day, with over one million elevators and escalators in service basement. The mission of KONE is to improve the flow of urban life by understanding people flow in and between buildings and by making people's journeys not only safe, but also convenient and reliable. The vision of KONE is to deliver the best People Flow® experience. Briefly, this is achieved by making sure that the people who use the products and services of the company, can move around more easily, more effectively, and have more enjoyable experiences. Figure 1.2 summarises the vision and strategy of KONE. [3]

KONE measures its progress towards its vision with strategic targets. The company aims to have the most loyal customers, to be a great place to work, to grow faster than the market, to have the best financial development in its industry and to be a leader in sustainability.

Strategic phase of KONE for 2017-2020 is called *Winning with Customers*. The main ideology is to drive differentiation further by setting the needs of users and customers at the centre of all development. The increasing urbanization provides attractive growth opportunities in the elevator and escalator industry. Connectivity and new technologies bring an opportunity to add value for customers in a way that answers better their specific needs. By closer collaboration with customers and

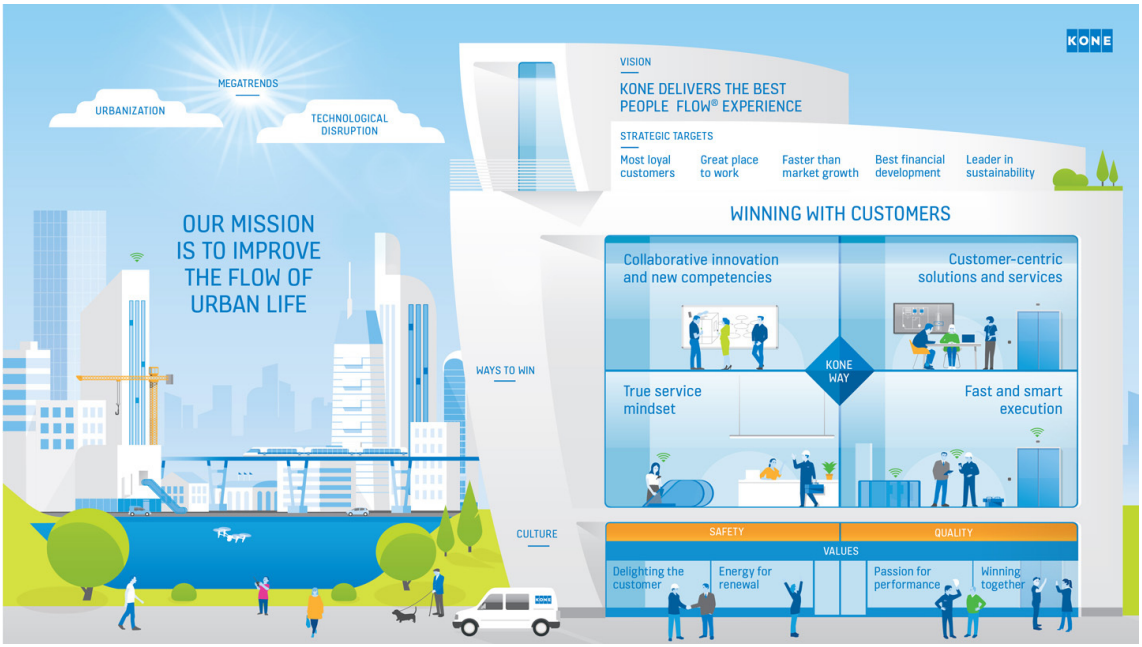

Figure 1.2 *Vision and strategy of KONE Corporation [3]. Copyright © KONE Corporation.*

partners, KONE will increase the speed of bringing new services and solutions to the market. For the new strategic phase, the company has defined [4] four *Ways to Win* that support in reaching its targets:

- Collaborative innovation and new competencies
- Customer-centric solutions and services
- Fast and smart execution and
- True service mindset.

1.5.2 KONE References

KONE has participated in numerous large-scale projects. *Doha Tower* in Qatar, *Cayan Tower* in Dubai, *The River South Tower* in Bangkok, *Makkah Clock Royal Tower* in Saudi Arabia (see Figure 1.3(a)), *The Shard* in London, *China Merchants Tower* in Shenzhen, *Marina Bay Sands* in Singapore, *One Bloor* in Toronto, Canada, and *De Rotterdam* in Netherlands are some of the most famous KONE references of the 2010 decade so far [5]. Worth mentioning is also one of the world's longest cruise ship, *Norwegian Getaway*, as well as *Jeddah Tower* (see Figure 1.3(b)), in Saudi Arabia, that will be the tallest building in the world when completed in 2020.

(a) Makkah Clock Royal Tower (601 m) in Saudi Arabia.

(b) Jeddah Tower (1008 m) in Saudi Arabia.

Figure 1.3 *Some KONE references [6]. Copyright © KONE Corporation.*

2. STACK EFFECT AND LANDING DOOR

In this chapter, stack effect and the driving forces behind it are described. The phenomenon is crucial for understanding the development of pressure difference across the elevator landing door. The structure of the door and its operation is introduced at the end of the chapter.

2.1 Stack Effect

Stack effect (also referred as to the *chimney effect*) is a phenomenon which occurs especially in tall buildings when the temperature indoors is higher than the temperature outside the building. In cold weather, a tall building can act like a chimney when cold air enters at the lower floors, rises through the building due to natural convection, and exits from the top of the building. The driving force, buoyancy, results from the difference in density between the cold air outdoors and the warm, less dense air inside the building. The stack effect creates pressure difference proportional to the height of the building as well as to the temperature difference between the warm air indoors and cold air outdoors. [7]

The stack effect can act also in reverse direction. This is a potential situation in warm and tropical climates, especially in the summertime, when the temperature outside the building is warmer than the temperature inside the building. For example, in the case of Burj Khalifa, magnitude of the stack effect is predicted assuming that the internal and external air temperature are +21 °C and +46 °C respectively. To give one an idea of the potential of the stack effect in this case, the maximal pressure difference is estimated at 320 Pa when the height of the shaft is 700 meters and other driving forces are ignored [8]. In reverse stack effect, air enters the building at the upper floors and exits at the ground level. The driving force of this reverse phenomenon is the same as in the aforementioned stack effect, but in this case the denser air is inside the building.

Density difference resulting from the temperature difference is not enough to explain the entire potential of the stack effect exclusively. Wind induces pressure differences across the envelope as well as forced heating and ventilation system of the building

while maintaining air quality requirements. The magnitude of the stack effect also depends on the locations and characteristics of the openings in the building envelope. Next, these driving mechanisms and their effect on the pressure difference are introduced more closely.

2.1.1 Pressure Difference Generated by Temperature

Hydrostatic pressure of air or stack pressure results from the weight of an air column above the point of interest. The weight of the air column is directly proportional to its density and height. Hydrostatic pressure refers especially to fluid in static equilibrium. The difference in internal and external pressures of a building caused by the temperature difference can be explained as follows. The mathematical formulation of the hydrostatic pressure gradient is

$$\frac{\partial p}{\partial z} = -\rho g \tag{2.1}$$

where p is pressure, z is the vertical distance from some reference point, which is taken to be ground level here, and g is the gravitational acceleration. The air density is denoted by ρ, which dependence on the air temperature and pressure can be expressed as

$$\rho = \frac{p}{RT} \tag{2.2}$$

where T is absolute temperature, and R is the gas constant for air. Equation 2.2 is the ideal gas law, which applies at normal temperatures and pressures when air can be treated as an ideal gas. Therefore, changes in the air temperature has an influence on hydrostatic pressure gradient over density. Hence, if the indoor temperature differs from the ambient temperature, the result will be different hydrostatic pressure gradients as illustrated in Figure 2.1. For a building without any internal partitions (singe-zone building), the pressure difference across the envelope changes linearly with elevation. If the building envelope is not perfectly sealed, the pressure difference causes leakage flow from the higher to lower pressure region through cracks and openings. The sign of the pressure difference typically changes at some height and this point is generally referred to as the *neutral pressure level* (NPL). [9]

Assuming density is constant over the height of the building, hydrostatic pressure is given by

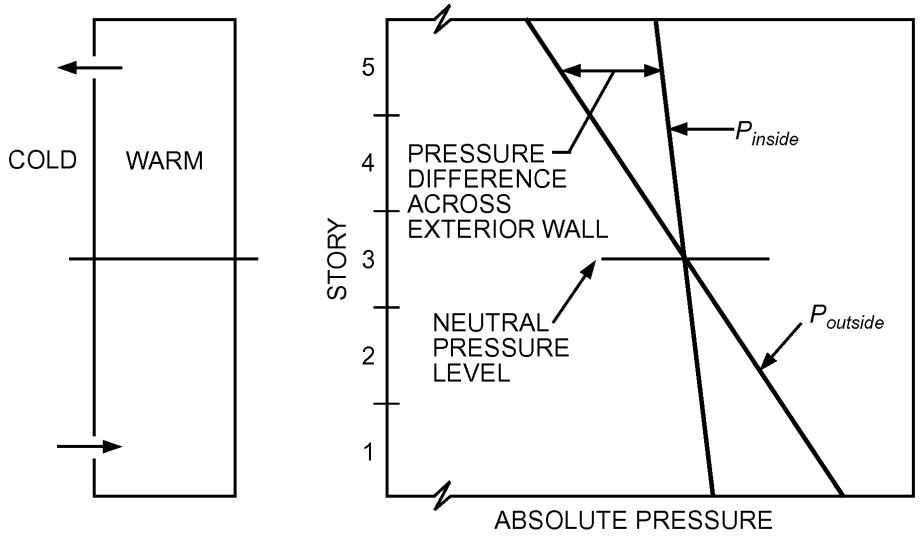

Figure 2.1 *Hydrostatic pressure gradient in the case of building with no internal partition [10].*

$$p = p_0 - \rho g z \tag{2.3}$$

where subscript '0' denotes ground level conditions. When equation 2.3 is applied to both sides of the building envelope, the pressure difference due to hydrostatic pressure is given by

$$\Delta p = (p_E - p_I) = p_{E0} - p_{I0} - \frac{gz}{R} p_{E0} \left(\frac{1}{T_{E0}} - \frac{1}{T_{I0}} \right) \tag{2.4}$$

where subscripts 'E' and 'I' denote the external and internal air respectively. If the location of the NPL is known, the stack pressure difference at height z can be expressed as

$$\Delta p = (p_E - p_I) g (z_{NPL} - z) = \rho_E \left(\frac{T_I - T_E}{T_I} \right) g (z_{NPL} - z) \tag{2.5}$$

where z_{NPL} is height of neutral pressure level without any other driving forces. Assuming no internal airflow resistance, equation 2.5 provides a maximum hydrostatic pressure difference [10]. Assuming no other driving forces and no stack effect within the flow elements themselves, the top of the building is pressurized and the base is depressurized relative to outdoors when indoor air is warmer than outdoors.

However, the simplification regarding to density in equations 2.3, 2.4 and 2.5 cannot

be accepted in the case of very tall buildings. Equation 2.3 should then be modified to involve the density gradient of the outdoor air as a function of altitude [10]. When a linear variation of temperature is assumed, $T = T_0 - bz$, equations 2.1 and 2.2 give

$$p = p_0 \left(1 - \frac{bz}{T_0}\right)^{\frac{g}{Rb_T}} \tag{2.6}$$

where b_T is temperature lapse rate [9]. Generally, appropriate value for b_T is -0.0065 K/m, which means the temperature degrease is 6.5 °C per kilometer [11, 12].

As for real buildings, the situation is more complicated due to multiple floors and partitions. If the vertical leakages between floors are totally blocked, each floor has an NPL and each floor acts independently being unaffected by any other floor, as illustrated in Figure 2.2(a). However, vertical air passages such as stairwells, elevator shafts and service shafts allow vertical movement of air inside the building. Figure 2.2(b) represents such a building, which has uniform openings across the building envelope, through each floors, and into the vertical shaft. The slope of the interior hydrostatic pressure is equal in all these cases (see Figures 2.1, 2.2(a) and 2.2(b)). The discontinuities represent the pressure differences across the floors. Part of the pressure difference is lost whenever there is a flow resistance between the shaft and outdoors. Thus, the pressure difference across the building envelope (as well as landing door) at any level is maximized when there is no internal partition and flow resistance on the floor. [10]

2.1.2 Pressure Difference Generated by Wind

The pressure difference across the building envelope is also dependent on the wind. Where hydrostatic pressure varies with height, the wind generates a distribution of static pressures on the exterior surface, which is rather a function of the wind direction and surface orientation than height. In ventilation literature, pressure due to air motion is often called a wind pressure at a point and it is given by

$$p_w = C_p \frac{\rho U^2}{2} \tag{2.7}$$

where is outside air density and U is average wind speed. Actually, wind pressure indicates the rise in pressure from the hydrostatic pressure. C_p is dimensionless wind pressure coefficient at a point on the building surface. Thus, the pressure difference across the i^{th} opening at height z_i is given by

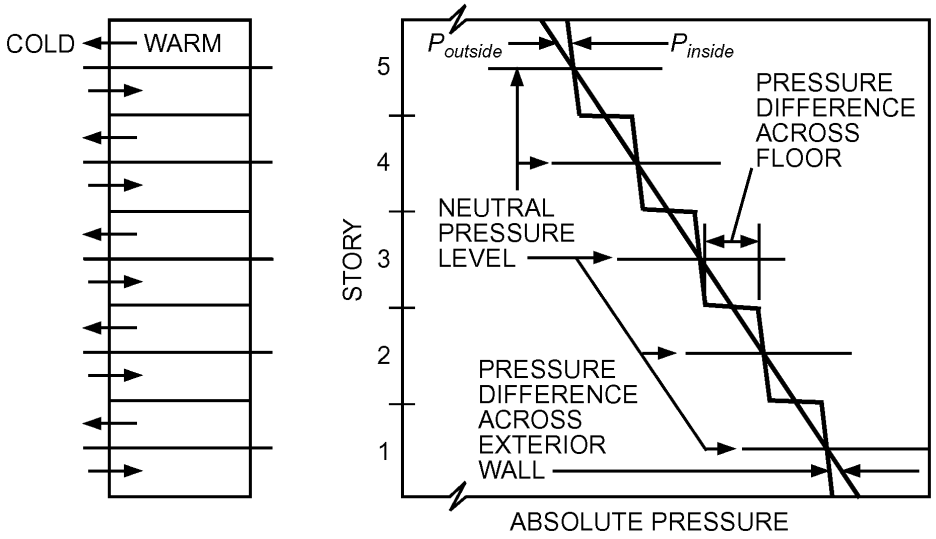

(a) Building with airtight separation of each story

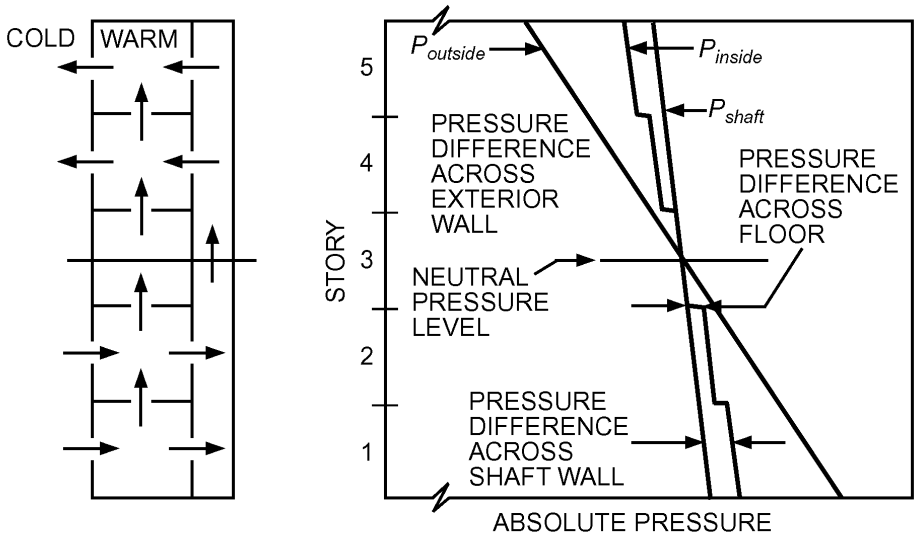

(b) Real building with open shaft

Figure 2.2 *Effect of compartmentation in buildings on pressure differences across exterior wall and shaft wall [10].*

$$\Delta p_i = p_{E0} - p_{I0} - \frac{gz_i}{R}\rho_{E0}\left(\frac{1}{T_{E0}} - \frac{1}{T_{I0}}\right) + p_{wi} \tag{2.8}$$

C_p of zero corresponds to free stream pressure, while C_p of one refers to a stagnation point. Generally, the value of C_p is positive on the windward side and negative on the other sides of the building. However, the wind pressure effect generally increases with altitude due to the atmospheric boundary layer [13]. The values of C_p for different cases can be found in the literature. Figure 2.3 illustrates the effect of a constant wind profile on a building with symmetric openings around the mid-height

and with negligible internal resistance to airflow. [10]

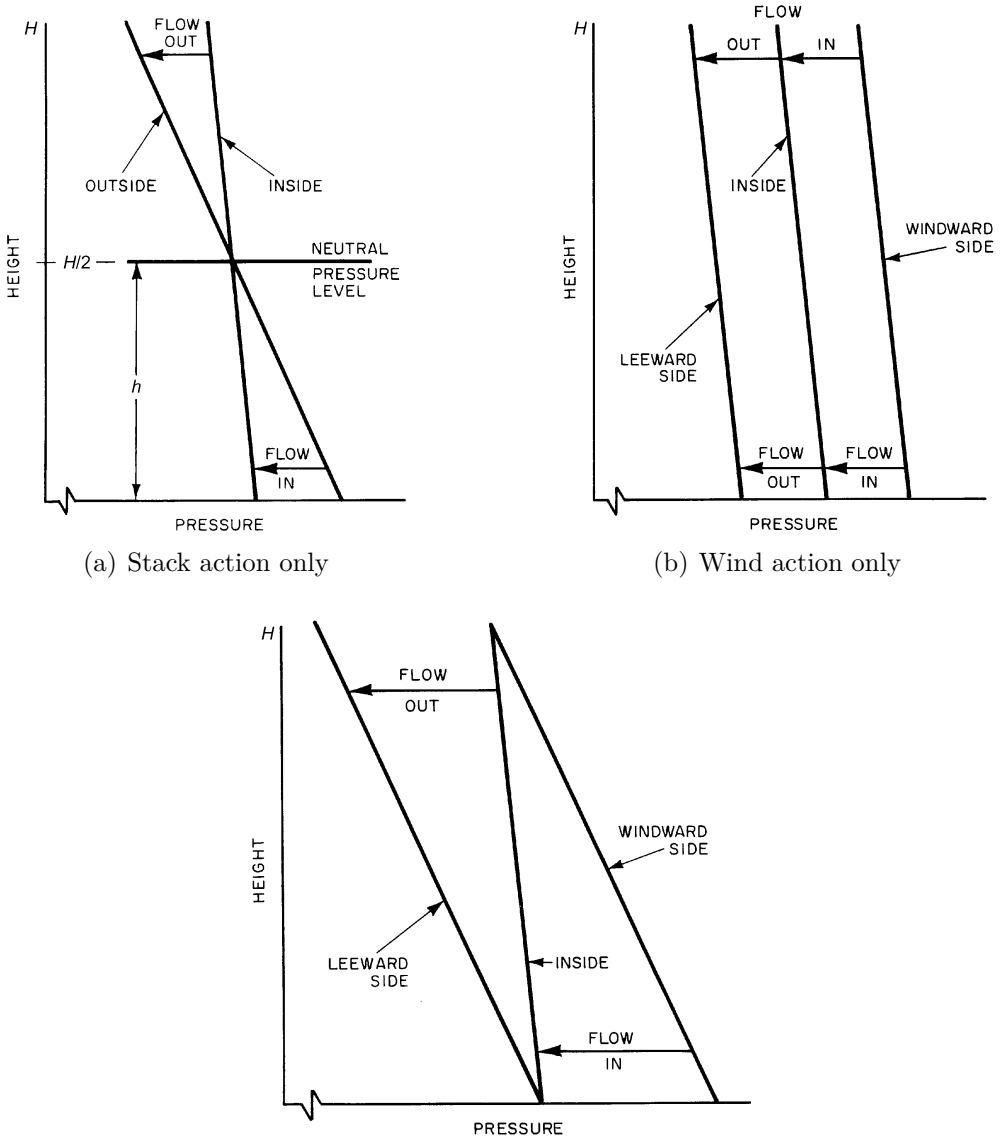

(a) Stack action only

(b) Wind action only

(c) Combined stack and wind action

Figure 2.3 *Effect of wind on stack effect [10].*

2.1.3 Neutral Pressure Level

Neutral pressure level (NPL) is a plane at the height where there is no pressure difference between the ambient and the interior of the building. For a tall building the NPL is usually located between 0.3 and 0.7 of the building height [14]. The exact location of the NPL is difficult to predict because it is a combination of many factors such as compartmentation, location of elevator shafts and stairwells, leakage of building envelope, mechanical ventilation and effect of the wind. For instance, a

relatively large opening in the building envelope moves the NPL toward the opening. It is also possible that a building does not have the NPL at all. [10]

2.1.4 Combining Driving Forces

When the indoor temperature is assumed to be uniform the pressure differences driven by stack effect, wind and mechanical ventilation system are able to predict in combination to each envelope of the building, such that

$$\Delta p = s^2 C_p P_U + H P_T + \Delta p_I \tag{2.9}$$

where s is shelter factor for the particular wind direction and the reference wind parameter P_U is

$$P_U = \rho_o \frac{U_H^2}{2} \tag{2.10}$$

and the stack effect parameter P_T is

$$P_T = g\rho_o \left[\left(T_i - T_o \right) / T_i \right] \tag{2.11}$$

The direction of Δp in equation 2.9 is so that positive differential pressure causes inflow. The local wind speed U_H takes into account the wind speed change in height, i.e. the effect of the atmospheric boundary layer. The term Δp_I is the pressure acting to balance inflows and outflows including flows generated by mechanical ventilation system. The combined cumulative effect of the main driving forces of the stack effect is shown in Figure 2.4

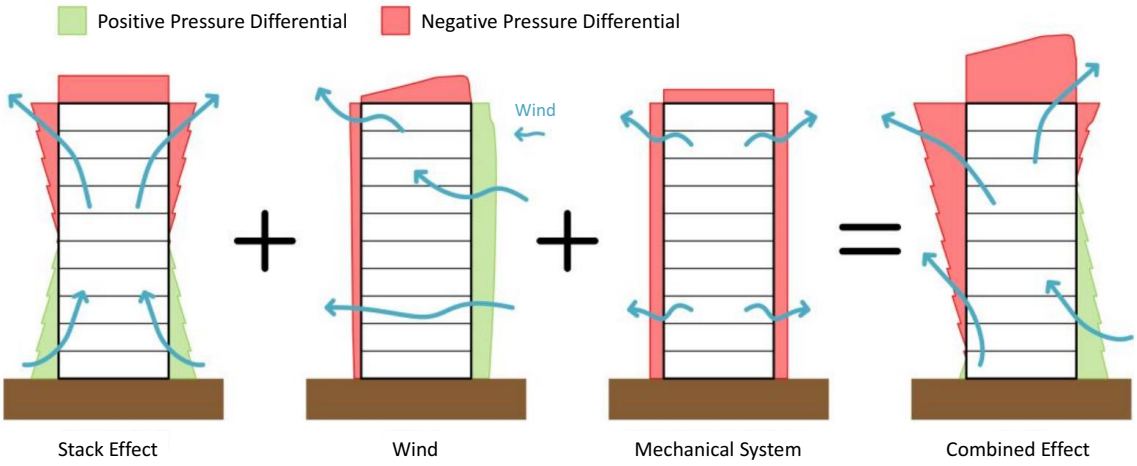

Figure 2.4 *Combining driving forces of stack effect.*

2.2 KES 800 Landing Door

Elevator doors can be classified to the car door and the landing door according to their functionality. The landing door is the door that can be seen from the lobby while waiting the arrival of the elevator car. Thus, the landing door exist on each floor, from which the elevator can be used. Figure 2.5 shows the location of the landing door in the elevator shaft. The primal task of a landing door is to provide safety and reliable operation of the elevator preventing anything from falling down to the elevator shaft. Other safety aspects, such as fire safety, are discussed further in Section 2.2.2. Unlike a landing door, a car door is equipped with a motor and an operator. When the elevator car reaches the landing, the coupler of the operator attaches to the landing door and forces both doors to open simultaneously. [15]

In this thesis, the object of study is KES 800 landing door intended for personal transport. There are several different configurations of this door type on the market. However, the interest of this work lies in two-panel center-opening door, which consist of two laterally opening door panels that meet in the middle of the entrance, as illustrated in Figure 2.6.

KONE elevator landing entrance consists of four basic elements: frame, door panels, railing mechanism and door sill. The door is attached to the elevator shaft wall with the frame. At the top, the door panels are hanging from the railing via roller guides, which is the only vertical support for the door panels. The bottom edge of the door panels is supported by the sill and sliding guide shoes, which allows the lateral movement of the door panels. There is no contact with the bottom of the sill profile and the guide shoes. The door has a fire labyrinth around the door panels to prevent the leakage of smoke and fire gases from flowing through the door. [15]

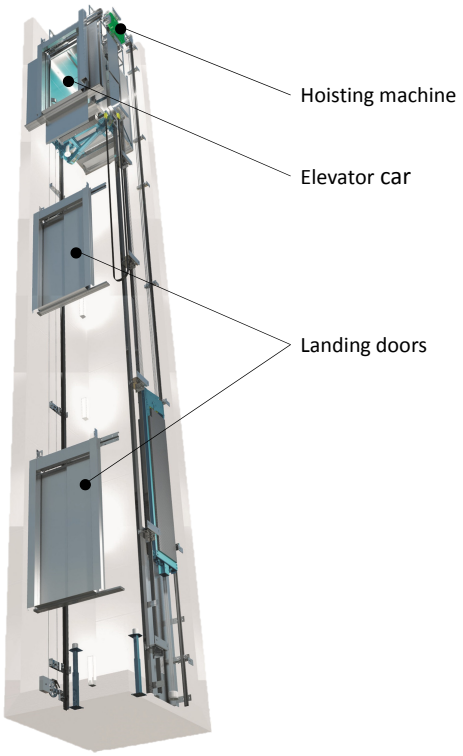

Figure 2.5 *Landing door location in elevator shaft. Copyright © KONE Corporation.*

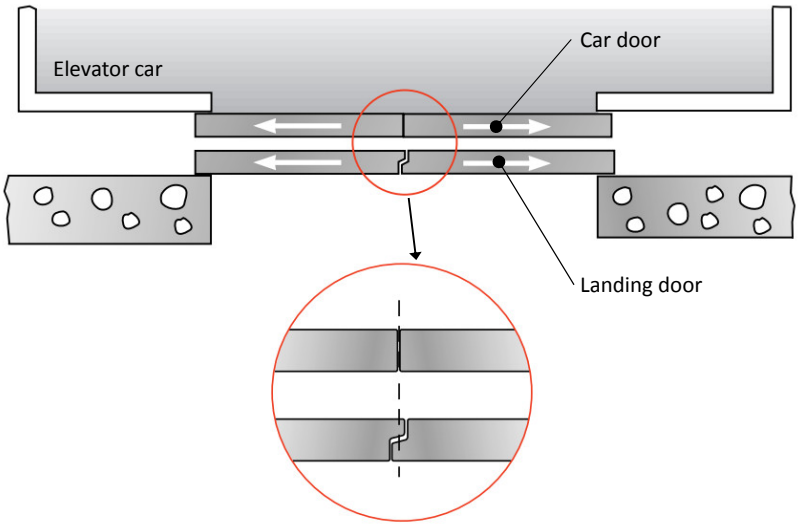

Figure 2.6 *Two-panel center-opening KES 800 landing door, adapted from [16].*

Normally, KONE landing doors are manufactured from steel, stainless steel or a combination of glass and one of the previous. In addition, various materials are used to produce smaller parts. The door panels and the components of the frame are usually made of sheet metal, which is bent and then assembled with glue and welding. Figure 2.7 represents the main elements of the door, whereas the fire labyrinth details are presented in the next section. [17]

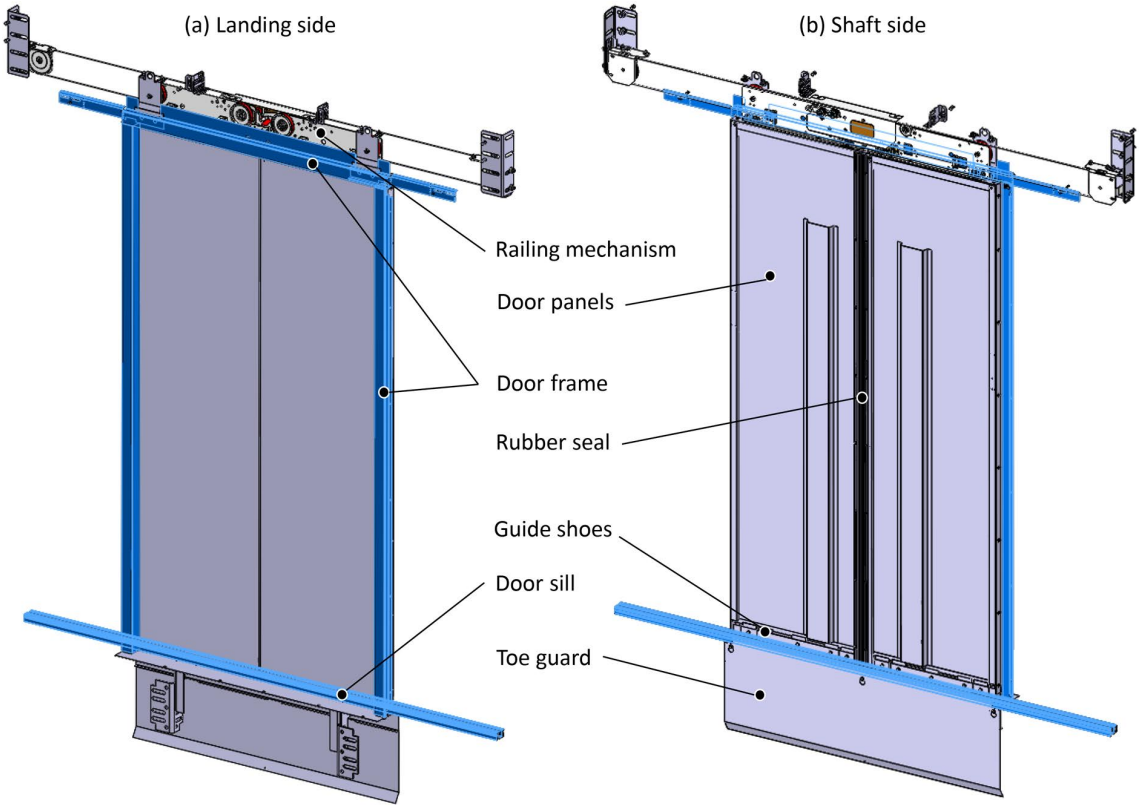

Figure 2.7 *Landing door elements as seen from (a) landing side, and (b) shaft side. Blue coloured parts (i.e. frame and door sill) form the fixed part of the labyrinth sealing.*

KES 800 landing door is available in several different sizes. The clear opening width of the door varies between 2000 and 3000 mm (step 100 mm) and the height between 700 and 3000 mm (see Figure 2.8).

2.2.1 Fire Labyrinths

Between the door panels and the frame there is a labyrinth sealing around the door. The door frame and the sill form the fixed part of the fire labyrinth. The outer edges of the door panels have a sheet metal which, when closed, forms a simple labyrinth geometry together with the fixed parts. The geometry of the lintel and upright labyrinth is very similar, as illustrated in Figure 2.9. Nonetheless, one can notice

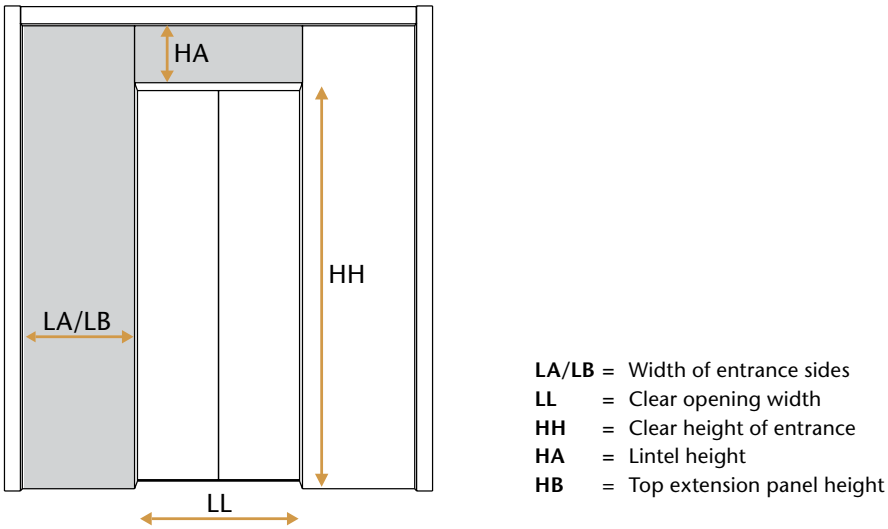

Figure 2.8 *Dimensions associated with size of landing door.*

a small difference in the covering that is assembled onto the actual frame pillar for cosmetic reasons [18]. In the immediate vicinity of the lintel labyrinth there are railing components, which may have a minor influence on the airflow as well. In the middle of the entrance, where the door panels coincide with each other, there is a rubber seal to block leakage flow entirely.

The sill labyrinth consists of a sill profile, guide shoes and a sheet metal thickness of 3 mm fitted in the sill groove. There are four sliding shoes supporting the bottom of the landing door, two on both door panels. Under every guide shoe, there is a straight slot at the bottom of the sill groove for dust removal. Naturally, these slots also form a path for air flow. The details of the sill labyrinth geometry can be seen in Figure 2.10.

The fire labyrinth has approximately 5 mm clearance wherever contact can occur. This ensures quiet and reliable operation of the door. However, the clearance depends somewhat on installation and wear that appears mainly in rollers. Due to wearing, the door descends and glides deeper in the sill groove [18].

2.2.2 Fire Safety Aspects

Landing doors are safety components that must meet not only mechanical safety standards but also fire safety standards prior to market access. Fire-induced smoke is the most hazardous component in a fire. In high-rise buildings, smoke may migrate a very long distance along the elevator shafts due to stack effect [12]. A landing door is an essential component in terms of passive fire protection. Its function is

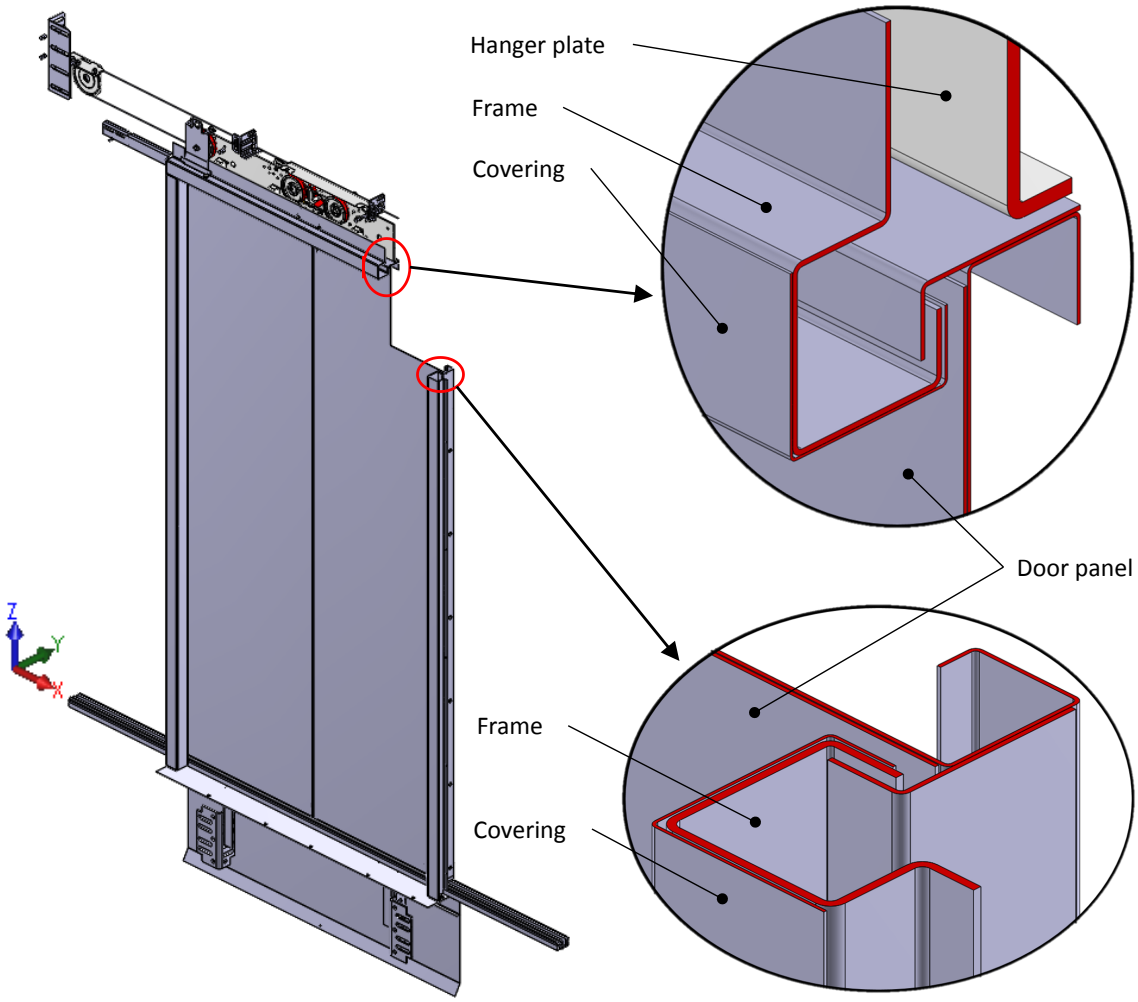

Figure 2.9 *Details of upright and lintel fire labyrinths. Positive Y-axis points towards the elevator shaft.*

to prevent the smoke and fire from spreading within the building and its proper operation can save lives and entire buildings from destruction. The fire resistance of a landing door is a major safety issue, which is based on the experiment where a heat source is placed on the landing side and heat is transferring into the elevator shaft through the landing door during the test. Fire resistance tests are described in details in various standards used in different countries. In addition, test procedures commonly include integrity testing, which means the allowed leakage of smoke, CO_2 and other hot gases through the door is limited. Fire ratings for landing doors are principally same as used in building safety and fire resistance elements. Some widely-used standards are [19]:

- EN 81-58; Used in most European countries
- UL 10B; Used in North America

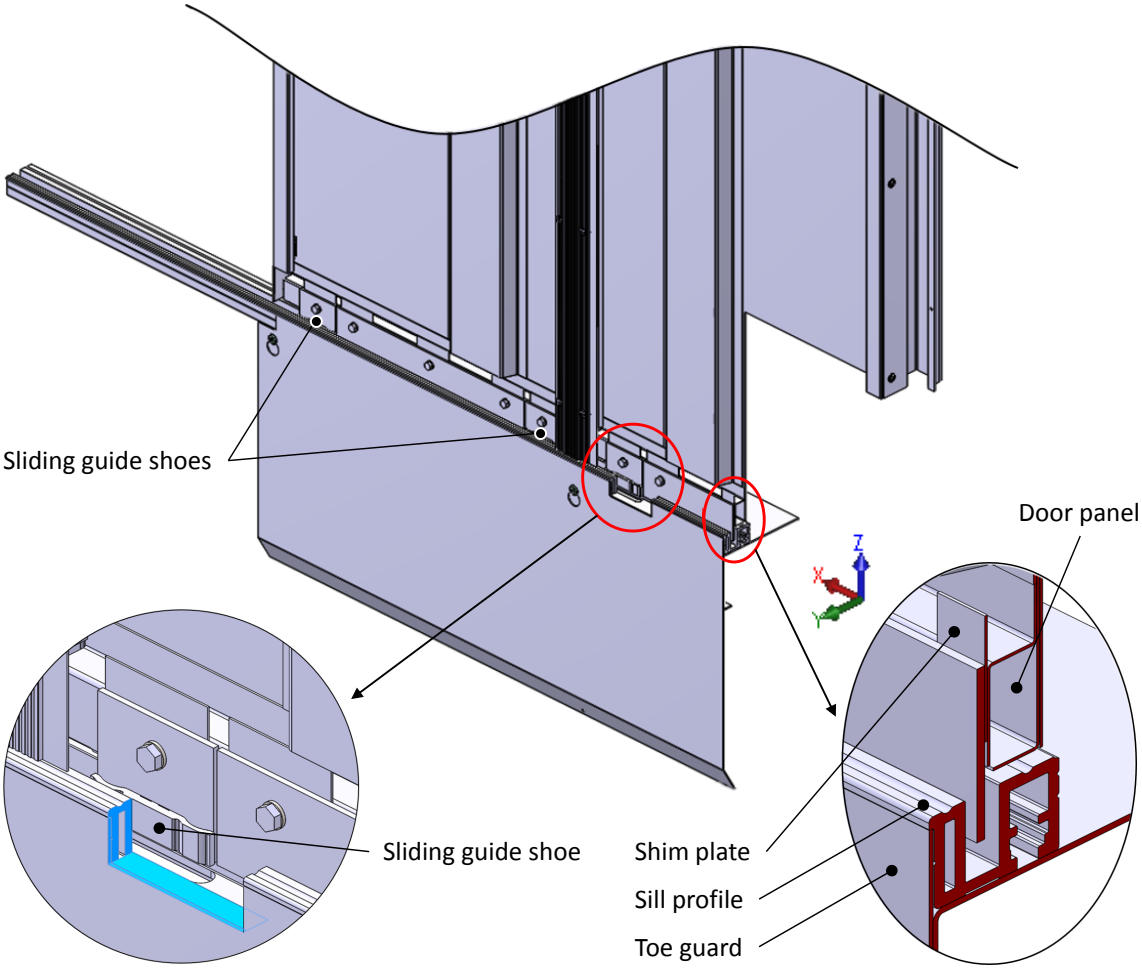

Figure 2.10 *Details of sill labyrinth and guide shoe locations as seen from shaft side.*

- BS 476-22; Used in Great Britain and its former colonies
- IMO MSC 61-3; Used for marine elevators

The purpose of fire labyrinth is to reduce leakage through the landing door. Therefore, its role is particularly important for in case of a fire. The use of combustible materials on the landing door is not desirable since it may weaken the fire resistance rate of the door [18]. These issues should be taken into consideration when designing the door.

3. THEORY OF SOUND AND NOISE MEASUREMENT

Some basic physical concepts of sound and noise measurement are considered in this chapter. In addition, some well-known sources of aerodynamic sound are presented.

3.1 What is sound?

From a physical point of view, sound is a vibration that travels in a medium as a sound wave. The medium can be in any state of matter, but this thesis deals with sound propagation in gas, and specifically in air. In the air the sound proceeds as a longitudinal wave motion and when it meets the ear, a hearing perception is generated.

The speed of sound c is given by

$$c = \sqrt{\gamma RT} \tag{3.1}$$

where γ $(= c_p/c_v)$ is the ratio of specific heats.

3.2 Different Types of Sound

The sound phenomenon can be classified in several ways. First, the sound phenomenon may be continuous, variable, intermittent or impulsive depending on how it changes over time. Continuous sound is stable and unchanged over a given period of time. Intermittent noise includes a mixture of relatively noisy and quiet periods with deviation of at least 5 dB in noise levels, whereas impulse noise consists of time periods less than one second, with sound pressure level exceeding the background sound pressure level by more than 20 dB. [20]

In noise measurements, sound is usually described by sound spectrum or the time variation of SPL. Spectrum illustrates how the sound energy is divided into different

frequencies. Normally, x-axis shows the frequency and the y-axis presents sound energy. The frequency spectrum of a sound phenomenon can be a continuous or so-called line spectrum. A pure tone consists of a single frequency and it has a sinusoidal waveform that can be represented by equation

$$p(t) = p_0 \sin(2\pi f)\ t \tag{3.2}$$

where $p(t)$ is instantaneous sound pressure, p_0 is the maximum amplitude of the sound pressure, and f is the frequency [21].

The sound energy of a pure tone is concentrated on a single frequency and thus the spectrum is a line spectrum as illustrated in Figure 3.1. The spectra of all periodic sound vibrations are line spectra, consisting of the fundamental frequency and harmonic components (i.e. overtones), of which frequencies are integer multiples of the fundamental. Pure tones exist rarely alone, but are usually associated with broadband noise. [20]

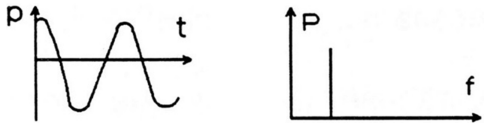

(a) Pure tone

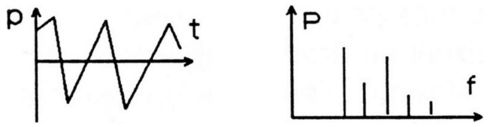

(b) Inharmonically related line spectrum

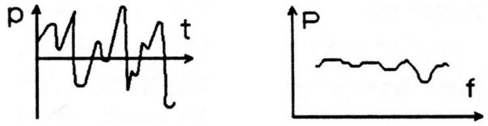

(c) Continuous spectrum

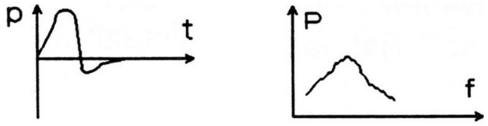

(d) Impulse sound

Figure 3.1 *Waveforms $p(t)$ and sound power spectra $P(f)$ of different types of noise [20].*

The frequency spectrum of an aperiodic sound is continuous. This kind of sound is a combination of an infinite (large) number of tones. An aperiodic sound can be divided into a transient sound, that occurs just once and briefly, and a noise sound, where the pressure at each moment is random. Energy and sound pressure are then expressed for a given frequency band. For example, a vortex in a flow generates such a noise sound. The maximum height and the corresponding position depends on the nature of the sound.

3.3 Concepts Related to Noise measurement

Here, physical quantities relevant for noise measurement are presented.

3.3.1 Sound Pressure Level

In the field of acoustics, the most essential physical measure is sound pressure. In general, pressure is the force applied perpendicular to the surface of an object per unit area. Hence, the unit of pressure is the Pascal (Pa = N/m^2). On the other hand, sound pressure is the local pressure deviation from the ambient atmospheric pressure in a medium, which is considered to be air in this work. Typically, sound pressure values are significantly smaller than the static pressure. Human hearing can deal with sounds that are within the range of 20 µPa to 50 Pa, while static air pressure in the atmosphere is around 100 kPa. Sound pressure is an important quantity because it correlates well with the perception of loudness, and furthermore, it can be measured easily.

Due to the fact that sound pressure varies over a large range in Pascal units, it is more convenient to use a logarithmic unit, the decibel. In acoustics, the concept of the decibel is used in a special way. If a fixed sound pressure reference is used, decibels are then absolute level units. Sound pressure level (SPL) is defined by

$$L_p = 10 \log_{10} \left[\frac{p(t)}{p_{ref}} \right]^2 = 20 \log_{10} \frac{p(t)}{p_{ref}} \tag{3.3}$$

where $p(t)$ is instantaneous sound pressure and p_{ref} is the reference sound pressure, standardized at 20×10^{-6} Pa. The reference pressure is selected so that it approximately corresponds to the threshold of hearing at a frequency of 1 kHz. On the decibel scale, human hearing can deal with sounds in the range of 0 to 130 dB. Table 3.1 shows some examples of different sound pressure levels. [22]

It is often necessary to determine the overall level $L_{p,tot}$ from the measured series of contiguous bands. However, logarithmic sound pressure levels are generally expressed in decibels and so cannot be manipulated until converted back to a linear scale. When the sound waves do not have the same phase, as is usually the case for noise measurement, the summation formula is

$$L_{p,tot} = 10 \log_{10} \sum_{i=1}^{n} 10^{L_{pi}/10} \tag{3.4}$$

where L_{pi} is the i^{th} addend sound pressure level [20]. Hence, the doubling of the sound pressure will cause a 3 dB rise in the decibel scale.

Table 3.1 *Example of sound pressure levels [23].*

Sound Source	Sound Pressure (Pa)	Sound Pressure Level (dB, A-Weighted)
Saturn rocket	100,000	194
Ram jet	2,000	160
Propeller aircraft	200	140
Riveter	20	120
Heavy truck	2	100
Noisy office or heavy traffic	0.2	80
Conversational speech	0.02	60
Quiet residence	0.002	40
Leaves rustling	0.0002	20
Hearing threshold, excellent ears at frequency maximum response	0.00002	0

The basic rule is that 1 dB differences are noticeable by ear in an immediate comparison [20]. However, this depends slightly on the SPL and frequency of the sound. Time-separated sounds require a difference of about 5 dB in order to be clearly distinguishable.

3.3.2 Sound Power Level

Sound power or acoustic power is a property that indicates the radiating energy by the sound source. For convenience, a decibel scale is also used with sound power. Thus, sound power level (SWL) is defined as

$$L_W = 10 \log_{10} \left[\frac{W}{W_{ref}} \right] \tag{3.5}$$

where W is sound power and W_{ref} is the reference sound power, which value generally is 10^{-12} W [21]. Table 3.3 shows some examples of different sound power levels. The summation of SWLs can be performed identically as in the case of sound pressure levels

$$L_{W,tot} = 10 \log_{10} \sum_{i=1}^{n} 10^{L_{Wi}/10} \tag{3.6}$$

where $L_{W,tot}$ is the overall sound power level and L_{Wi} is the i^{th} addend sound power level. Table 3.2 illustrates the influence of chance in SWL on absolute sound power and subjective effect. A rule of a thumb here is that a 3 dB reduction halves the noise in watts.

Table 3.2 *Subjective effect of change in sound power level [24].*

Sound Level Change	Acoustic Energy Loss	Subjective Effect
0 dB	0 %	Reference
-1 dB	21 %	Barely Perceptible
-3 dB	50 %	Noticeable to most
-5 dB	68 %	Clearly Perceptible
-10 dB	90 %	Half as Loud
-20 dB	99 %	1/4 as Loud
- 30 dB	99.9 %	1/8 as Loud
- 40 dB	99.99 %	1/16 as Loud

3.3.3 Frequency Weighting

A sound level meter is designed to give SPL readings. However, the human hearing response is not constant over the audio band. This means that the human ear perceives the change in the loudness of the sound as the frequency changes, even if the SPL reading remains the same. The lack of hearing sensitivity is the most pronounced at low frequencies. Moreover, it is proportional to the intensity of the sound, that is to say, that the shape of so-called equal-loudness curve changes with

Table 3.3 *Example of sound power levels [25].*

Sound Source	Sound Power (W)	Sound Power Level (dB)
Heavy thunder Small aircraft engine	1	120
Accelerating motorcycle Chain saw	0.1	110
High pressure gas leak	0.01	100
Small air compressor Lawn mover	0.001	90
Alarm clock Dishwasher	0.0001	80
Noisy office Vacuum cleaner Toilet flushing	0.00001	70
Hair dryer Busy restaurant or canteen Noisy home	10^{-6}	60
Quiet office Average home	10^{-7}	50
Private office Quiet home	10^{-8}	40
Quiet conversation	10^{-9}	30
Whisper	10^{-10}	20

SPL. Thus, different frequency weightings have been standardized to compensate the issue. Figure 3.2 shows A-, B- and C-weightings that are tailored to correspond with the frequency characteristics of hearing at SPLs of 40, 70 and 100 dB respectively.

The A-weighting has proven to be the best in terms of adverse health effects and is currently being used almost exclusively [20]. In addition, Z-weighting (zero frequency weighting) implies no frequency weighting. The symbol of A-weighted sound pressure level is L_{pA}, but often the weighting is shown only in a unit such as dB(A) or dBA.

3.3.4 Equivalent Continuous Sound Pressure Level

The target of noise measurement is most often to determine the A-weighted equivalent noise level L_{Aeq} that corresponds to a constant sound level that produces the same sound energy during the measurement time as the measured noise [20]. It is given by

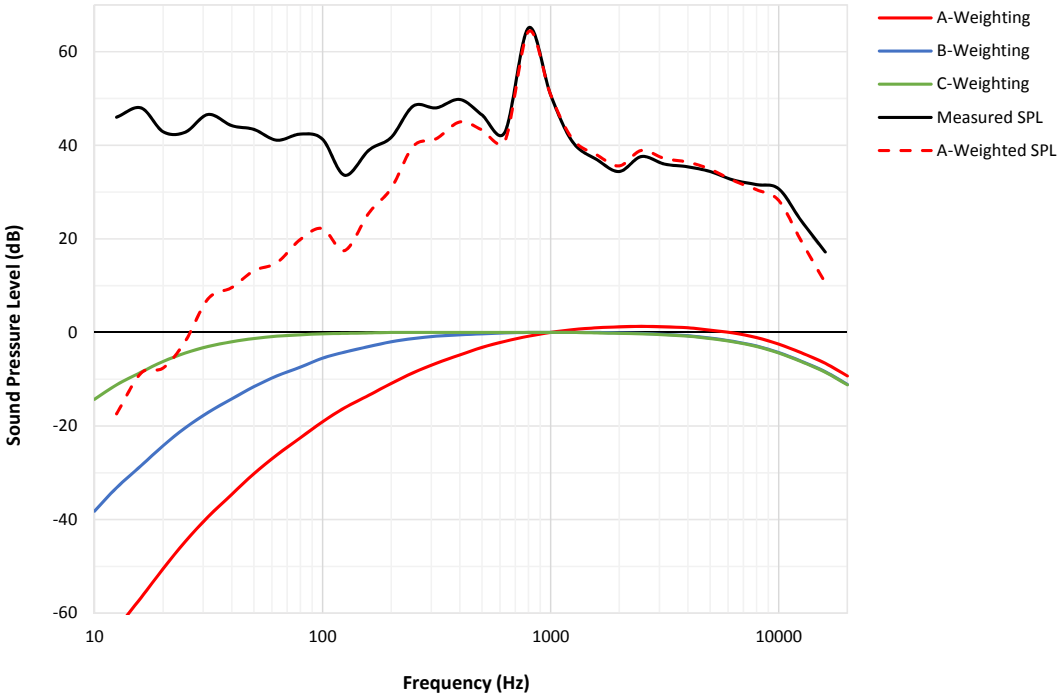

Figure 3.2 *Frequency weightings, based on [26].*

$$L_{Aeq,T} = 10 \log_{10} \left[\frac{1}{T} \int_0^T \left(\frac{p(t)}{p_{ref}} \right)^2 dt \right] \tag{3.7}$$

where t is time and T is length of the time period. The time T must be specified when equivalent level is used, $L_{Aeq,8h}$ for example.

3.3.5 Time Weighting

Practically speaking, sounds vary widely with time. Generally, this kind of phenomenon is described by a graph with time on the x-axis and acoustic quantity on the y-axis. Different time frames are used to describe fluctuations of sound. Time frame is the time interval, of which the value of the RMS sound pressure and the corresponding SPL are formed. Sound level meters use standardized time frames or time weightings. F (Fast) time weighting corresponds to a 125 ms time constant, whereas S (Slow) corresponds to a 1 second time constant. For example, when F time weighting is used the sound level meter displays an average of 250 ms, which is twice the time constant [20]. The shorter the time constant, the higher the resolution of the meter to detect different variations in the SPL, and, for example, the higher the reading of the impulse noise. The SPL of steady noise can be simply depicted by the instantaneous value displayed by the noise meter and the measured

value is named L_{AF} or L_{AS} where 'A' refers to the A-weighting. When measuring fluctuating noise, a longer equivalent level is used.

3.3.6 Octave Band Analysis

The frequency analysis can be narrowband or broadband depending on the width of the frequency band used for the analysis. A method where the relative bandwidth of the filter is constant is generally used in noise measurements. Octave band filter is commonly used to estimate the disturbance of noise. However, third octave filter corresponds better to the features of hearing than octave filter. On the other hand, a more precise analysis may be necessary if the purpose of the measurement is to examine the source of noise. [20] Table 3.4 shows the standardized third octave bands. It should be noted that the narrower bands are used, the higher the spectrum will be located on the dB-scale. The octave spectrum is about 5 dB higher on average than the third octave spectrum.

Table 3.4 *One-third octave bands with upper and lower band limits [21].*

Band	Lower Band Limit (Hz)	Center Frequency (Hz)	Upper Band Limit (Hz)	Band	Lower Band Limit (Hz)	Center Frequency (Hz)	Upper Band Limit (Hz)
12	14.1	16	17.8	28	562	630	708
13	17.8	20	22.4	29	708	800	891
14	22.4	25	28.2	30	891	1,000	1,122
15	28.2	31.5	35.5	31	1,122	1,250	1,413
16	35.5	40	44.7	32	1,413	1,600	1,778
17	44.7	50	56.2	33	1,778	2,000	2,239
18	56.2	63	70.8	34	2,239	2,500	2,818
19	70.8	80	89.1	35	2,818	3,150	3,548
20	89.1	100	112	36	3,548	4,000	4,467
21	112	125	141	37	4,467	5,000	5,623
22	141	160	178	38	5,623	6,300	7,079
23	178	200	224	39	7,079	8,000	8,913
24	224	250	282	40	8,913	10,000	11,220
25	282	315	355	41	11,220	12,500	14,130
26	355	400	447	42	14,130	16,000	17,780
27	447	500	562	43	17,780	20,000	22,390

3.4 Annoyance of Tonality

Sound annoyance is a complicated subjective concept that depends not only on the nature of sound, but also on other factors, such as the mood and physical state of the person, as well as previous experience. When the conditions are well standardized, more or less consistent results can be obtained with listening tests. In this way, it may be possible to formulate a computational model for annoyance based on psychoacoustic quantities. Loudness is often the main factor of annoyance, especially at high SPLs. A particularly disturbing sound can be experienced if a person is performing a task that needs concentration. [27]

In psychoacoustics, tonality is a quantity that reflects how much the sound stimulus has the characteristics of a pure tone. Tonality is low in noisy sounds and high if the sound contains prominent discrete tones or narrowband components, which sound energy is centered around a small range of frequencies. The term tonality also occurs in music theory, but it is not to be confused with the one in psychoacoustics. [22]

Tonal noises can cause unpleasant user experiences and lead to increased complaints by customers [28]. Commonly, tonal sounds are emitted by devices that includes rotating parts, for example, hard disk drives, wind turbines, fans and pumps. The presence of tonal components in a noise signal can be estimated using several different methods. A straightforward method is to carry out a third octave analysis and compare the SPL in each band with the levels in the adjacent bands. This method is described in ISO 1996-2 Annex D [29]. The criterion for tonality depends significantly on the frequency range. For low frequency bands (25 to 125 Hz) the difference of 15 dB is required, whereas for middle and high frequency bands the corresponding values are 8 dB and 5 dB respectively. In this context middle and high frequency ranges are 160 to 400 Hz and 500 to 10,000 Hz.

The method mentioned above is adopted into the noise regulations of many countries and a 5-dB penalty is added to adjust the overall noise levels when tonality occurs [30, 31, 32]. This gives one an idea of the relative magnitude of annoyance of tonal sounds. However, the method has been criticized because it may not detect tonal components, especially if the narrowband sound is located at the edge of a band and the energy is split into two different bands. It is also questionable how the addition of 5 dB will reflect the annoyance perception. Several other methods have been developed to compensate the shortcomings of third octave method. These methods are based on the narrow-band analysis. This may be information in 1/24 octaves or fast Fourier transform (FFT) that provides a frequency resolution of 1 to 2 Hz.

In these methods, the tone correction factor varies from 0 to 6 dB according to the frequency of tones and the level differences between the band values [28, 30].

3.5 Determination of Sound Power based on ISO 3746

ISO can be used to determine the sound power of a noise source. The A-weighted SPLs are measured from a hemispherical measuring surface with 4 microphone positions. Then, the A-weighted SWL is calculated from measured values. The standard is suitable for all types of noise sources and can be used in cases where standards ISO 3741...3745 are not suitable or desirable due to their excessive effort [33]. The standard provides results that can be used to compare the noise of equipment of a similar size and function, although it is less accurate than other ISO standards used to determine sound power.

3.5.1 Microphone positions

The microphone positions lie on the hypothetical hemispherical surface of radius r and area S, enveloping the source and terminating on the reflecting plane. The microphone positions referring to Figure 3.3 are listed in Table 3.5. The center of the hemisphere is the vertical projection on the reflecting plane of the geometrical center of the source. The radius of the hemisphere is at least twice the major source dimension, that is, at least twice the largest dimension of the reference box (l_1, l_2 or l_3). The value of the radius, in meters, is to be rounded to the next higher integer.

Table 3.5 *Coordinates of measurement positions referring to Figure 3.3.*

Microphone position	Microphone at height $z = 0.6\,r$		
	$\frac{x}{r}$	$\frac{y}{r}$	$\frac{z}{r}$
1	0.8	0.0	0.6
2	0.0	0.8	0.6
3	- 0.8	0.0	0.6
4	0.0	- 0.8	0.6

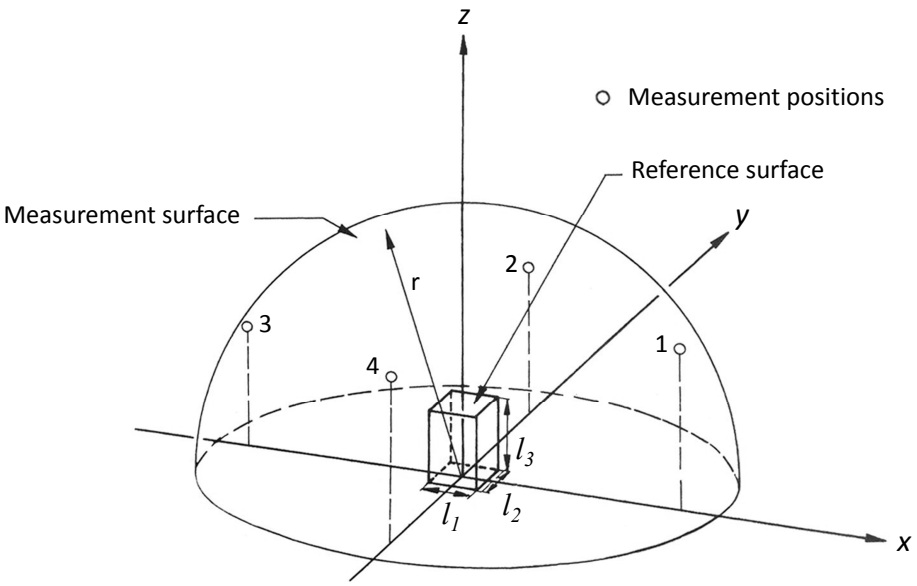

Figure 3.3 *Microphone array on the hemisphere.*

3.5.2 Correction of sound pressure levels for the background noise

After appropriate orientation of the device relative to the hemispherical microphone array, the A-weighted sound pressure levels are measured at each of the 4 microphone positions of the array. After correction are applied for background noise, these data are used for the calculation of the surface SPL, and further for SWL, according to Sections 3.5.3 and 3.5.4.

3.5.3 Calculation of Surface Sound Pressure Level

An A-weighted *surface sound pressure level* $\overline{L_{pA}}$ is calculated from measured values of the A-weighted SPLs after corrections are applied according to Section 3.5.2, by using the equation

$$\overline{L_{pA}} = 10 \log_{10} \left[\frac{1}{N} \sum_{i=1}^{N} 10^{L_{pAi}/10} \right] \tag{3.8}$$

where L_{pAi} is A-weighted sound pressure level at the i^{th} measurement position in decibels, and N is total number of measurement positions.

Table 3.6 *Correction for background noise.*

Difference between sound pressure level measured with sound source operating and background sound pressure level alone **(dB)**	**Correction to be subtracted from sound pressure level measured with sound source operating to obtain sound pressure level due to sound source alone** **(dB)**
3	3
4	2
5	2
6	1
7	1
8	1
9	0.5
10	0.5
> 10	0.0

3.5.4 Calculation of Sound Power Level

The A-weighted sound power level of the source shall be calculated from the equation

$$L_{WA} = \left(\overline{L_{pA}} - K\right) + 10\log_{10}\frac{S}{S_{ref}} \tag{3.9}$$

where K is the environmental correction, S is the area of the measurement surface, and S_{ref} is the reference area that equals to one square meter. For the hemispherical measurement surface, S is given by

$$S = 2\pi r^2 \tag{3.10}$$

where r is the radius of the hemispherical surface.

The environmental correction K accounts for the influence of undesired sound reflections from room boundaries and reflecting objects near the source under test. The magnitude of this term depends on the ratio of the sound absorption area A of the test room to the area S of the measurement surface. The environmental correction in decibels is given by

$$K = 10 \log_{10} \left[1 + \frac{4}{A/S} \right] \tag{3.11}$$

The mean acoustic absorption coefficient α of the surfaces of the room is estimated by using Table 3.7. The sound absorption area is given by

$$A = \alpha S_V \tag{3.12}$$

where S_V is the total area of the surface of the test room (walls, ceiling and floor).

Table 3.7 *Approximate values of the mean acoustic absorption coefficient.*

Mean acoustic absorption coefficient α	**Description of room**
0.05	Nearly empty room with smooth hard walls made of concrete, brick, plaster or tile
0.1	Partly empty room, room with smooth walls
0.15	Room with furniture, rectangular machinery room, rectangular industrial room
0.2	Irregularly shaped room with furniture, irregularly shaped machinery room or industrial room
0.25	Room with upholstered furniture, machinery or industrial room with a small amount of acoustical material (for example, partially absorptive ceiling) on ceiling or walls
0.35	Room with acoustical materials on both ceiling and walls
0.5	Room with large amounts of acoustical materials on ceiling and walls

3.6 Noise of Gas Flows

The sound generated by an unsteady gas flow or its interaction with solid bodies is called *aerodynamic sound* and is a very common by-product of industrial processes. Such flows often tend to excite structural modes of vibration in surrounding walls. Hence, the wall becomes a sound radiating surface and the flow acts as a time-varying disturbance. This is called *structure-borne sound*.

The flow-induced sound generation increases exponentially with the flow velocity. Sound can be a result of vorticity or intermittent fluctuations in the flow. Vorticity occurs when the fluid flows through a nozzle or a pipe and is mixed with the stationary fluid, when the flow interacts with an obstacle, or when the piping includes discontinuities. [20]

The mechanism of sound generation varies with the Mach number (see Section 4.2.2) of the mean-flow. The lowest Mach numbers occur, for example, in air condition systems and underwater applications, whereas the supersonic flows with high Mach number relate to high-pressure valves and jet engines. A monopole, a dipole and a quadrupole are the basic source types of subsonic flows ($M < 1$) to be discussed next. In addition, aeroacoustics of cavity flows will be introduced. Much of this theory refers to [21].

3.6.1 Aerodynamic monopole, dipole and quadrupole

The sound power radiated by a monopole source is equivalent to the radiation emitted by a pulsating spherical surface in a stationary fluid. Typical examples of a monopole source are turbulent flow through a relatively small orifice in a wall, which induces pulsating motion, and a resonance phenomenon. For unsteady flow, the radiated sound power of the monopole is dependent on the flow parameters as follows:

$$W_{monopole} \propto \frac{\rho L^2 U^4}{c} = \rho L^2 U^3 M \tag{3.13}$$

where ρ is mean density of gas, L is length scale of flow in source region, U is mean-flow velocity in source region, c is speed of sound in gas, and M is the Mach number. A dipole source is equivalent to two monopoly source that are in the opposite phase and their distance from each other is much smaller than the wavelength of the sound. When unsteady flow interacts with a surface, the source type is typically a dipole. Moreover, dipole source is in question when a fluid flows past a solid object, such as an airfoil or a telegraph wire, and vortex shedding takes place generating tonal sound. For a dipole source, the dependency on flow parameters is

$$W_{dipole} \propto \frac{\rho L^2 U^6}{c^3} = \rho L^2 U^3 M^3 \tag{3.14}$$

A dipole source is less efficient in comparison to monopole since it suffers from interference between the monopoles. Thus, the shape of the radiation field is figure

eight, as illustrated in Table 3.8. However, Curle [34] showed the dominance of the dipole source for the low Mach number flows. Where a dipole source consists of monopoles, a quadrupole source is similarly a combination of two equal and opposite dipoles. Again, the radiation efficiency is weaker than in the case of a dipole source due to the double cancellation. Quadrupole sources arise from Reynolds stresses in turbulent fluid motion and dominate the sound production in high-speed subsonic flows where the flow does not interact with obstacles. This is found, for instance, in the turbulent mixing layer of a jet. The connection between the sound power of the quadrupole source and the flow is given by

$$W_{quadrupole} \propto \frac{\rho L^2 U^8}{c^5} = \rho L^2 U^3 M^5 \tag{3.15}$$

which differs from the power output of the dipole source by a factor of M^2. The same difference exists between a monopole and dipole source.

Provided that the source type in question is known, one can use the proportionality relations 3.13, 3.14, and 3.15 to predict the reaction of the sound source to chances in the flow parameters, especially in velocity. In these relations, the value of the constant varies with the mechanism by which the sound is generated as well as the flow configuration.

3.6.2 Cavity flows

A frequent cause for irritating flow-induced noise is flow past a cavity. This phenomenon is about a cavity or an opening in a wall, similar to those shown in Figure 3.4, which is passed by shear flow. Examples of such noise are found in automobiles [35, 36] and other high-speed vehicles. Roughly speaking, the subject can be divided into two groups, Helmholtz resonators and Rossiter's model for rectangular cavities. Both models provide natural frequencies, being incapable to estimate the acoustic power of the source, though.

Cavity of Uniform Cross Section

Resonant cavity oscillation is generally explained by a feedback loop, where flow separates from the upstream edge inducing vortices that impinge on the downstream corner causing pressure perturbations, which emanate back to upstream furthering flow separation, closing the loop. The wave resonance may be longitudinal or it may

Table 3.8 *Aeroacoustical source types, based on [21].*

Source type	Radiation characteristic		Directivity pattern	Radiated power is proportional to
	180° phase difference			
Monopole	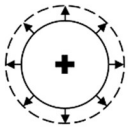	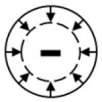	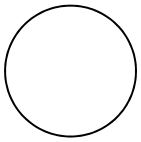	$\rho L^2 \frac{U^4}{c}$
Dipole	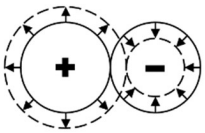	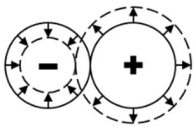	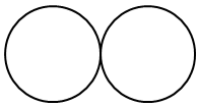	$\rho L^2 \frac{U^6}{c^3}$
Quadrupole	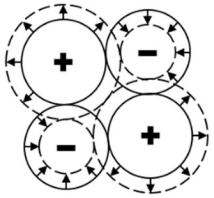	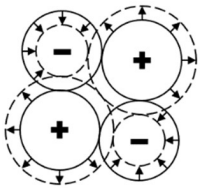	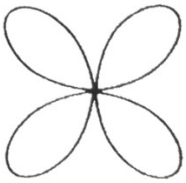	$\rho L^2 \frac{U^8}{c^5}$

occur in a depth-oriented manner. The former occurs in the case of a shallow cavity ($L/D > 1$), while the latter is observed more likely in deep cavities ($L/D < 1$). To make this phenomenon arise, sufficiently short acoustical wavelengths are required as to make standing waves possible inside the cavity. Thus, the conditions are $c/f \leq 2L$ for longitudinal resonance and $c/f \leq 4D$ for depthwise resonance. [21]

The frequency can be estimated by Rossiter's model [38] for *longitudinal* cavity resonance modes:

$$St = \frac{fL}{U} = \frac{m - \xi}{M + 1/k_v} \tag{3.16}$$

where k_v is ratio of shear layer velocity to free-stream velocity ($= U_c/U \cong 0.57$), m is dimensionless mode number (=1,2,3,), ξ is empirical constant (=0.25), and L is cavity length. St refers to Strouhal number (see Section 4.2.3).

East [39] developed the following equation for the *depthwise* cavity modes:

$$\frac{fL}{U} = \left(\frac{1}{M}\right)\left(\frac{1}{D}\right)\left(\frac{0.25}{1+0.65(L/D)^{0.75}}\right) \tag{3.17}$$

where L/D is length-to-depth ratio.

Block [40] merged earlier results providing an equation which can be used to estimate the flow velocity at which the tonal noise is aroused. Then, the Mach number of the cavity flow is given by

$$M = \frac{1.75\ L/D}{4m\left[1+0.65(L/D)^{0.75}\right] - [(L/D)+0.514]} \tag{3.18}$$

which is valid for $L/D < 2$ and for Mach numbers in the range of 0.1 to 0.5.

Helmholtz resonator

A clear tone can be achieved by blowing air across the mouth of a bottle. This is an example of such a case where a large volume with just a little slot is subjected to the mean flow, called Helmholtz resonator. The resulting tone is of monopole type and its frequency is not dependent on the flow parameters, but, on the contrary, on geometry as follows:

$$f_n = \frac{c}{2\pi}\sqrt{\frac{A_o}{V_c L_{\text{eff}}}} \tag{3.19}$$

where c is speed of sound, A_o is orifice cross-sectional area, V_c is cavity volume, and L_{eff} is effective neck length of the orifice.

The acoustical length of the neck is slightly longer than its physical measure, and therefore an end correction is added. The effective neck length can be estimated by

$$L_{\text{eff}} = L_o + 0.48\sqrt{A_o} \tag{3.20}$$

where L_o is the neck length of the orifice.

(a) Rectangular cavity (b) Helmholtz resonator

Figure 3.4 *Geometry of rectangular cavity and Helmholtz resonator. [21]*

4. FLUID DYNAMICS

This chapter covers the fluid flow related theory applied in this thesis.

4.1 Conservation Laws

In this section, basic conservation laws are applied to an infinitesimal control volume. As a result, the differential equations of fluid motion are achieved. Derivation of the equations is based on White's book *Fluid Mechanics* [41].

4.1.1 The Differential Equation of Mass Conservation

Conservation of mass states that the mass of the system must remain constant over time. When this concept is applied to a very small elemental control volume (dx, dy, dz), as in Figure 4.1, all the basic differential equations can be derived.

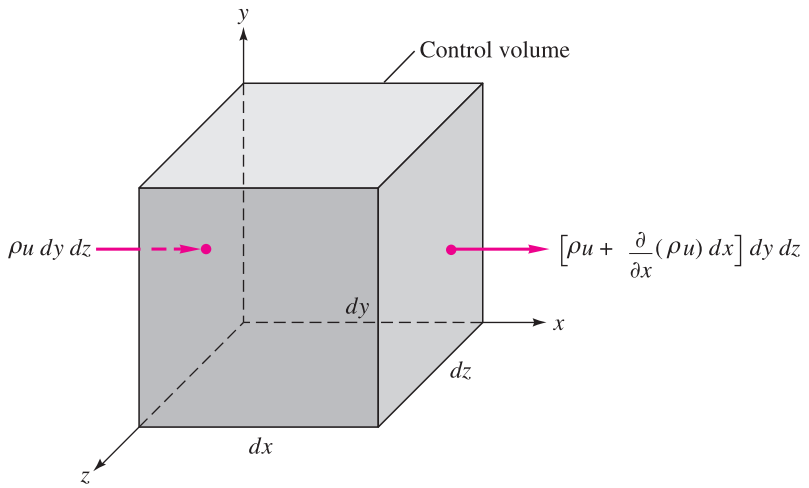

Figure 4.1 *Infinitesimal fixed control volume showing the inlet and outlet mass flows in the x-direction. [41]*

The flow through each side is assumed to be one-dimensional, and the mass flow terms occur on all six faces, three inlets and three outlets, although y- and z-directions are not tagged in the Figure 4.1.

The element volume cancels out of all terms, leaving a partial differential equation involving the derivatives of density and velocity. The desired result is conservation of mass for an infinitesimal control volume:

$$\frac{\partial \rho}{\partial t} + \frac{\partial (\rho u)}{\partial x} + \frac{\partial (\rho v)}{\partial y} + \frac{\partial (\rho w)}{\partial z} = 0 \tag{4.1}$$

where u, v and w are velocity components in x-, y- and z-directions, respectively. The flow may be either steady or unsteady, compressible or incompressible.

However, if the flow is assumed to be incompressible, the first term of the equation is reduced to zero. Density, as a constant, can be separated from the partial derivatives, and the continuity equation becomes

$$\frac{\partial u}{\partial x} + \frac{\partial v}{\partial y} + \frac{\partial w}{\partial z} = 0 \tag{4.2}$$

4.1.2 The Differential Equation of Momentum

In this section Newton's second law is derived for a moving fluid using the same elemental control volume as in Figure 4.1. Generally, Newton's second law states that the rate of change of momentum of a body is directly proportional to the force applied.

The momentum fluxes can now be formed by exact analogy with discussion that led to the equation for net mass flux. For example, inlet momentum flux on the left face is $\rho u \mathbf{V}\ dy\ dz$, and the x-direction gives

$$\sum F_x = \rho \left(\frac{\partial u}{\partial t} + u\frac{\partial u}{\partial x} + v\frac{\partial u}{\partial y} + w\frac{\partial u}{\partial z} \right) dx\ dy\ dz \tag{4.3}$$

Control volume is affected by two types of forces, surface forces and body forces. The latter are non-contact forces due to external fields, such as gravitation, whereas surface forces are due to the stresses on the sides of the control volume. Surface force can be decomposed into hydrostatic pressure p and viscous stresses τ_{ij}, thus

$$\sigma_{ij} = \begin{vmatrix} -p + \tau_{xx} & \tau_{yx} & \tau_{zx} \\ \tau_{xy} & -p + \tau_{yy} & \tau_{zy} \\ \tau_{xz} & \tau_{yz} & -p + \tau_{zz} \end{vmatrix} \tag{4.4}$$

The subscript notation for stresses is given in Figure 4.2(a). The gradients of these stresses cause a net force on the differential control surface. Figure 4.2(b) shows the stresses acting in x-direction only. For example, the leftward force $\sigma_{xx}\ dy\ dz$ on the left face is balanced by the force $(\partial\sigma_{xx}/\partial x)\ dx\ dy\ dz$ on the right face. This stands on the other four faces as well. When these stresses are split into pressure plus viscous stresses, the net surface force in the x-direction is given by

$$\frac{dF_{x,surf}}{dV} = -\frac{\partial p}{\partial x} + \frac{\partial \tau_{xx}}{\partial x} + \frac{\partial \tau_{yx}}{\partial y} + \frac{\partial \tau_{zx}}{\partial z} \tag{4.5}$$

where $dV = dx\ dy\ dz$.

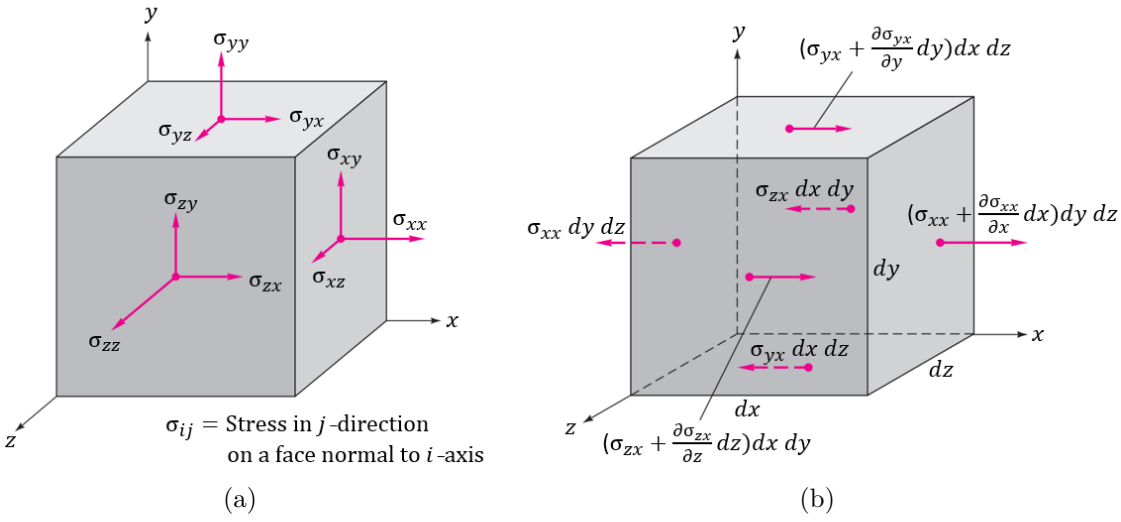

Figure 4.2 *Fixed control volume showing (a) the notation for stresses and (b) the surface force in the x-direction. [41]*

The gravity force acting on the elemental mass in the x-direction is given by

$$\frac{dF_{x,grav}}{dV} = \rho g_x\ dx\ dy\ dz \tag{4.6}$$

A fluid is said to be Newtonian in case the viscous stresses are proportional to the rates of deformation and the coefficient of viscosity μ. Then, for incompressible flow the normal components of viscous stresses are

$$\tau_{xx} = 2\mu\frac{\partial u}{\partial x} \qquad \tau_{yy} = 2\mu\frac{\partial v}{\partial y} \qquad \tau_{zz} = 2\mu\frac{\partial w}{\partial z} \tag{4.7}$$

The shear stresses are equal in pairs and are given by

$$\tau_{xy} = \tau_{yx} = \mu \left(\frac{\partial u}{\partial y} + \frac{\partial v}{\partial x} \right) \tag{4.8}$$

$$\tau_{xz} = \tau_{zx} = \mu \left(\frac{\partial w}{\partial x} + \frac{\partial u}{\partial z} \right) \tag{4.9}$$

$$\tau_{yz} = \tau_{zy} = \mu \left(\frac{\partial v}{\partial z} + \frac{\partial w}{\partial y} \right) \tag{4.10}$$

Finally, rearranging the viscous stresses and equations 4.3, 4.5 and 4.6 gives the differential momentum equation. The momentum equations in y- and z-directions can be derived in identical manner. This yields

$$\rho g_x - \frac{\partial p}{\partial x} + \mu \left(\frac{\partial^2 u}{\partial x^2} + \frac{\partial^2 u}{\partial y^2} + \frac{\partial^2 u}{\partial z^2} \right) = \rho \left(\frac{\partial u}{\partial t} + u\frac{\partial u}{\partial x} + v\frac{\partial u}{\partial y} + w\frac{\partial u}{\partial z} \right) \tag{4.11}$$

$$\rho g_y - \frac{\partial p}{\partial y} + \mu \left(\frac{\partial^2 v}{\partial x^2} + \frac{\partial^2 v}{\partial y^2} + \frac{\partial^2 v}{\partial z^2} \right) = \rho \left(\frac{\partial v}{\partial t} + u\frac{\partial v}{\partial x} + v\frac{\partial v}{\partial y} + w\frac{\partial v}{\partial z} \right) \tag{4.12}$$

$$\rho g_z - \frac{\partial p}{\partial z} + \mu \left(\frac{\partial^2 w}{\partial x^2} + \frac{\partial^2 w}{\partial y^2} + \frac{\partial^2 w}{\partial z^2} \right) = \rho \left(\frac{\partial w}{\partial t} + u\frac{\partial w}{\partial x} + v\frac{\partial w}{\partial y} + w\frac{\partial w}{\partial z} \right) \tag{4.13}$$

which are the Navier-Stokes equations for incompressible flow.

4.2 Essential Dimensionless Numbers

This section presents a few relevant dimensionless numbers.

4.2.1 Reynolds Number

The Reynolds number describes the flow regime by means of the ratio of inertial forces and viscous forces. The Reynolds number indicates whether the flow is laminar or turbulent, and is defined as

$$Re = \frac{\rho U L}{\mu} = \frac{U L}{\nu} \tag{4.14}$$

where L is a characteristic linear dimension, μ is the dynamic viscosity, and ν is the kinematic viscosity of the fluid. For laminar flow, viscous forces are dominant, while turbulent flow is dominated by inertial forces producing flow instabilities, such as eddies and vortices.

Different types of flow have different limits for transition from laminar to turbulent, but generally, however, the turbulence of the flow increases as the Reynolds number increases. For example, for flow in a pipe of diameter D, laminar flow occurs when $Re_D < 2300$, whereas turbulent flow takes place at $Re_D > 2600$. This result is generalized to non-circular channels using the hydraulic diameter. Thus, a transition Reynolds number can be calculated for other shapes of channel. The characteristic dimension L for flow between two plane parallel surfaces (where the width is much greater than the distance between the plates) is equal to the distance between the plates.

4.2.2 Mach Number

The Mach number is defined as the ratio of flow velocity and the local speed of sound in the following way:

$$M = \frac{u}{c} \tag{4.15}$$

where u is the local flow velocity and c is the local speed of sound in the medium.

Primarily, the Mach number is used to estimate whether a flow can be treated as an incompressible, which denotes that the density of a fluid parcel persists constant during its motion. A value of incompressible flow is the mathematically easier modelling.

Usually, when $M < 0.3$, compressibility has a minor effect and airflow can be modelled as an incompressible flow.

4.2.3 Strouhal Number

The Strouhal number is a dimensionless value useful for analysing oscillating unsteady fluid flow dynamics problems. It contains a ratio of the inertial forces due to the unsteadiness of the flow to the inertial forces due to changes in velocity from one point to another in the flow field. The Strouhal number can be expressed as

$$St = \frac{fL}{U} \tag{4.16}$$

where f is the frequency of vortex shedding and L is characteristic length.

Some examples are flow around a cylinder, or flow around a stone in a river. In the case of a cylinder, experiments have shown that the Strouhal number is approximately constant over a wide range of Reynolds numbers. The Strouhal number may be useful when estimating the frequency of a tonal peak produced by vortex shedding.

4.3 Turbulent Flow

Virtually, all macroscopic fluid flows in nature and engineering applications are turbulent. This kind of flow regime is characterized by rapid changes in pressure and flow velocity. Turbulent flow is three-dimensional with increased mixing of the substance, whereby, for example, heat transfer and mixing of chemical concentrations are greatly enhanced in contrast to laminar flow.

For laminar flow, no oscillations occur and the streamlines do not cross each other. Thus, drag due to friction effects is decreased and, for example, the energy needed to pump fluid through a pipeline is decreased. For these reasons, turbulence provides both benefits and disadvantages simultaneously in many applications. For instance, in air-breathing combustion systems, turbulence is desired for better mixing of the reactants but, at the same time, there is a hindrance of noise and friction loss.

Turbulent flow is not easy to define unequivocally, however, some of the basic features of turbulence are:

- **High Reynolds number**
  High Reynolds number refers to strong turbulence. Once the critical Re value is exceeded small perturbations may grow spontaneously.
- **Fluctuations**
  Turbulent flow includes fluctuations that behave unpredictable, irregular, and chaotic. These fluctuations occur in the dependent-field quantities such as pressure, velocity, temperature, etc.
- **Vorticity**
  One of the main features of turbulence is diverse collection vortices of various

sizes that spin, divide and deform. Rotational structures in a turbulent flow are called eddies, which turbulence always contains. The size range of eddies in-creases with increasing Reynolds number.

- **Dissipation**
  The largest eddies absorb kinetic energy from the mean flow transferring it to smaller and smaller scales, until velocity gradients become so high that the energy is converted into heat through viscosity. Hence, to maintain turbulence, continuous supply of energy is required.

- **Diffusivity**
  Turbulent flow is characterized by increased diffusivity due to the macroscopic mixing of fluid particles.

4.4 Boundary Layer

A boundary layer is layer of a certain thickness close to the surface, separating the surface and the freestream from each other. In the boundary layer, the viscous forces play a significant role and the flow velocity drops steeply when moving from the free flow region to the surface. Generally, it is eligible to assume that the flow velocity for viscous fluids is zero at the surface (no-slip condition). The velocity increases when moving from the surface towards the freestream, and it is agreed that the thickness of the boundary layer δ is the distance where the flow velocity has reached 99 per cent of the free flow rate. The thickness of the boundary layer depends on flow type (laminar or turbulent), properties of flow and the geometry of the case.

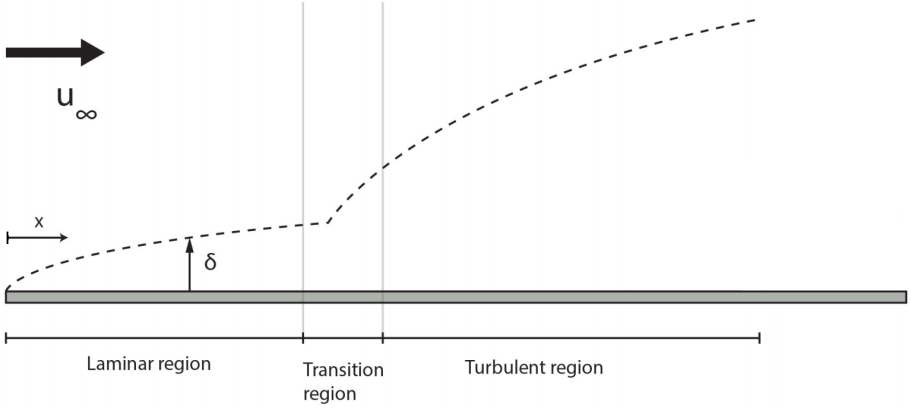

Figure 4.3 *Boundary layer on a flat plate.*

Laminar boundary layer occurs at low Reynolds numbers only. The thickness of boundary layer increases with the distance from the leading edge (parameter x in

Figure 4.3). At a certain point, the flow becomes unstable and the transition area is reached. As the distance x increases, the flow finally becomes turbulent.

In any case of a turbulent boundary layer, there is a thin layer nearest the surface, called the *laminar sublayer* or the *viscous sublayer*, where the flow is laminar and dominated by viscous forces. The viscous sublayer is bordered by *buffer layer* from the freestream side. Further, when moving away from the surface, there is a logarithmic region, also referred to as the fully turbulent region. These layers occur at a certain dimensionless distance of y^+ from the wall. A graphical representation of the law of the wall is shown in Figure 4.4

For the logarithmic law region

$$u^+ = \frac{1}{\kappa} \ln y^+ + C \tag{4.17}$$

with

$$y^+ = \frac{u_\tau y}{\nu}, \qquad u_\tau = \sqrt{\frac{\tau_w}{\rho}}, \qquad u^+ = \frac{u}{u_\tau} \tag{4.18}$$

where y^+ is the dimensionless distance to the wall, u_τ is the friction velocity, y is distance to the wall, τ_w is the wall shear stress, u^+ is the dimensionless velocity, and u is the velocity parallel to the wall. Equation 4.17 includes two constants, the Von Kármán constant κ and a constant C, which are found to be $\kappa \approx 0.41$, and for a smooth wall $C \approx 5.0$.

In the region of the laminar sublayer, which is in the range $y^+ < 5$, the friction velocity is written as

$$u^+ = y^+ \tag{4.19}$$

Modelling of the boundary layer is an essential part of the flow simulation, and is further discussed in Section 4.5.2.

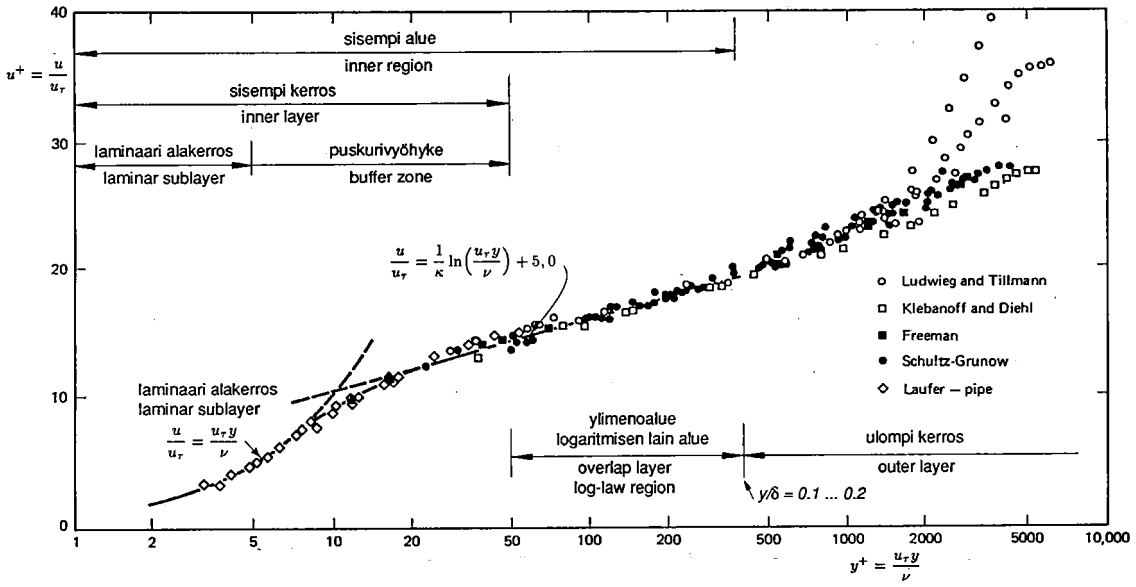

***Figure** 4.4 Law of the wall for turbulent boundary layer. [42]*

4.5 Turbulence Modelling

The most accurate numerical way to describe turbulent flow is to execute Direct Numerical Simulation (DNS), that is, to solve the Navier-Stokes equations numerically without any simplifications. However, this kind of processing is practically infeasible due to the lack of computing power, with the exception of simple flows with low Reynolds numbers, and is mainly used in academic studies. Hence, turbulence models (i.e. approximations of the Navier-Stokes equations) are used to predict the effects of turbulence. Normally, turbulence models are categorized according to their mathematical description, into Reynolds-avergaed-Navier-Stokes equations (RANS equations), hybrid models, Large Eddy Simulation (LES) and DNS.

For most engineering purposes it is unnecessary to resolve the details of the turbulent fluctuations. Then, a general way to proceed is to divide the flow variables of turbulent flow into the mean component and the fluctuating component. For instance, a time-dependent velocity component $u(t)$ can be divided in a following way:

$$u(t) = \overline{u} + u'(t) \tag{4.20}$$

where $\overline{u}$ is the mean velocity and $u'(t)$ is the fluctuating component. In Figure 4.5, this is graphically illustrated. The theory of turbulence modelling presented in this chapter is derived from ANSYS Fluent Theory Guide [43].

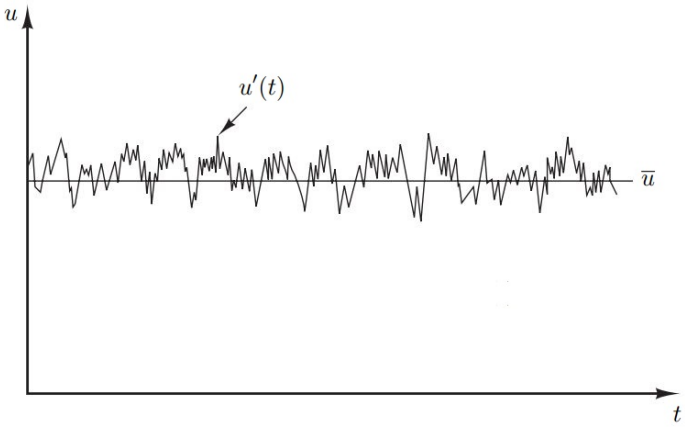

Figure 4.5 *Splitting turbulent flow variable into the mean component and the fluctuating component.*

When the presumption (i.e. equation 4.20) is applied to Navier-Stokes equations 4.11, 4.12, 4.13, a new system of equations is obtained, with the additional term $-\overline{\rho u_i' u_j'}$, generally referred to as the Reynolds stress. The system of equations is called Reynolds-averaged Navier-Stokes equations (RANS). This nonlinear Reynolds stress term requires additional modelling to close the RANS equations for solving, and has led to the generation of many different turbulence models.

The oldest approach of modelling Reynolds stresses has proved to be an important part of most functional turbulence models. Boussinesq's eddy viscosity concept is based on an analogy between molecular and turbulent motion. In this model, the additional turbulence stresses are given by augmenting the molecular viscosity with an eddy viscosity. Turbulent swirls are treated as liquid bodies that collide and transfer momentum to each other. Thus, Reynolds stresses are modelled like molecular friction

$$-\overline{\rho u_i' u_j'} = \mu_t \left(\frac{\partial u_i}{\partial x_j} + \frac{\partial u_j}{\partial x_i} \right) - \frac{2}{3} \rho k \delta_{ij} \tag{4.21}$$

where μ_t is the turbulence eddy viscosity and k is the turbulence kinetic energy

$$k = \frac{1}{2} \overline{u_i' u_i'} \tag{4.22}$$

Models of this type are known as eddy viscosity models. Next, the so-called two equation models used in this work are presented.

4.5.1 Two Equation Turbulence Models

In turbulence modelling, two equation models are a very common way to approach almost any problem. Models like the k-ε model and the k-omega model have become industry standard models and are commonly used for most types of engineering problems.

These models include two extra transport equations to represent the turbulent properties of the flow. Most often one of the transported variables is the turbulent kinetic energy k. The second transported variable varies depending on what type of two-equation model it is. Common choices are the turbulent dissipation ε, or the specific turbulence dissipation rate ω.

The second variable can be thought of as the variable that determines the scale of the turbulence (length-scale or time-scale), whereas the first variable, k, determines the energy of it.

Standard k-epsilon model

Standard k-ε model is the most common model used in CFD to simulate mean flow characteristics for turbulent flow conditions.

The model includes two additional partial differential equations to solve the turbulence closure problem. The first transported variable is the turbulence kinetic energy k. The second transported variable is the rate of dissipation of turbulence energy ε.

For eddy viscosity

$$\mu_t = \rho C_\mu \frac{k^2}{\varepsilon} \tag{4.23}$$

For turbulent kinetic energy k

$$\frac{\partial}{\partial t}(\rho k) + \frac{\partial}{\partial x_i}(\rho k u_i) = \frac{\partial}{\partial x_j}\left[\left(\mu + \frac{\mu_t}{\sigma_k}\right)\frac{\partial k}{\partial x_j}\right] + G_k - \rho\varepsilon \tag{4.24}$$

For dissipation

$$\frac{\partial}{\partial t}(\rho\varepsilon) + \frac{\partial}{\partial x_i}(\rho\varepsilon u_i) = \frac{\partial}{\partial x_j}\left[\left(\mu + \frac{\mu_t}{\sigma_\varepsilon}\right)\frac{\partial \varepsilon}{\partial x_j}\right] + C_{1\varepsilon}\frac{\varepsilon}{k}G_k - C_{2\varepsilon}\rho\frac{\varepsilon^2}{k} \tag{4.25}$$

where G_k represents the generation of turbulence kinetic energy due to the mean velocity gradients as follows:

$$G_k = -\rho\overline{u_i' u_j'}\frac{\partial u_j}{\partial x_i} = \mu_t S^2 \tag{4.26}$$

$$S \equiv \sqrt{2S_{ij}S_{ij}} \tag{4.27}$$

The equations also consist of five adjustable constants. The values of these constants have been arrived at by numerous iterations of data fitting for a wide range of turbulent flows. These are shown in Table 4.1.

Table 4.1 *Standard k-ε model constants.*

C_μ	$C_{1\varepsilon}$	$C_{2\varepsilon}$	σ_k	σ_ε
0.09	1.44	1.92	1.0	1.3

The k-ε model has been used successfully for many two and three dimensional flow cases. The overall prevalence of the constants given in Table 4.1 can not be expected because there are so many assumptions in the model that it is not possible to imagine all of them being valid in every practical flow situation.

Experience has shown that even some fairly simple cases require at least one constant value to be adjusted. The suitability of the model can be extended by replacing any of the constants with the functions of the appropriate flow parameters.

Realisable k-epsilon model

The realisable k-ε model differs from the standard model with two major factors. Firstly, the turbulent viscosity is modelled differently, and for the second, the transport equation for the dissipation rate is based on the dynamic equation of the mean-square vorticity fluctuation. The term *realisable* suggests that the model meets certain mathematical limits for Reynolds stresses, therefore being consistent with the physics of turbulent flow.

The advantage of the realisable k-ε model is the better modelling of the spreading rate for jets. In addition, the model's ability to predict flows with separation and recirculation is more advanced.

The transport equation for dissipation is

$$\frac{\partial}{\partial t}(\rho\varepsilon) + \frac{\partial}{\partial x_j}(\rho\varepsilon u_j) = \frac{\partial}{\partial x_j}\left[\left(\mu + \frac{\mu_t}{\sigma_\varepsilon}\right)\frac{\partial \varepsilon}{\partial x_j}\right] + \rho C_1 S\varepsilon - \rho C_2 \frac{\varepsilon^2}{k + \sqrt{\nu\varepsilon}} \tag{4.28}$$

where

$$C_1 = \max\left[0.43, \frac{\eta}{\eta + 5}\right], \quad \eta = S\frac{k}{\varepsilon}, \quad S = \sqrt{2S_{ij}S_{ij}} \tag{4.29}$$

Unlike in the standard model, C_μ is not a constant but a variable

$$C_\mu = \frac{1}{A_0 + A_S \frac{kU^*}{\varepsilon}} \tag{4.30}$$

where

$$U^* \equiv \sqrt{S_{ij}S_{ij} + \widetilde{\Omega}_{ij}\widetilde{\Omega}_{ij}} \tag{4.31}$$

$$\widetilde{\Omega}_{ij} = \Omega_{ij} - 2\varepsilon_{ijk}\omega_k \tag{4.32}$$

$$\Omega_{ij} = \overline{\Omega_{ij}} - \varepsilon_{ijk}\omega_k \tag{4.33}$$

$$A_0 = 4.04, \quad A_S = \sqrt{6}\cos\phi \tag{4.34}$$

$$\phi = \frac{1}{3}\cos^{-1}\left(\sqrt{6}\ W\right), \quad W = \frac{S_{ij}S_{jk}S_{ki}}{\widetilde{S}^3} \tag{4.35}$$

$$\widetilde{S} = \sqrt{S_{ij}S_{ij}}, \qquad S_{ij} = \frac{1}{2}\left(\frac{\partial u_j}{\partial x_i} + \frac{\partial u_i}{\partial x_j}\right) \tag{4.36}$$

The constants of the realisable k-ε model are shown in Table 4.2.

Table 4.2 *Realisable k-ε model constants.*

C_2	σ_k	σ_ε
1.9	1.0	1.2

SST k-omega model

The shear stress transport (SST) k-ω model was developed by Menter [44] based on the standard k-ω model and k-ε model. The transported variables are the turbulent kinetic energy k and the specific turbulence dissipation rate ω.

Near the walls, in the inner part of the boundary layer, the standard k-omega model can be used even in the viscous sub-layer. Thus, the SST k-omega model is a valid Low-Re turbulence model without extra damping functions.

For kinematic eddy viscosity

$$\nu_T = \frac{a_1 k}{\max(a_1\omega, SF_2)} \tag{4.37}$$

Transport equations for kinetic energy

$$\frac{\partial k}{\partial t} + U_j\frac{\partial k}{\partial x_j} = G_k - \beta^* k\omega + \frac{\partial}{\partial x_j}\left[(\nu + \sigma_k\nu_T)\frac{\partial k}{\partial x_j}\right] \tag{4.38}$$

For the specific dissipation rate

$$\frac{\partial \omega}{\partial t} + U_j\frac{\partial \omega}{\partial x_j} = \alpha S^2 - \beta\omega^2 + \frac{\partial}{\partial x_j}\left[(\nu + \sigma_\omega\nu_T)\frac{\partial \omega}{\partial x_j}\right] + 2(1-F_1)\sigma_{\omega 2}\frac{1}{\omega}\frac{\partial k}{\partial x_i}\frac{\partial \omega}{\partial x_i} \tag{4.39}$$

Closure coefficients and auxiliary relations are given by

$$F_2 = \tanh\left[\left[\max\left(\frac{2\sqrt{k}}{\beta^*\omega y}, \frac{500\nu}{y^2\omega}\right)\right]^2\right] \tag{4.40}$$

$$G_k = \min\left(\tau_{ij}\frac{\partial U_i}{\partial x_j}, 10\beta^* k\omega\right) \tag{4.41}$$

$$F_1 = \tanh\left\{\left\{\min\left[\max\left(\frac{\sqrt{k}}{\beta^*\omega y}, \frac{500\nu}{y^2\omega}\right), \frac{4\sigma_{\omega 2}k}{CD_{k\omega}y^2}\right]\right\}^4\right\} \tag{4.42}$$

$$CD_{k\omega} = \max\left(2\rho\sigma_{\omega 2}\frac{1}{\omega}\frac{\partial k}{\partial x_i}\frac{\partial \omega}{\partial x_i}, 10^{-10}\right) \tag{4.43}$$

$$\phi = \phi_1 F_1 + \phi_2(1 - F_1) \tag{4.44}$$

In Table 4.3, the constants of the SST k-ω model are listed.

Table 4.3 *SST k-ω model constants.*

α_1	α_2	β_1	β_2	β^*	σ_{k1}	σ_{k2}	$\sigma_{\omega 1}$	$\sigma_{\omega 2}$
$^5/_9$	0.44	$^3/_{40}$	0.0828	$^9/_{100}$	0.85	1	0.5	0.856

The common problem with the standard k-omega model is hypersensitivity to the free-stream turbulence properties outside the boundary layer. In this area, the SST model behaves like the k-ε model.

The SST model produces slightly too intensive turbulence in regions where large normal strain occurs, such as stagnation regions and strong acceleration regions. However, the SST k-ω model is considered as a good option for adverse pressure gradient cases and modelling of separating flow.

4.5.2 Near-Wall Treatments

Walls have a significant effect on turbulent flow. The modelling of a turbulent boundary layer has a great impact on the success of the solution, as the walls act as a source of turbulence and vorticity. In the vicinity of the walls, steep gradients appear in the solution variables. Ultimately, this is a crucial factor in simulating the wall-bounded turbulent flows.

There are two alternative ways to model the near-wall region. One option is to use such turbulence models that allow the boundary layer to be modelled through the viscous sublayer all the way to the wall. In this case, a proper mesh refinement is necessary near the wall. This approach is commonly referred to as near-wall modelling.

In another approach, the viscous sublayer and buffer layer is treated with so-called wall functions, and these regions will not be resolved at all. By means of wall functions, the logarithmic region and the values of flow variables on the wall are coupled together. The use of wall functions is initiated from the outside of the viscous sublayer and the buffer zone. These approaches are shown in Figure 4.6.

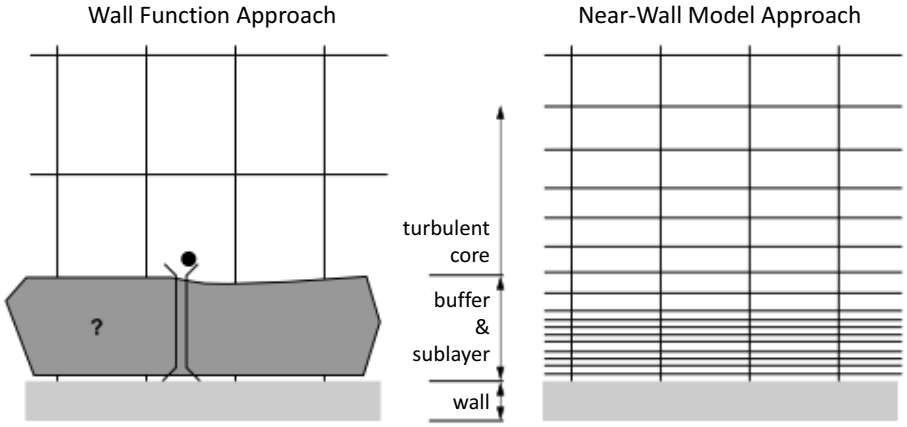

Figure 4.6 *Wall treatment approaches. [43]*

Standard Wall Functions

Limitations of the wall function approach:

In ANSYS Fluent, the standard wall functions are based on the law of the wall, which was presented earlier in Section 4.4. The logarithmic law now has the form

$$U^* = \frac{1}{\kappa} \ln (Ey^*) \tag{4.45}$$

where U^* is the dimensionless velocity, so that

$$U^* \equiv \frac{U_P C_\mu^{0.25} k_P^{0.5}}{\tau_w / \rho} \tag{4.46}$$

and y^* is the dimensionless distance to the wall

$$y^* \equiv \frac{\rho C_\mu^{0.25} k_P^{0.5} y_P}{\mu} \tag{4.47}$$

In equations 4.45 - 4.47, E is empirical constant, U_P is mean velocity at the wall-adjacent cell centroid, y_P is distance between the centroid of the wall-adjacent cell and the wall, and k_P is turbulence kinetic energy at the wall-adjacent cell centroid.

The region where the wall functions are valid is always case-specific depending on the Reynolds number. However, the lower limit invariably lies at $y^* \approx 15$. Typically, the wall functions do not satisfy with lower values of y^* and the quality of the solution might be weak. In ANSYS Fluent, the limit value for the logarithmic law is set to $y^* = 11.225$, below which the laminar stress-strain relationship is used

$$U^* = y^* \tag{4.48}$$

In k-ε models, the kinetic energy equation is solved all over the domain. The wall-adjacent cells are included and the boundary condition is set at the wall as

$$\frac{\partial k}{\partial y} = 0 \tag{4.49}$$

Calculation of the production of turbulent kinetic energy G_k and the dissipation rate ε is based on the local equilibrium hypothesis so in the wall-adjacent cells the production G_k and dissipation ε are assumed to be equal. The production is computed from

$$G_k \approx \tau_w \frac{\partial U}{\partial y} = \tau_w \frac{\tau_w}{\kappa \rho C_\mu^{0.25} k_P^{0.5} y_P} \tag{4.50}$$

and the dissipation is computed from

$$\varepsilon_P = \frac{C_\mu^{\frac{3}{4}} k_P^{\frac{3}{2}}}{\kappa y_P} \tag{4.51}$$

Scalable Wall Functions

Standard wall functions operate poorly when used below the logarithm region. If $y^* < 11$ in the wall-adjacent cell, the scalable wall functions virtually increase the cell size of the near-wall mesh. This is achieved simply by using a limiter function instead of y^* alone such that

$$\tilde{y}^* = \max\left(y^*, y^*_{limit}\right) \tag{4.52}$$

where $y^*_{limit} = 11.225$. In other respects, the scalable wall functions operates identically with the standard wall functions.

Two-Layer Model and Enhanced Wall Treatment

Enhanced Wall Treatment is a near-wall model approach where the two layer model is combined with so-called enhanced wall functions. The viscous sublayer is resolved, provided that the mesh near the wall is fine enough. A suitable indicator for this is the value of $y^+ \approx y^* \approx 1$. This method is identical to the two-layer zonal model. Enhanced wall function is a system, which works to improve the solution in the situation where the closest near-wall node lies neither in the log-law region, nor at the distance of $y^* \approx 1$ from the wall, but between these two regions.

The idea of the two-layer approach and is to subdivide the boundary layer into the viscosity-affected region and the log-law region. The wall-distance-based turbulent Reynolds number is written as

$$Re_y \equiv \frac{\rho y \sqrt{k}}{\mu} \tag{4.53}$$

Here, the log-law region is defined as $Re_y > 200$. In this region, the k-ε models are used, whereas in the near-wall region the one-equation model is employed, and the dissipation field is calculated from

$$\varepsilon = \frac{k^{\frac{3}{2}}}{l_\varepsilon} \tag{4.54}$$

where l_ε is a length scale of turbulence dissipation rate. Mixing functions are em-

ployed between these two regions for smooth transition of the turbulence quantities.

4.6 Flow Through Openings

This section deals with steady-state flow through adventitious openings. Two equations are principally used to represent such openings, the power law and quadratic equations. Both equations give good agreement at the region where the measurements are usually performed ($\Delta p > 10$ Pa). At lower pressures, the differences between the two equations are most remarkable [9]. A more detailed assessment may therefore be required if the measurement data are to be extrapolated up to very small pressure differences.

The power law is presented here for its simplicity and popularity.

4.6.1 The Power Law

For ventilation openings, the so-called power law is the most commonly used equation to describe the relationship between pressure drop and flow rate [9]

$$q = \alpha \Delta p^{\beta} \tag{4.55}$$

or

$$q = \alpha' W \Delta p^{\beta} \tag{4.56}$$

where α, α' and β are coefficients assumed to be constants for a certain opening and dependent solely on the geometry of the opening. W is the width of the opening. The difference between α and α' is that the latter is the value per unit width ($\alpha = \alpha' W$).

The value of β depends on both the geometry and Re. Thus, for a given opening, the value of β changes with the volume flow rate. However, the greatest variation of β occurs at lower pressures and the value can be constant in a very wide range at high pressures. A precise definition for those ranges does not exist.

4.6.2 Curve Fitting to Measurement Data Points

The results of a leakage flow measurements will be comprised of a set of pairs of values of pressure difference Δp and leakage flow rate Q. This data can be refined

into a curve that can be used to estimate leakage flow rate at a specified Δp or as an input to a mathematical model to calculate ventilation rates.

Ideally, an equation that has the best fit to series of data points should satisfy who requirements. First, the flow characteristic should be described closely over the range of Δp used for experimental measurements. In addition, extrapolation should be reliable at lower pressures normally occurred in ventilation.

For the power law (equation 4.55) it is possible to transform it to a linear equation for $\ln q$ and $\ln \Delta p$, so that

$$\ln q = \beta \ln \Delta p + \ln \alpha \tag{4.57}$$

Now a standard linear regression analysis can be achieved [9], with β and $\ln \alpha$ being the coefficients of the equation.

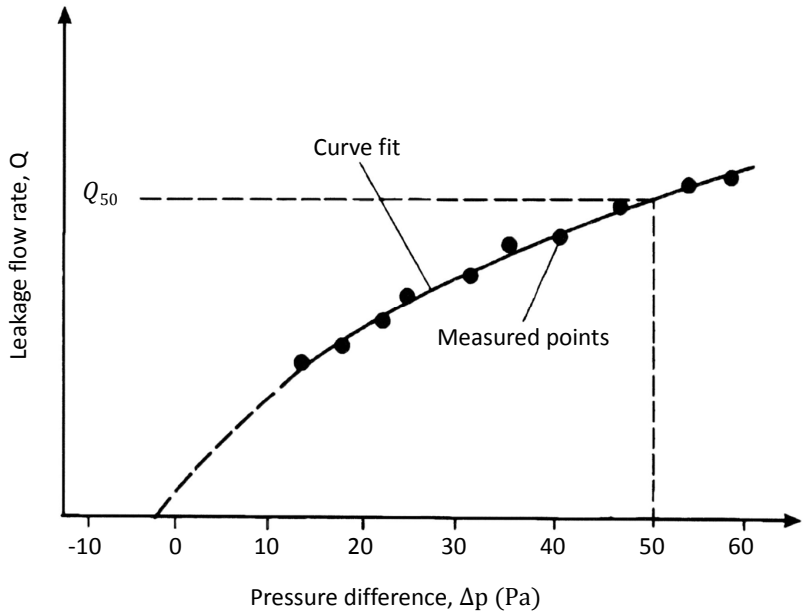

Figure 4.7 *Leakage flow rate estimation at a given pressure difference [9].*

4.6.3 Combination of Parallel Openings

When steady flow characteristic of each individual opening of a combination is known, the flow characteristic of the combination can easily be found. In parallel combination, the pressure difference across each opening is equal. Assuming that the openings do not significantly interfere with each other, the flow characteristic of the combination is given by

$$\Delta p_1 = \Delta p_2 = \Delta p_3 = p_{01} - p_{02} = \Delta p_{tot} \tag{4.58}$$

and

$$Q_{tot} = q_1 + q_2 + q_3 \tag{4.59}$$

where Q_{tot} is the total flow rate of the combination.

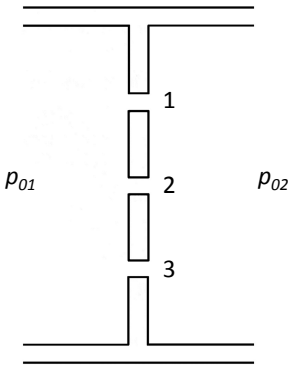

Figure 4.8 *Example of openings in parallel. [9].*

Etheridge [9] has found this procedure to be a viable approach to problems such as a door with a leakage flow path consisting two or more different cross-sectional areas.

5. FLOW SIMULATION

This chapter explains how the CFD calculation was performed for two cross sections, which are also experimentally investigated in this thesis. The calculation was performed with ANSYS® Fluent®, a commercial CFD simulation software.

Flow simulation was performed on two different labyrinth geometry, vertical labyrinths (assembly no. 3) and a modified sill labyrinth (assembly no. 6, modified). The selection was made based on the fact that the lintel and the vertical labyrinth are very similar to each other. Thus, ignoring the discontinuities of the labyrinth sealing (i.e. the corners and the upper and lower middle sections), the flow area of the elevator door is mainly composed of these two cross-sectional geometries, and the modelling of turbulence in these two gaps provides relatively a lot of information with reasonable amount of work on the question of which turbulence model would be best suited for modelling the entire leakage flow of the door. Only the simulation of the sill labyrinth is presented in this chapter, because the upright labyrinth was treated in a similar manner.

The geometry of discontinuities, such as the corners, should be modelled in three dimensions, which increases the resources needed both temporally and computationally, and is not performed in this thesis. However, the leakage rate through these discontinuities are around one third of the entire leakage of the door, when the dimensions of the door are $LL = 1100$ mm and $HH = 2100$ mm, based on experiments done in this work. Thus, when using an appropriate turbulence model, a bold assumption can be made that the same model will perform satisfyingly in three-dimensional simulation of discontinuities as well, if such an analysis is to be done at all.

5.1 Geometry

The 2D models used in CFD simulations were modelled based on the 3D CAD model, which was received from KONE. These geometries were modelled using ANSYS® DesignModeler™, which is a basic tool on the ANSYS® Workbench™ platform. Figure 5.1 shows the domain of the sill labyrinth used in the simulation. The outlet

boundary was set sufficiently far downstream to achieve better convergence.

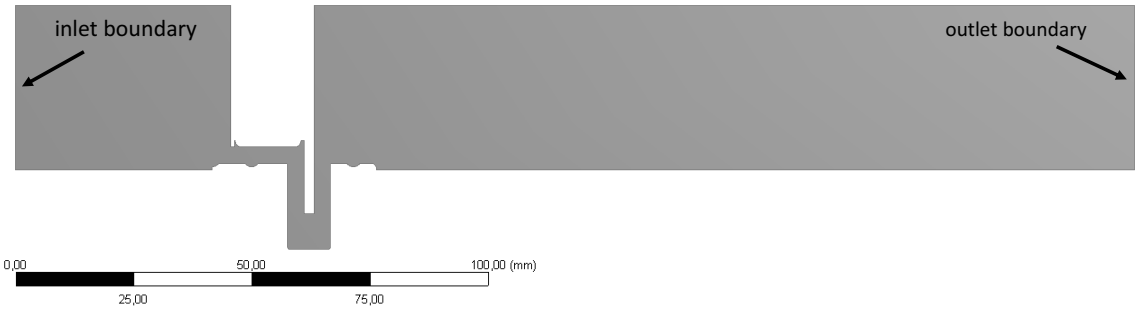

Figure 5.1 *The domain of modified sill labyrinth used in CFD simulations.*

5.2 Meshing

The meshes was generated using ANSYS Workbench and refined at the gap so that the turbulence could be modelled with the appropriate accuracy. Finally, the inflation tool was used to increased the layer resolution near the walls in the normal direction of the wall. In the case of scalable wall functions, however, the inflation was omitted. The mesh generated for the sill labyrinth, including 33,000 elements, is shown in Figure 5.2.

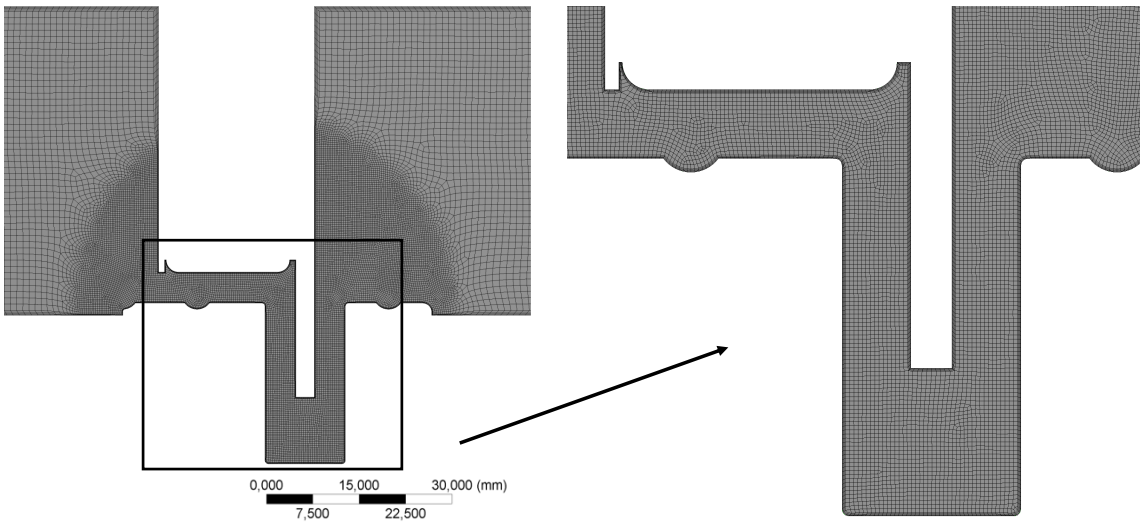

Figure 5.2 *Mesh used in the simulation of sill labyrinth.*

5.2.1 Mesh Independence

In order to produce the best possible results in a simulation, the mesh must be sufficiently fine. For this reason, the so-called mesh independence is considered.

This means that the mesh is moderately refined, step by step, and the change that it causes to one of the variables is considered.

In this work, the mesh independence was determined by examining the velocity profile at the narrowest cross section of the labyrinth sealing and refining the mesh gradually until the shape of the velocity profile has not changed significantly and the pressure difference over the gap remained unchanged. This method was used in both simulated cases. For example, in the case of Figure 5.2, 15 cells from wall to wall were the first trial, after which the number was increased by two, and further by two. Naturally, the rest of the mesh is refined in the same proportion. Neither the velocity profile nor the pressure difference were not changed significantly with the second time of refinement, so the selected number of cells over the gap was 17.

5.2.2 Mesh Quality

Attention was paid to the quality of the computing network, especially in the gap, because it is actually the subject of interest due to the walls. There is the decisive turbulence region that results in a pressure drop.

Y-plus values do not really tell the quality of the mesh, but show that the wall-adjacent cells are small enough to allow the boundary layer to be solved all the way to the wall through the laminar sublayer. Y-plus values are rather a requirement than a guarantee of success in a simulation.

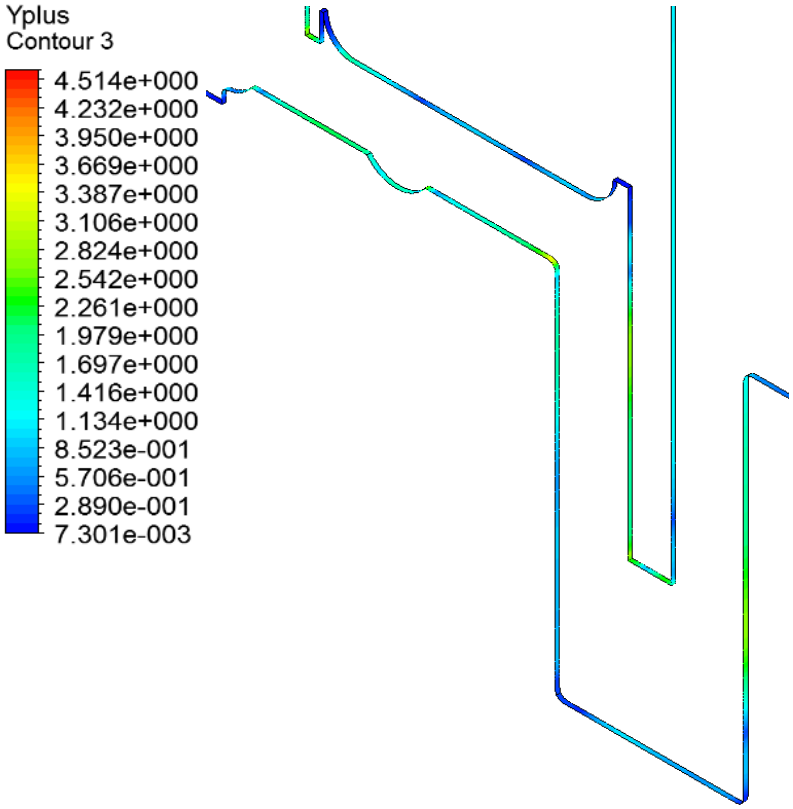

Figure 5.3 *Y-plus values at the narrowest point of the gap, $\Delta p = 290$ Pa, in simulation of the modified sill labyrinth, using realisable k-ε model and enhanced wall functions.*

5.3 Simulation Setup

In this work, the flow is assumed to be incompressible. This can confidently be done because in all cases, Mach number clearly is M $<$ 0.3. The air temperature was set to 20 degrees Celsius and the density to 1.2 kg/m^3.

Turbulence models used in the simulations are widely used two equation models, which are expected to yield good results without unreasonable computational resources. The models used in the simulations are the standard k-ε, realisable k-ε model, and SST k-ω model.

Concerning wall treatment, both enhanced wall functions as well as scalable wall functions were employed for k-ε models, whereas for the k-ω model, the low-Reynolds number correction was used.

A second-order upwind scheme was chosen for the numerical discretization method, since convergence did not really cause any problems to accomplish, as long as the outlet boundary was set sufficiently far downstream.

5.3.1 Boundary Conditions

In all cases, constant velocity was used as an inlet boundary condition. Thus, the procedure differs from experimental measurements, whereby the pressure difference was desired, whereas the volume flow rate was measured.

However, the velocity criterion excludes solutions in which the flow does not pass through the labyrinth gap, but enters from the inlet boundary and leaves the domain through the same boundary. The same is also the case with the outlet boundary, and in practice, a solution that satisfies the boundary conditions is a vortex at each end of the domain.

At the outlet boundary, constant pressure of 100 kPa was applied to the boundary condition. The velocity criterion was set case by case, so that each variation of turbulence model and wall treatment method was subjected to six simulations. Based on these simulation results, best-fit curves were drawn. The comparison is performed in Chapter 7. The boundary conditions are listed in detail in Table 5.1

Table 5.1 *Boundary conditions.*

Boundary	Boundary Condition	Value
Inlet	Velocity Inlet	Constant, case-by-case
	Turbulent Intensity	5,0 %
	Hydraulic Diameter	0,4 m
Outlet	Pressure Outlet	100 000 Pa
Walls	No-slip	N/A

5.3.2 Convergence

In general, problems in CFD simulation are nonlinear and numerical methods are exploited by the solvers, that is, an iterative process is used to reach a solution. Thus, it is self-selectable when the solution is sufficiently accurate and the process is terminated. This is called convergence. However, determining the criteria for convergence is a compromise between the resources used and the desired precision. Excessively demanding convergence criteria often leads to long computing time without any practical gain.

In this work, the convergence took about 10 minutes at its peak when the calculation was executed with an Intel Core i5-3570K processor (overclocked up to 4.5 GHz).

Therefore, there was no need to compromise on the convergence criteria. In Table 5.2, the convergence criteria are listed.

Finally, it was rechecked that the conservation of mass was maintained.

Table 5.2 *Convergence criteria.*

Variable	Convergence Criterion
x-velocity, u	10^{-6}
y-velocity, v	10^{-6}
Continuity	10^{-6}
Turbulence kinetic energy, k	10^{-6}
Rate of dissipation, ε	10^{-6}
Specific dissipation, ω	10^{-6}

6. EXPERIMENTAL WORK

Handling and measuring the whole landing door is inconvenient and requires a lot of space and resources. Secondly, identifying the most harmful noise sources can be difficult. On the other hand, when measuring the whole door, there is no need to be involved with the uncertainty caused by the model. Here the model refers, for example, to a portion of the labyrinth seal that is cut from the door and measured independently.

In this work, the landing door was decided to split into smaller configurations for the experiments. These configurations were chosen so that all possible sources of noise would be mapped and at the same time it would be possible to calculate the entire leakage volume of the door based on the measurements of these subassemblies.

The experimental apparatus aimed at creating an adjustable pressure difference across the labyrinth seals to be measured. The requirement was to simultaneously measure the pressure difference and the noise. On the other hand, the connection between the Δp and the flow rate had to be measured. The experiment was carried out in such a way that the pressure difference, noise and volume flow were measured simultaneously. An additional requirement was that generating a pressure difference should not produce significant noise that interferes with the noise measurements.

The test equipment was designed to blow a suitable overpressure into a pressure chamber constructed from MDF, thickness of 8 mm. On the top of the chamber, there was a place for the labyrinth seal assembly. The labyrinths were constructed so that those could be turned upside down, and so the flow direction through the seal could be turned over. The idea of this is shown in Figure 6.1.

The experimental part of this work were performed in an acoustic room at the premises of KONE Corporation in Hyvinkää. To reduce noise in the acoustic room, the fan with its motor as well as the orifice flow meter was placed outside the room. The air was run with a hose through the wall into the pressure chamber.

Some difficulties were also encountered. The most significant problem was the volume flow adjustment. At low volume flows, the system was sometimes difficult to

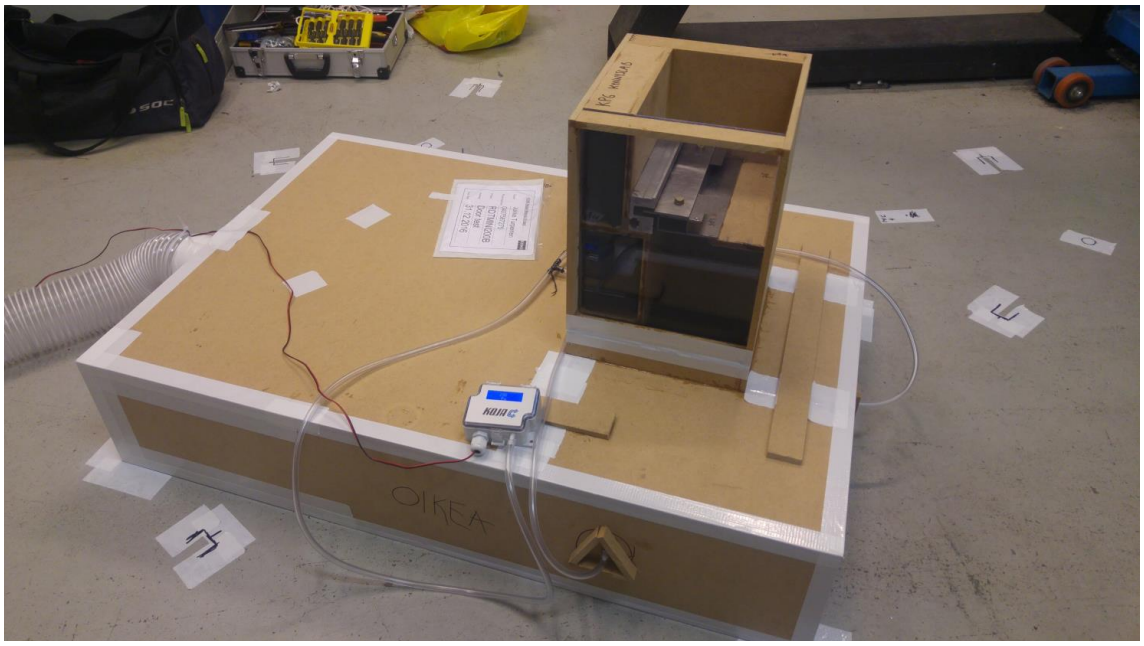

Figure 6.1 *Test equipment in the acoustic room.*

get stable and, on the other hand, large volumetric flows could cause the fan output to end in some configurations.

6.1 Noise Measurement

The measurement of noise in this work is based on ISO 3746-1979. Although there were four measuring points in the microphone configuration, only one noise meter was used and recirculated at every microphone position in turn. Measurements were performed by keeping the pressure difference constant while measuring the noise alternately at each microphone position. Thereafter, the pressure difference was increased and noise was again measured at each point.

The noise meter used in the measurements was Brüel & Kjær hand-held analyzer type 2250 Light with microphone type 4189, attached to the tripod.

The radius of the hemispherical measurement surface was chosen to be $r = 1$ m (see Figure 3.3). Origin was placed in the middle of the configuration to be measured, so that the z-axis zero point is on the top surface of the pressure chamber.

The microphone positions (angle of rotation) were selected according to the most loudest subassembly (assembly 6) and the differential pressure (160 Pa). The loudest angle was searched and the measuring point was set. The other places were determined according to this angle as defined in the standard. These microphone

positions were used throughout the measurements for all subassemblies.

A measurement time of 10 seconds (length of the time period T) was used and the background noise measured in the period of 10 seconds was equivalent to sound pressure level of $L_{Aeq,10s} = 25.0$ dBA. The mean acoustic absorption coefficient of the test room was assumed to be $\alpha = 0.5$, indicating that the reverberation in the room was very low (see Table 3.7).

6.2 Flow Rate Measurement

The measurement of air flow rate in this work is based on standard ISO 5167-1980. The measurement is based on an orifice in the pipe that forms a pressure drop in the flow. This pressure loss is proportional to the volume flow which can then be calculated.

Atmospheric pressure and humidity were also measured for determining the material properties of air. For this purpose, Vaisala PTB110 barometer was used. The pressure difference across the orifice plate was measured with the HK Instruments DPT2500-R8 differential pressure transmitter. The same transmitter model was also used to measure pressure difference across the labyrinths.

Because of the great amount of measurement data, a MATLAB program was created to process the data. This is shown in Annex A.

6.3 Measuring Pressure Difference

The pressure difference across the labyrinth seal assembly was measured so that the pressure chamber's walls had three measuring points that were imported to the pressure differential transmitter. The second measuring member of the pressure gauge was exposed to ambient pressure in the acoustic room. The pressure difference was measured by HK Instruments DPT2500-R8.

6.4 Test Assemblies

Subassemblies were constructed from seven different portions of the door, these sections are shown in Figure 6.2.

The following were requested from the subassemblies:

1. All different cross-sections shall be considered to find out the most significant noise sources.

2. The volume flow rate of the whole door can be approximated from the measurement results.

Both upper and lower corners are symmetrical in the door. Some examples of the structure of the tested subassemblies are shown in Figure 6.3. In addition, the subassemblies containing the sill labyrinth (assemblies 5, 6 and 7) were constructed two-fold with the difference that the alternative geometry was modified by blocking the holes shown in Figure 6.4.

As a foreknowledge for the work it was that the door produced, in certain circumstances, disturbing whistle. When the structure of the door was examined more closely, the idea was that the holes beside flow path of the sill labyrinth could form a noise-inducing structure. The modification refers to the blocking of these holes in all subassemblies in which they occur, i.e. as mentioned above, in subassemblies 5, 6 and 7.

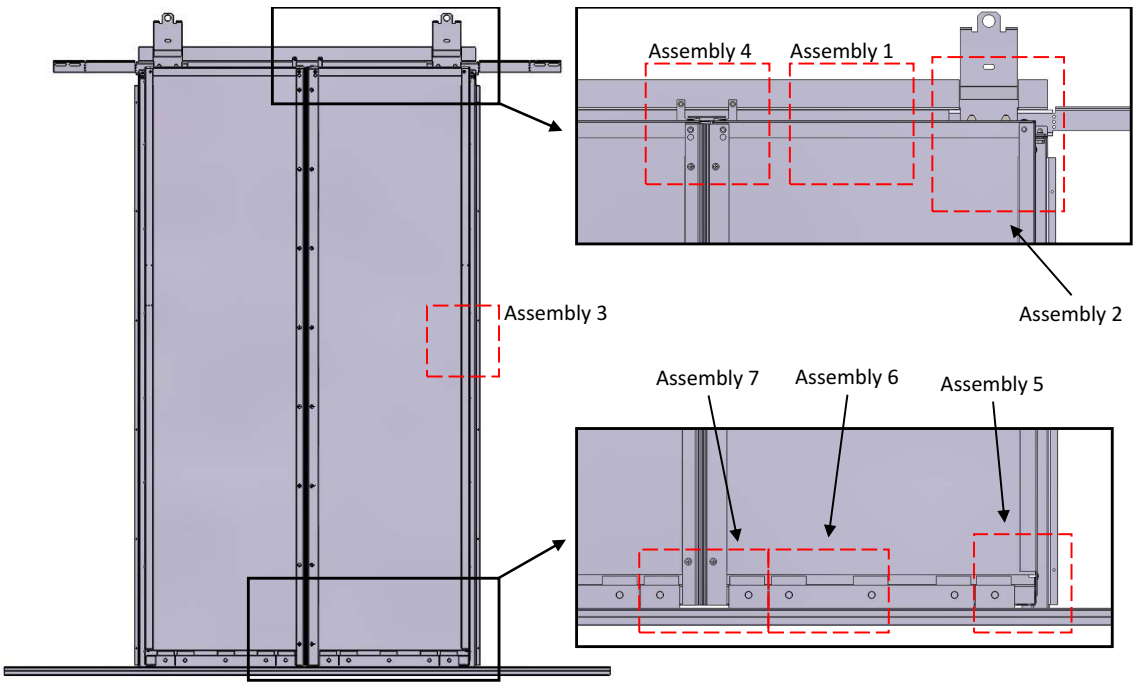

Figure 6.2 *Cuts from which the subassemblies were built for measurements.*

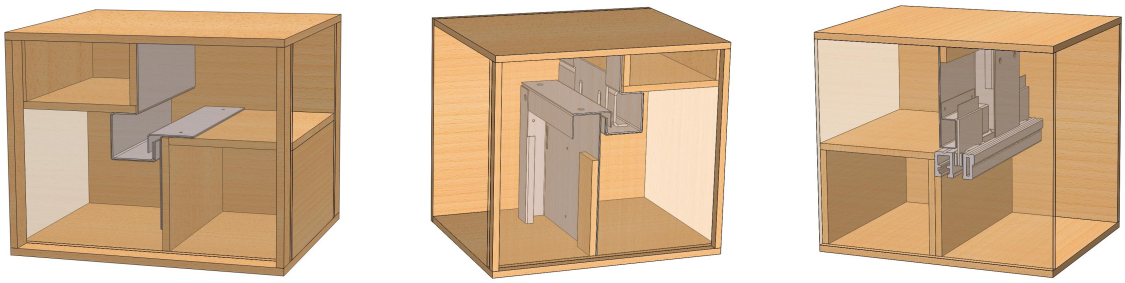

Figure 6.3 *Couple examples of test assemblies (CAD models). The walls facing the reader are set to transparent for clarity.*

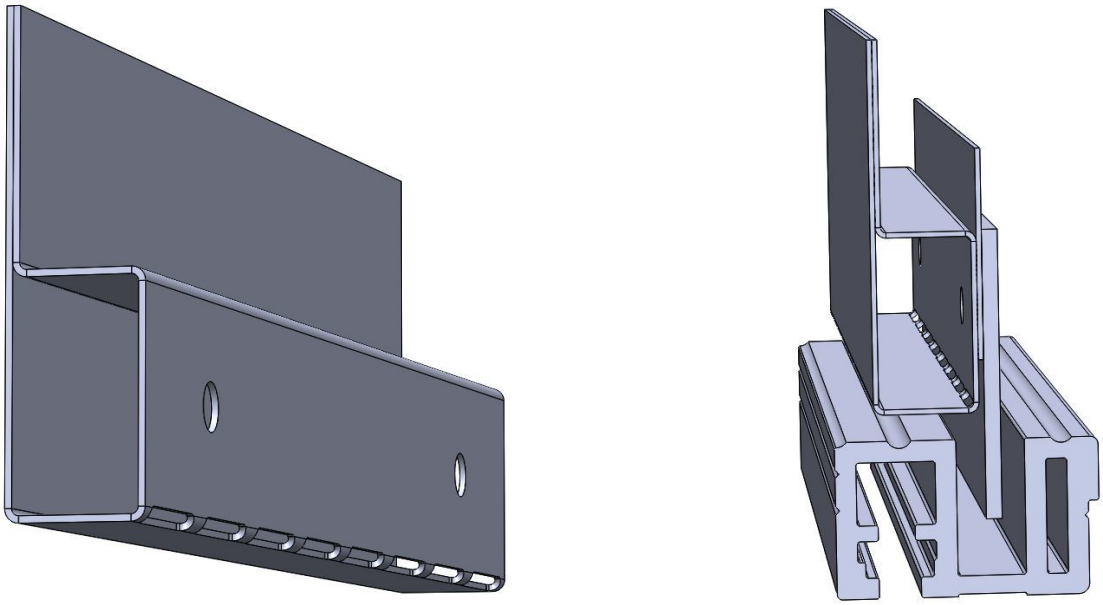

Figure 6.4 *An unmodified profile of the sill labyrinth on the left, and its position in the labyrinth on the right. In the modified versions, the holes in the bottom corner of the horizontal profile were blocked.*

7. RESULTS

In this chapter the results of the work are presented. First, the results of the leakage flow of the subassemblies and the whole door are introduced in both flow directions. Regarding the results presented, the pressure difference across the landing door is always shown as a positive value and the flow direction is indicated separately. The term *Direction 1* refers to the direction of flow from the lobby to the elevator shaft, while *Direction 2* is vice versa.

All results related to volume flow rate should be interpreted with caution when using measurement data extrapolated up to very small pressure differences, such as more specifically explained in Section 4.6.

Secondly, the results of the noise measurement are presented and the modified geometry is compared to the original. Finally, the results of turbulence models are compared.

7.1 Volume Flow Rate

Figure 7.1 presents the measurement results of volume flow rate of assemblies 1, 2, 3 and 4, and the best-fit lines based on *the power law*.

Using the measurement data shown in Figures 7.1 and 7.2, an estimate of the flow rate of the entire door can be derived in either direction of flow. The variables are the pressure difference Δp and the door dimensions LL and HH. The flow rate is obtained by

$$Q_{tot} = \overbrace{(LL-a)\,\alpha_1'\Delta p^{\beta_1}}^{\text{Lintel labyrinth}} + \overbrace{2\,(HH-b)\,\alpha_3'\Delta p^{\beta_3}}^{\text{Upright labyrinths}} + \overbrace{(LL-c)\,\alpha_6'\Delta p^{\beta_6}}^{\text{Sill labyrinth}} + \\ + \underbrace{2\alpha_2\Delta p^{\beta_2}}_{\text{Upper corners}} + \underbrace{\alpha_4\Delta p^{\beta_4}}_{\text{Upper middle section}} + \underbrace{2\alpha_5\Delta p^{\beta_5}}_{\text{Lower corners}} + \underbrace{\alpha_7\Delta p^{\beta_7}}_{\text{Lower middle section}} \tag{7.1}$$

of which values of constants and coefficients are listed in Table 7.1. Parameters LL and HH refer to clear opening width and height of the entrance, respectively.

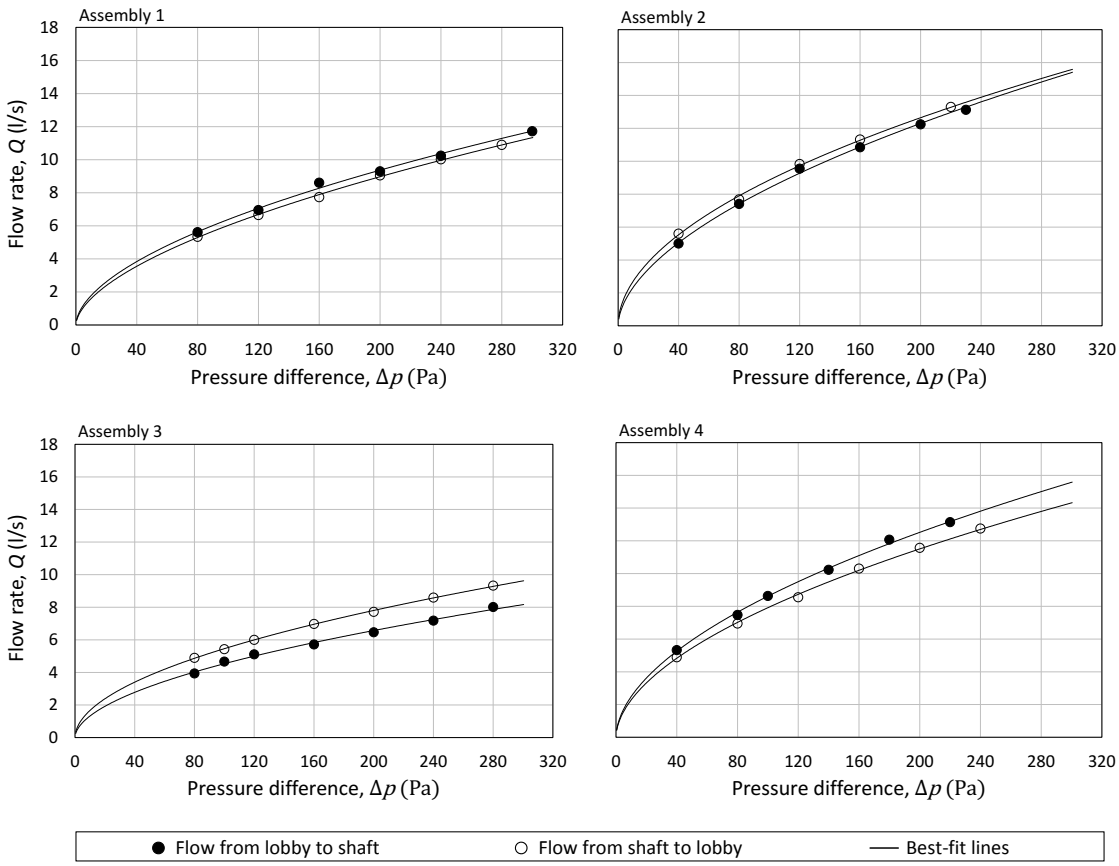

Figure 7.1 *Measured flow rate curves of assemblies 1, 2, 3, and 4.*

Constants a, b and c are due to geometric overlap and are formed such that, for example, the width of the door LL is reduced by the width of the corners and middle section. Thus, for example, the factor (LL - a) represents length of the lintel in which the cross-section is invariable and separated by overlapping with other measured subassemblies. In other words, the first three terms of equation 7.1 depend on the height and width of the door, while the other terms are independent of the door dimensions.

In Figure 7.2, volume flow rates of the assemblies 5, 6 and 7 are presented, as well as the corresponding results of the modified versions. Assembly 6 was tested first, after which a smaller number of measuring points were found to be sufficient. For this reason, the number of measuring points in other cases is smaller. Figure 7.3 shows the comparison of estimated flow rates of entire door obtained by equation 7.1.

Actually, all measuring points fit well into the power law curve so it can be said that the random errors were fairly well avoided.

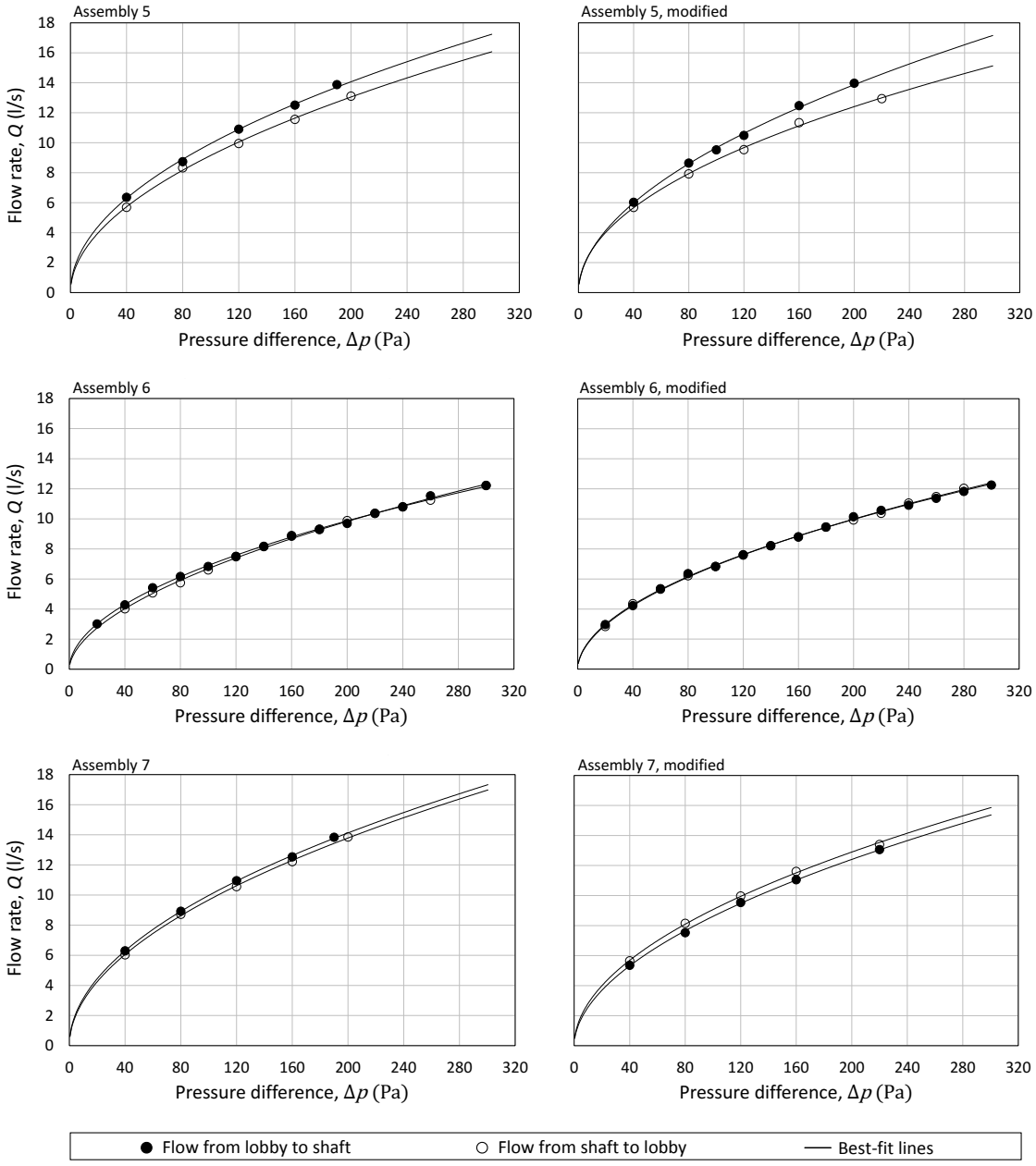

Figure 7.2 *Measured flow rate curves of assemblies 5, 6, 7, and their modified versions.*

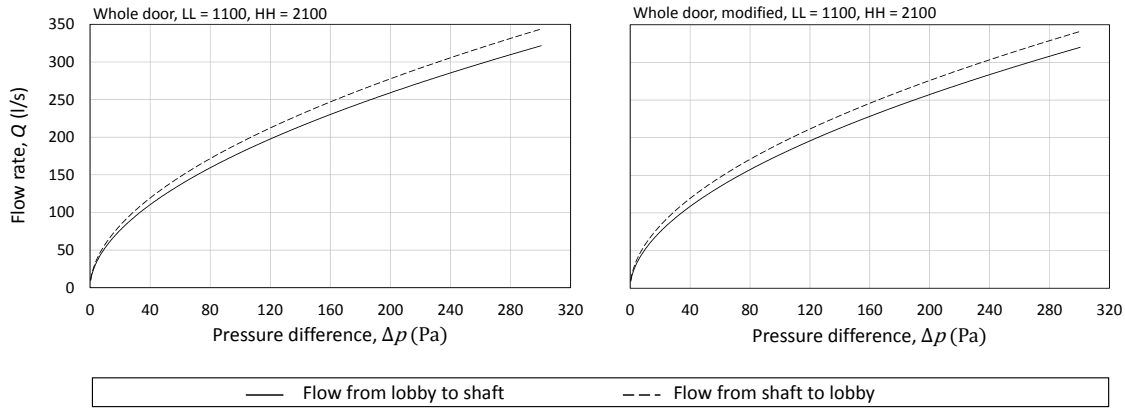

Figure 7.3 *Comparison of estimated flow rate curves between the original whole door (LL = 1100 mm, HH = 2100 mm) and the modified version, obtained by equation 7.1.*

Table 7.1 *Values of coefficients α, α' and β derived from the measurement data.*

Assembly tested	Flow direction					
	From lobby to shaft (Direction 1)			From shaft to lobby (Direction 2)		
	Coefficient, α [(l/s) Pa$^{-\beta}$]	Coefficient, α' [(l/s) Pa$^{-\beta}$ m^{-1}]	Exponent, β	Coefficient, α [(l/s) Pa$^{-\beta}$]	Coefficient, α' [(l/s) Pa$^{-\beta}$ m^{-1}]	Exponent, β
No. 1	0.496	2.478	0.555	0.424	2.120	0.576
No. 2	0.656	N/A	0.553	0.833	N/A	0.513
No. 3	0.387	1.933	0.535	0.508	2.541	0.516
No. 4	0.720	N/A	0.540	0.660	N/A	0.540
No. 5	0.994	N/A	0.500	0.866	N/A	0.512
No. 5, modified	0.873	N/A	0.522	0.940	N/A	0.487
No. 6	0.643	3.213	0.516	0.519	2.596	0.555
No. 6, modified	0.618	3.091	0.525	0.589	2.946	0.534
No. 7	0.987	N/A	0.502	0.917	N/A	0.512
No. 7, modified	0.763	N/A	0.527	0.872	N/A	0.509
Constants	a = 0.5 m	b = 0.27 m	c = 0.387 m			

7.2 Noise

Figure 7.4 shows the surface SPLs of assemblies 1, 2, 3 and 4. With regard to assemblies 1 and 3, there can be seen peaks around 100 Pa and correspondingly in the case of assembly 2 at 220 Pa. All these peaks occur in the same flow direction, where air flows from the lobby to the elevator shaft. The peak of assembly 1 is clearly the strongest.

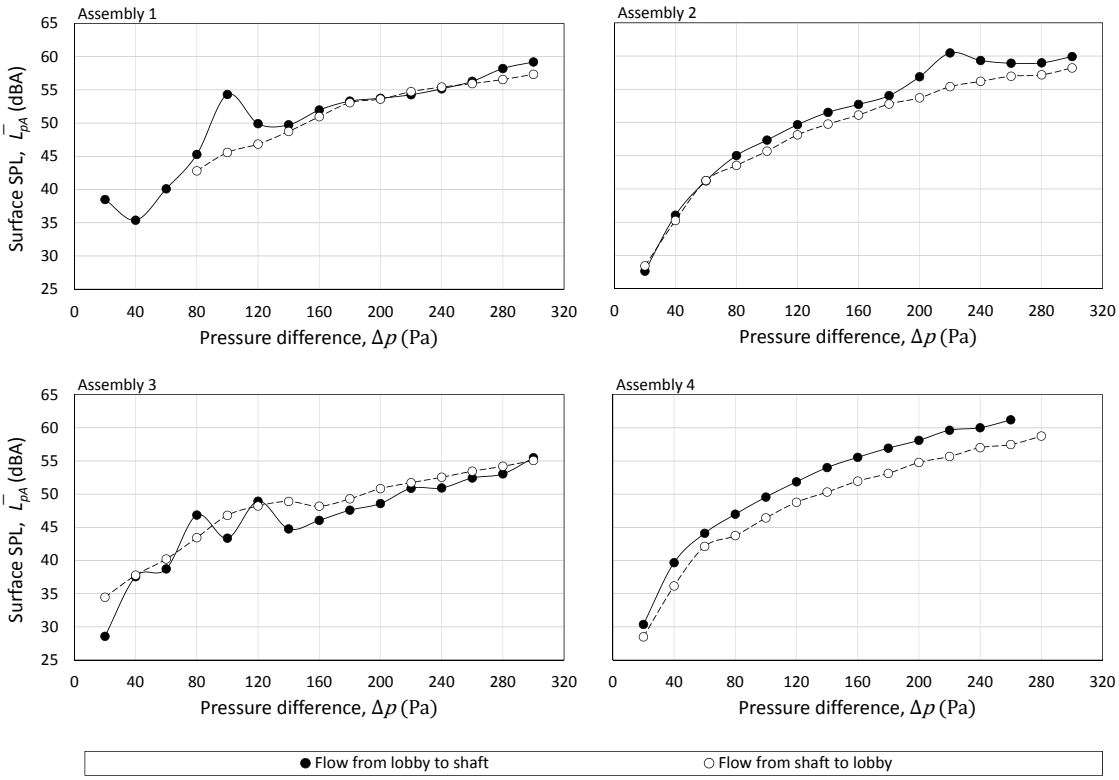

Figure 7.4 *Measured surface SPLs of assemblies 1, 2, 3, and 4.*

In Figure 7.5, the surface SPLs of assemblies 5, 6 and 7 as well as the results of the corresponding modified assemblies. Speaking of these, really only in assembly 6 there are peaks, though they are in a very wide range of pressure difference.

The actual comparison between the original and the modified configurations is shown in Figure 7.6. In the original assembly number 6, there is a huge peak in relation to the modified, with the difference being at best 15 dBA at pressure difference of 160 Pa when the flow direction is from lobby to shaft. This is also shown in Figure 7.8, which shows the modification-induced change in the sound spectrum with certain pressure differences. When the flow direction is opposite, the peak occurs at 120 Pa and is somewhat smaller in size, about 10 dBA.

Figure 7.7 shows how much effect the elimination of these aforementioned peaks may have on the sound power level of the entire door. Both directions are viewed separately. Graphs may seem somewhat inadequate in terms of how they cover the pressure difference between 0-300 Pa because the calculation of the total SWL of the door with a given pressure difference requires successful measurement results for all subassemblies with that differential pressure in question. Due to the adjustment problems in the measurements, the results are simply insufficient to estimate the SWL with a greater Δp range than the one in Figure 7.7.

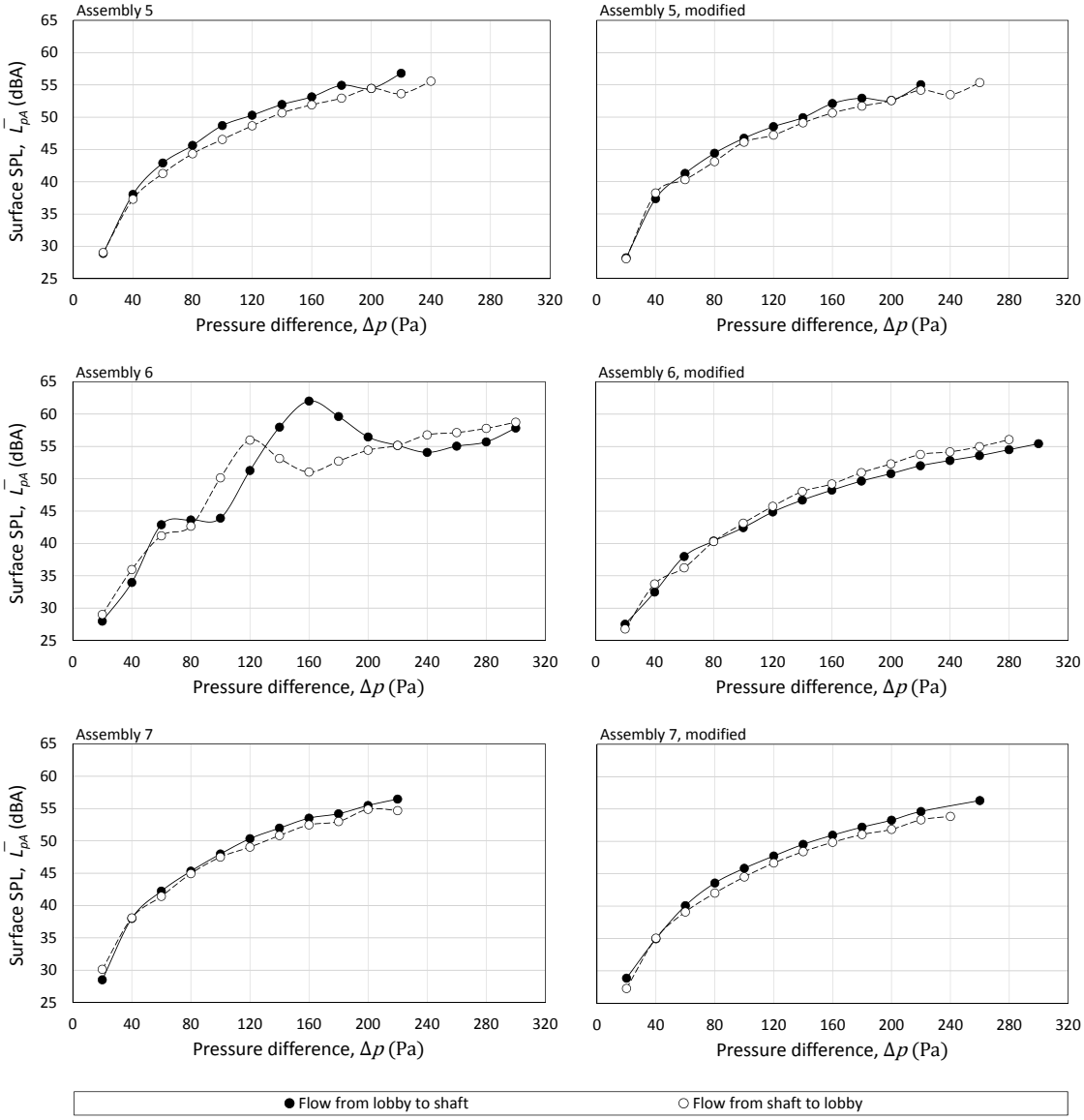

Figure 7.5 *Measured surface SPLs of assemblies 5, 6, 7, and their modified versions.*

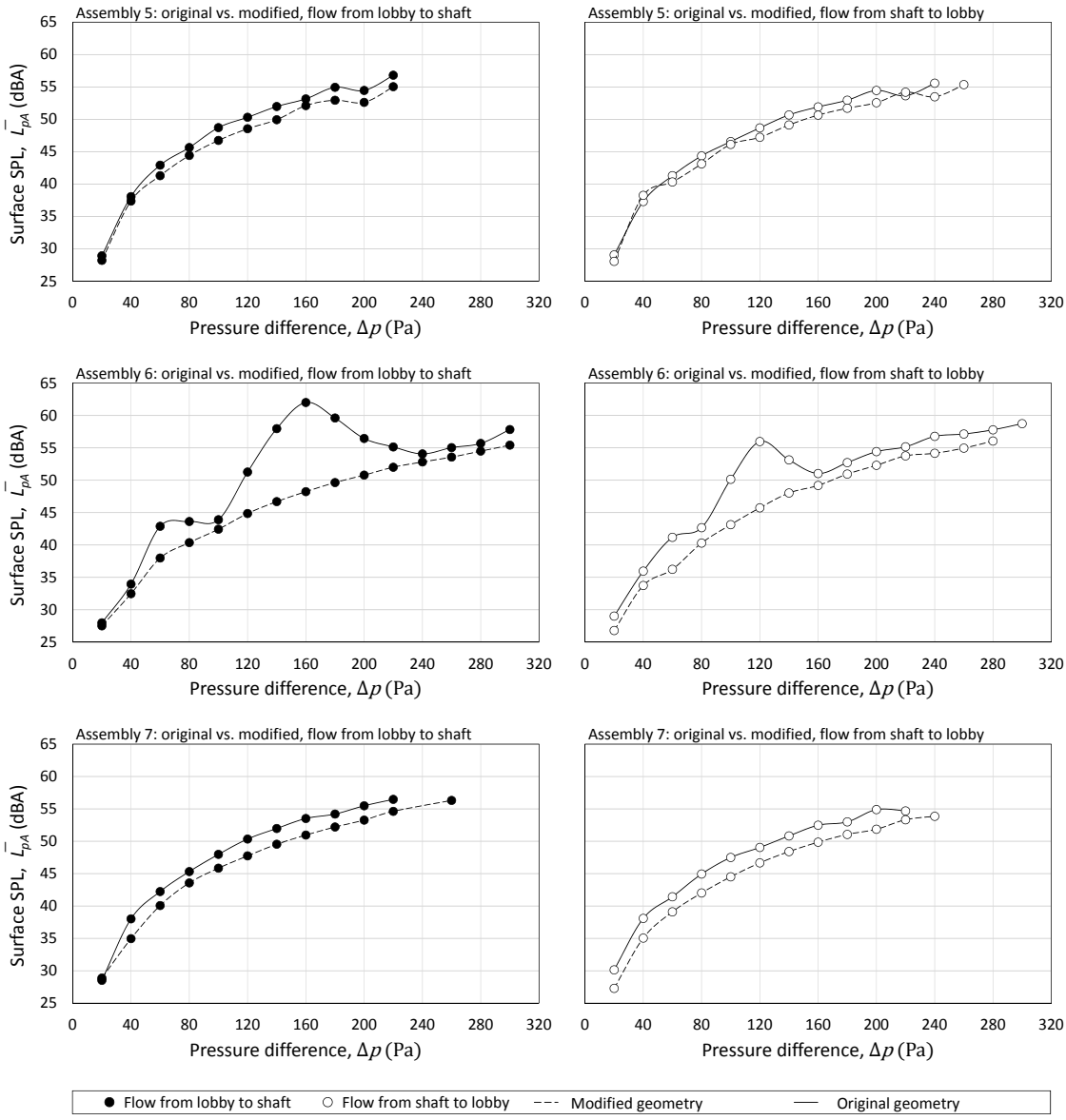

Figure 7.6 *Comparison between measured surface SPLs of assemblies 5, 6, 7, and their modified versions.*

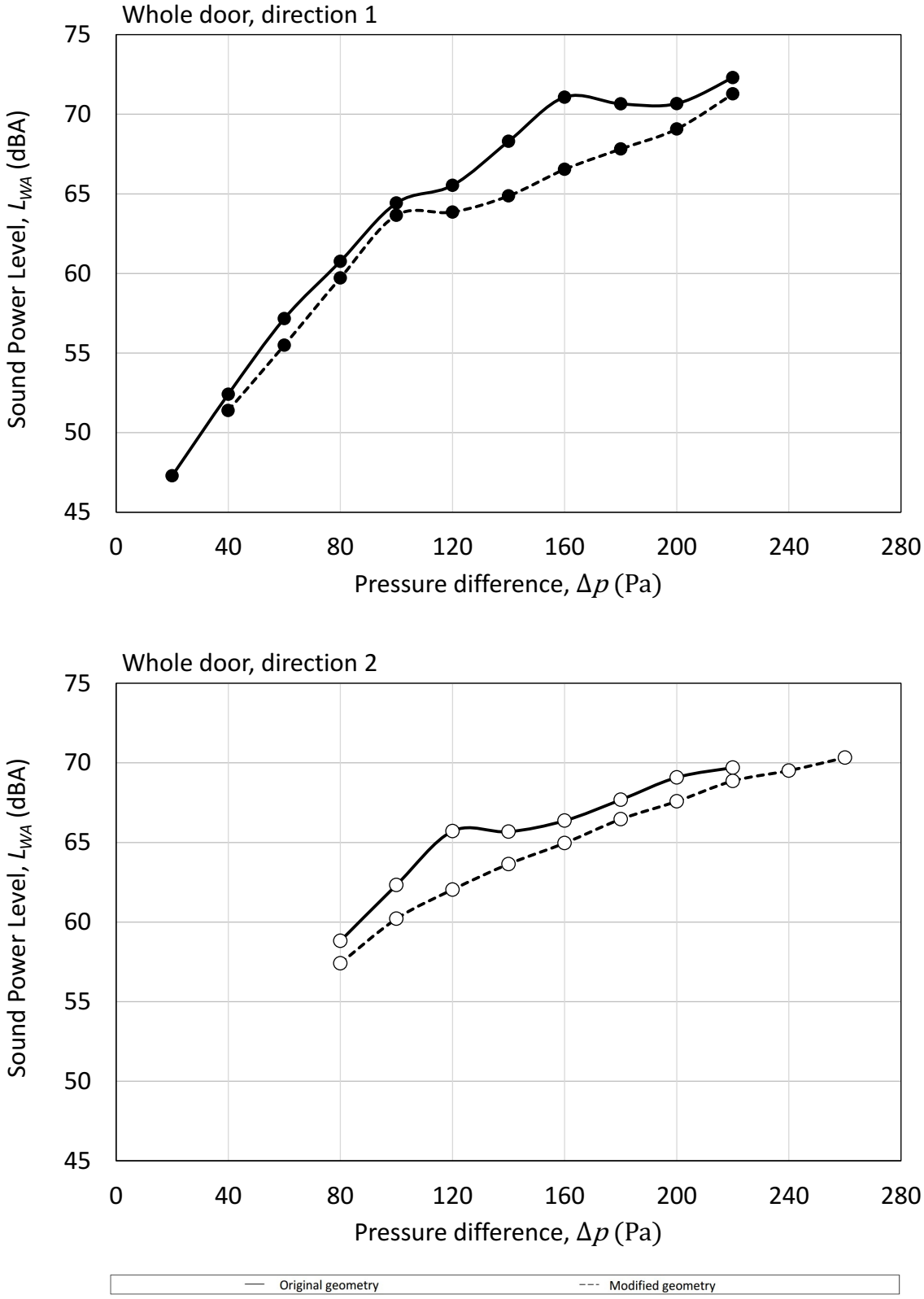

Figure 7.7 *Comparison of estimated sound power levels between original and modified full-size door (LL = 1100 mm, HH = 2100 mm).*

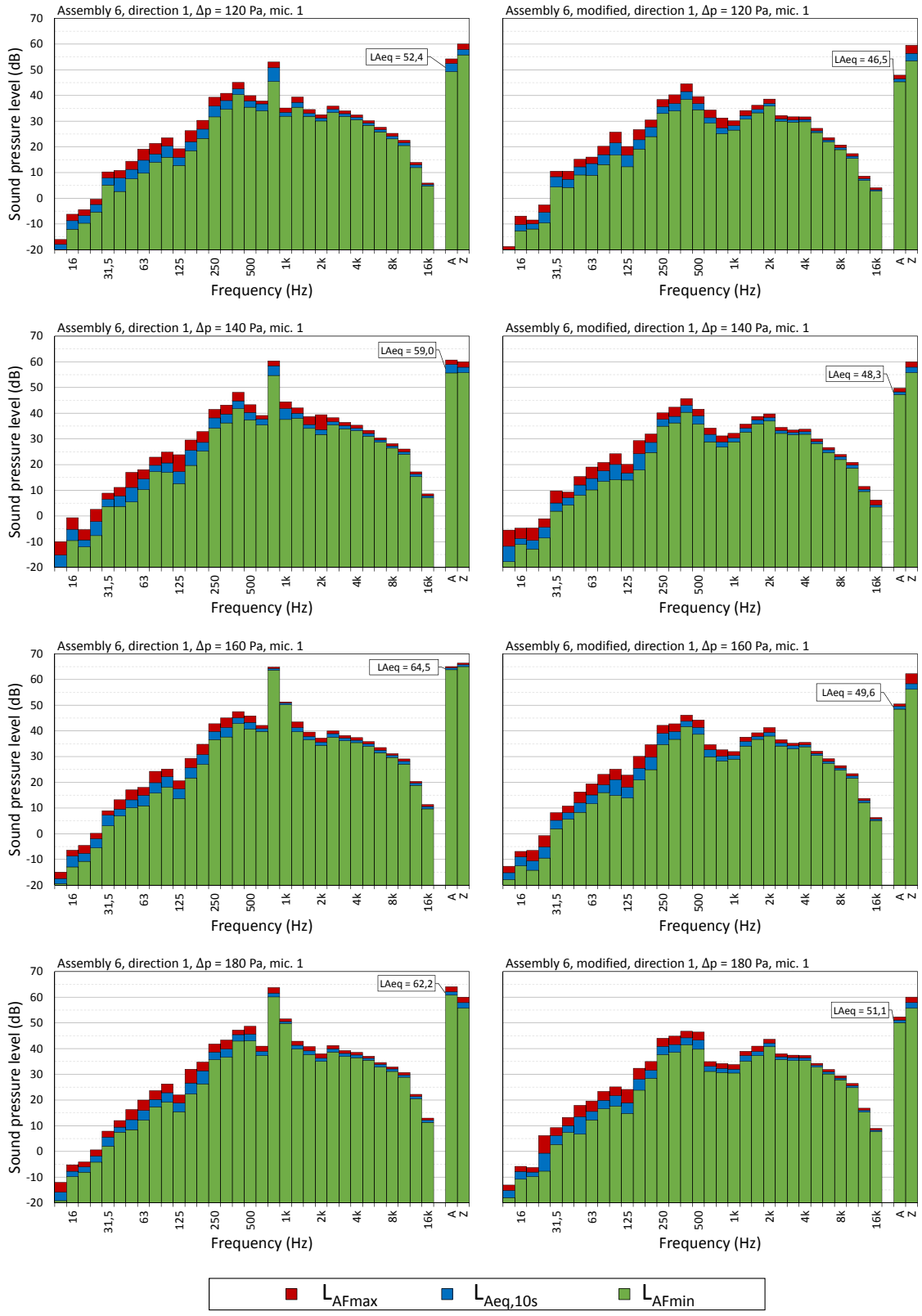

Figure 7.8 *Comparison of measured 1/3-octave bands of the sill labyrinth (assembly 6) and the modified version with pressure differences 120, 140, 160, and 180 Pa. Tonal peak can be seen at the frequency band of 800 Hz.*

7.3 Comparison of Turbulence Models

Figures 7.9 and 7.10 are exemplary representations of the velocity and pressure fields of both the sill and upright labyrinth seals obtained from the CFD simulation.

In Figure 7.9, the flow enters to labyrinth gap from the left and correspondingly, in Figure 7.10, the flow enters from down. The velocity fields show how the flow separates from the wall at sharp edges in a curvy labyrinth. The maximum velocity with a pressure difference of 285 pascals is 19.6 m/s in modified sill labyrinth.

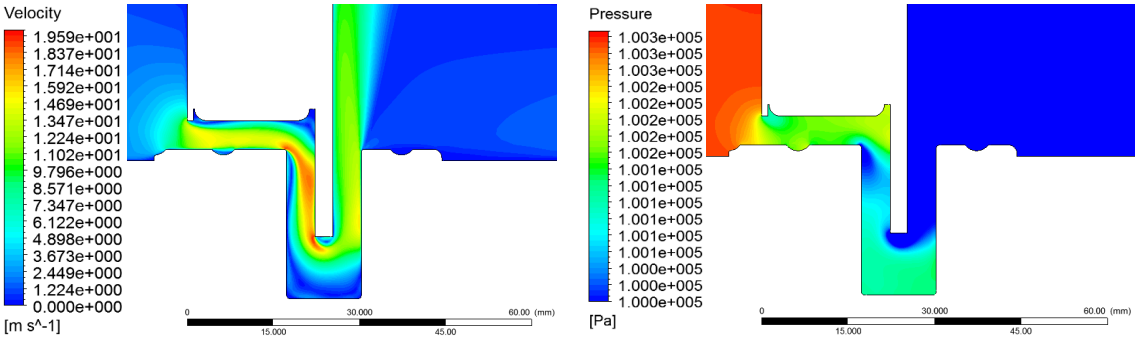

Figure 7.9 *Velocity and pressure fields of modified sill labyrinth at $\Delta p = 285$ Pa. Results obtained with realisable k-ε model, using enhanced wall treatment.*

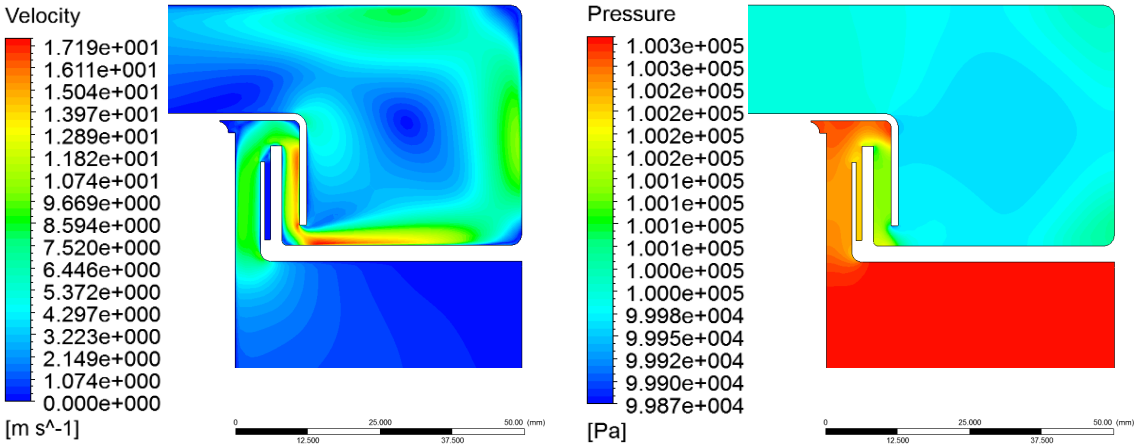

Figure 7.10 *Velocity and pressure fields of upright labyrinth at $\Delta p = 300$ Pa. Results obtained with realisable k-ε model, using enhanced wall treatment.*

The actual comparison of turbulence models is shown in Figure 7.11. The graph show the power law curves matched to the measurement results as well a corresponding curves for all tested turbulence models. For each turbulence model, the relationship between pressure difference and volume flow was calculated at five different points on which best-fit curves were plotted.

Simulation was performed for a vertical labyrinth as well as for a sill labyrinth with no holes, so-called modified geometry.

In either case, the results are quite similar. All turbulence models predicted too low volume flow compared to the measured results. The most successful model is the realisable k-ε model with an error of about 10 % when the scalable wall functions are used as a wall treatment method.

Also, wall treatment methods can be seen to have an effect. Especially in the case of a vertical labyrinth, scalable wall functions would appear giving the best results, although the differences are rather small. In both cases, the error was the highest with SST k-ω model.

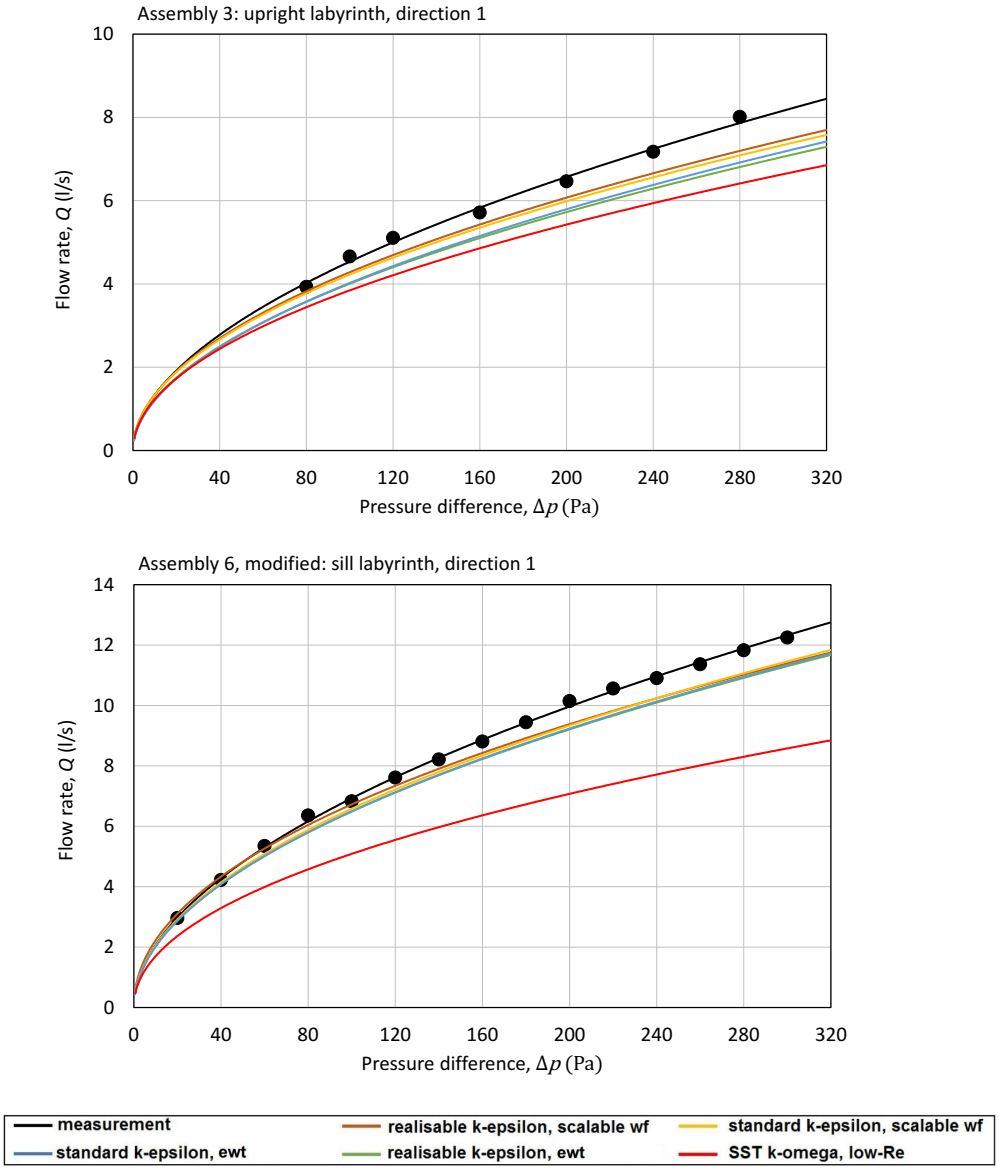

Figure 7.11 *Comparison of turbulence models.*

8. CONCLUSION AND DISCUSSION

The purpose of this work was to investigate the flow-induced noise generated by the labyrinth seals of the elevator landing door and to find solutions to reduce the amount of noise emitted. In addition, the aim was to measure leakage flow rate and to study how suitable is flow simulation as tool for analysing leakage flow rate.

First, KONE Corporation is presented as a company and the theory to understand the stack effect phenomenon is explained. Subsequently, the basic structure and operation of the elevator landing door are described, as well as the theory of noise. The general equations that govern the flow and the turbulence models used in the simulation are presented.

In order to determine the sound sources, the door was not treated as a whole, but smaller configurations were measured to cover all possible noise-inducing structures. At the same time, the leakage flow rate was also measured. Regarding the lower edge of the door, two pieces were constructed to make a change to the original structure. The change to the original structure was to block the holes in the profile of the sill labyrinth. This proved to be an excellent, simple and potential means of significantly reducing the noise generated by the flow. The profile in the sill labyrinth with the holes appears to form a Helmhotz resonator that induces noise in the 800 Hz frequency band according to the 1/3 octave measurements.

The biggest difference in sound pressure levels between the original and the modified subassembly is up to 15 dBA. Blocking the holes seems to have a maximum effect of about 5 dB on the sound power level of the entire door. This may be of great significance in human audition because the noise difference is due to the narrow tonal peak (tonality). Based on the measurements, the modification reduces the noise throughout the pressure difference range. The major differences in noise are perceived in the range of 100-200 Pa.

Perhaps the biggest uncertainty factor with noise measurement is the difference between the model (subassembly) and the actual structure of the sill labyrinth. In the real structure, the profile of the sill is open at the ends, whereas in the measured

models it is closed at the ends (see Figure 6.3). On the other hand, it is known experimentally (as a preliminary information) that the door noise is particularly in the 100-200 Pa range, so the sill labyrinth is reasonably suspected as a source of whistle, since the other subassemblies are not particularly noisy in that area.

Small peaks in the results of subassemblies 1 and 3 may arise from a small gap formed between the sheet metal plates (see Figure 7.10).

The most correct flow rate was predicted by k-ε-based turbulence models. The closest results compared to measurements were achieved with realisable k-ε model and with scalable wall functions, although the differences were small between the different models and wall treatment methods. Hence, flow simulation can be considered a valid tool for examining the fire labyrinths.

BIBLIOGRAPHY

[1] "Tall Buildings in Numbers - The Global Tall Building Picture: Impact of 2016," Council on Tall Buildings and Urban Habitat. Available (accessed on 19.4.2017): http://skyscrapercenter.com/research/CTBUH_ResearchReport_2016YearInReview.pdf

[2] KONE Corporation, KONE in brief, website. Available (accessed on 5.4.2017): http://www.kone.com/en/company

[3] KONE Corporation, Vision and strategy, website. Available (accessed on 5.4.2017): http://www.kone.com/en/company/vision-and-strategy Home > Company > Vision and Strategy

[4] KONE Corporation, KONE enters a new strategic phase: "Winning with Customers", Jan. 2017, Press release. Available (accessed on 5.4.2017): http://www.kone.com/en/media/releases/ Home > Media > Releases

[5] http://www.kone.com/en/stories-and-references/references/ Home > Stories & References > References

[6] KONE Corporation, Kone image bank, website. Available (accessed on 5.4.2017): http://www.kone.com/en/media/ Home > Media > KONE image bank

[7] ASHRAE Handbook, HVAC Applications, SI ed., Chapter 4: Tall Buildings, American Society of Heating, Refrigerating and Air-Conditioning Engineers, Inc., Atlanta, GA, 2011

[8] P. Weismantle, L. Leung, Burj Dubai Stack Effect - Passive Stack Effect Mitigation Measures in the Design of the World's Tallest Building, Council on Tall Buildings and Urban Habitat Journal, Fall 2007, pp. 8-13. Available (accessed on 3.7.2017): http://global.ctbuh.org/resources/papers/download/1234-burj-dubai-stack-effect-passive-stack-effect-mitigation-measures-in-the-design-of-the-worlds-tallest-building.pdf

[9] D. Etheridge, M. Sandberg, Building Ventilation: Theory and Measurement, John Wiley & Sons Ltd, Chichester, England, 1996, 724 p.

[10] ASHRAE Handbook, Fundamentals, SI ed., Chapter 16: Ventilation and Infiltration, American Society of Heating, Refrigerating and Air-Conditioning Engineers, Inc., Atlanta, GA, 2009

[11] U.S. Standard Atmosphere, U.S. Government Printing Office, Washington, D.C., 1976. Available (accessed on 4.7.2017): https://ntrs.nasa.gov/archive/nasa/casi.ntrs.nasa.gov/19770009539.pdf

[12] W. Z. Black, Smoke Movement In Elevator Shafts During A High-Rise Structural Fire, Fire Safety Journal, Vol. 44, No. 2, 2009, pp. 168-182. Available (accessed 4.7.2017): https://www.researchgate.net/publication/223082155_Smoke_movement_in_elevator_shafts_during_a_high-rise_structural_fire

[13] S. Mijorski, S. Cammelli, Stack Effect in High-Rise Buildings: A Review, International Journal of High-Rise Buildings, Vol. 5, No 4, 2016, pp. 327-338. Available (accessed on 4.7.2017): http://global.ctbuh.org/resources/papers/download/3084-stack-effect-in-high-rise-buildings-a-review.pdf

[14] G. T. Tamura, A. G. Wilson, Pressure Differences Caused by Chimney Effect in Three High Buildings, ASHRAE Transactions, Vol. 73, Part 2, 1967, pp. 1-10

[15] A. Raiko, Ride Comfort of Automatic Elevator Doors, MSc thesis, Lappeenranta University of Technology, 2013

[16] KONE AMD Doors and Entrances: Door Configurations. KONE Corporation. Available (accessed 4.7.2017): http://www.movetec-irq.com/admin/files7/AMD

[17] KONE technical1, SO-03.13.047, Product Description: KONE ReNova™ Slim landing doors. Updated 25.04.2013. Available at KONE intranet (access required): http://intranet.konenet.com

[18] H. Anttila, Senior Expert, Elevator Doors Technology Finland, KONE Corporation, P.O. Box 677, FI-05801 Hyvinkää, Finland, Several interviews during the study, 2016

[19] E. Kulo, Evaluating Elevator Landing Door Fire Testing Services, MSc thesis, Lappeenranta University of Technology, 2013. Available (accessed 6.7.2017): http://www.doria.fi/bitstream/handle/10024/92346/final_Dippa_Eetu.pdf?sequence=2

[20] E. Björk, Meluntorjunta, 2nd ed., University of Kuopio, Department of Environmental Sciences, Kuopio University Printing Office, 1995

[21] I. L. Vér, L. L. Beranek, Noise and Vibration Control Engineering: Principles and Applications, 2nd ed., John Wiley & Sons, Inc., Hoboken, New Jersey, 2006, 976 p.

[22] V. Pulkki, M. Karjalainen, Communication acoustics: An Introduction to Speech, Audio, and Psychoacoustics, John Wiley & Sons Ltd, Chichester, United Kingdom, 2015, 457 p.

[23] F. A. Everest, K. C. Pohlmann, Master Handbook of Acoustics, 6th ed., Chapter 2: Sound Levels and the Decibel, McGraw-Hill Education LLC, New York, 2015

[24] G. Ballou, Handbook for Sound Engineers, 4th ed., Part 1: Acoustics, Chapter 2: Fundamentals of Audio and Acoustics, Elsevier Inc., Burlington, USA, 2008, 1808 p.

[25] The Engineering ToolBox, Sound Power – Sound Power Level from Common Sources, Available (accessed 27.7.2017): http://www.engineeringtoolbox.com/sound-power-level-d_58.html

[26] Brüel & Kjær (Sound and Vibration Measurement A/S), Instruction Manual – Hand-held Analyzer Types 2250, 2250-L and 2270, Nærum, Denmark, 2015

[27] M. Karjalainen, Hieman akustiikkaa, Finnish textbook, Espoo: Helsinki University of Technology, Laboratory of Acoustics and Audio Signal Processing, 2000

[28] J. Lee, The Effects of Tones in Noise on Human Annoyance and Performance, University of Nebraska – Lincoln, Architectural Engineering – Dissertations and Student Research, 39, 2016, Available (accessed 4.8.2017): http://digitalcommons.unl.edu/archengdiss/39

[29] International Organization for Standardization, Acoustics – Description, Measurement and Assessment of Environmental Noise – Part 2: Determination of Environmental Noise Levels, ISO 1996-2:2007

[30] H. Nykänen et al., Tuulivoimalan meluvaikutukset: Häiritsevyysmittaristo ja sen käyttö, Research report, VTT Technical Research Centre of Finland Ltd, 2014, Available (accessed 27.7.2017): http://www.vtt.fi/inf/julkaisut/muut/2014/VTT-R-04392-14.pdf

[31] N.Y. ADC. LAW § 27-770: NY Code – Section 27-770: Noise Control of Mechanical Equipment, New York, 2006

[32] Minnesota, Ordinance of Minnesota Chapter 389 – Noise, 2008

[33] International Organization for Standardization, Acoustics – Determination of Sound Power Levels of Noise Sources – Survey Method, ISO 3746:1979

[34] N. Curle, The influence of solid boundaries upon aerodynamic sound, In: Proceedings of the Royal Society of London, Series A, Mathematical and Physical Sciences, Vol. 231, No. 1187, 1955, pp. 505-514

[35] E. Johansson, Aeroacoustic study on the roofbar of a truck using CFD, MSc thesis, Chalmers University of Technology, Gothenburg, Sweden, 2013

[36] J. Tell, Aeroacoustic study on roof bow – CFD generation of input data for hybrid approach, MSc thesis, Chalmers University of Technology, Gothenburg, Sweden, 2012

[37] X. Gloerfelt, Cavity Noise, In: VKI Lectures: Aerodynamic Noise from Wall-Bounded Flows, Von Karman Institute, 2009

[38] J. E. Rossiter, Wind Tunnel Experiments on the Flow over Rectangular Cavities at Subsonic and Transonic Speeds, RAE TR 64037, Royal Aircraft Establishment, Farnborough, United Kingdom, 1964

[39] L. F. East, Aerodynamically Induced Resonance in Rectangular Cavities, Journal of Sound and Vibration, Vol. 3, No. 3, 1966, pp. 277-287

[40] P. J. W. Block, Noise Response of Cavities of Varying Dimensions at Subsonic Speeds, Technical Paper D-8351, NASA Langley Research Center, Hampton, VA, 1976

[41] F. M. White, Fluid Mechanics, 7th ed., McGraw-Hill, New York, 2009, 862 p.

[42] H. Ahlstedt, Kitkallinen virtaus, Course handout, Tampere University of Technology, Department of Energy and Process Engineering, 2012

[43] ANSYS Fluent Theory Guide, Release 17.0, ANSYS, Inc., Southpointe 2600 ANSYS Drive Canonsburg, PA 15317, January 2016

[44] F. R. Menter, Zonal Two Equation k- Turbulence Models for Aerodynamic Flows, AIAA Paper 93-2906, 1993

APPENDIX A. MATLAB PROGRAM

This appendix describes how the flow rate is calculated from the measurement data using MATLAB.

```
d = 0.030;          % Orifice diameter
D = 0.0515;         % Upstream internal pipe diameter
beta = d/D;         % Diameter ratio
kappa = 1.4;        % Isentropic exponent of the gas

L1 = 1.0;           % Relative pressure tapping spacings L1 and L2
L2 = 0.47;

cDATA = [d; D; kappa; L1; L2];

mDATA = xlsread('kp6s1.xlsx');   % Measurement data

mDATArows = size(mDATA,1);

RESULTS = zeros(mDATArows,6+8);

qm_guess = 1e-3;               % Initial guess for mass flow rate (kg/s)


for i = 1:mDATArows

f = @(qm) myfun(qm,cDATA,mDATA(i,:));  % Function handle for fsolve

[qm, fval] = fsolve(f,qm_guess);       % Nonlinear system solver

p       = mDATA(i,2);
dp_orif = mDATA(i,3);
T       = mDATA(i,5);
RH      = mDATA(i,6);

ReD = (4*qm/(pi*mu(T)*D));

RESULTS(i,1:6) = mDATA(i,:);
RESULTS(i,7) = coeff_C(beta, ReD, L1, L2);       % Discharge coefficient
RESULTS(i,8) = epsilon(beta,kappa,dp_orif,p);    % Expansion factor
RESULTS(i,9) = mu(T);                            % Dynamic viscosity
RESULTS(i,10) = fval;                            % fsolve function value
RESULTS(i,11) = ReD;                             % Reynolds number
RESULTS(i,12) = rho_humidair(p,T,RH);            % Desity of humid air
RESULTS(i,13) = qm;                              % Mass flow rate
RESULTS(i,14) = qm/rho_humidair(p,T,RH);         % Volume flow rate

end
```

```
function F = myfun(qm,cDATA,mDATA)

% Input constant data (cDATA)
d = cDATA(1);
D = cDATA(2);
kappa = cDATA(3);
L1 = cDATA(4);
L2 = cDATA(5);

beta = d/D;                 % Diameter ratio
E = (1-beta^4)^(-1/2);      % Velocity of approach factor

% Input measurement data (mDATA)
p       = mDATA(2);
dp_orif = mDATA(3);
T       = mDATA(5);
RH      = mDATA(6);

F = qm - coeff_C(beta,(4*qm/(pi*mu(T)*D)),L1,L2)*E..
    *epsilon(beta,kappa,dp_orif,p)*(pi/4)*(d^2)..
    *sqrt(2*dp_orif*rho_humidair(p,T,RH));

end
```

```
function C = coeff_C (beta, ReD, L1, L2)

    if (L1 >= 0.4333)

        C = 0.5959 + 0.0312*beta^2.1 - 0.1840*beta^8...
            + 0.0029*beta^2.5*(10^6/ReD)^0.75...
            + 0.090*L1*0.0390 - 0.0337*L2*beta^3;

    else

        C = 0.5959 + 0.0312*beta^2.1 - 0.1840*beta^8...
            + 0.0029*beta^2.5*(10^6/ReD)^0.75...
            + 0.090*L1*beta^4*(1-beta^4)^(-1) - 0.0337*L2*beta^3;
    end

end
```

```
function eps = epsilon(beta, kappa, dp_orif, p)

% Expansibility (expansion) factor
% This formula is applicable only within the range of the limits of use.

eps = 1 - (0.41 + 0.35*beta^4)*dp_orif/(kappa*p);

end
```

```
function rho = rho_humidair(p,T,RH)

% The function calculates the density of humid air as a mixture of ideal
% gases when air pressure, temperature and relative humidity are known.

% Input arguments:
% p = Pressure (Pa)
% T = Temperature (°C)
% RH = Relative humidity (%)


Md = 0.028964;              % Molar mass of dry air (kg/mol)
Mv = 0.018016;              % Molar mass of water vapor (kg/mol)
R = 8.314;                  % Universal gas constant (J/(K*mol))

pv = (RH/100)*p_sat(T);     % Pressure of water vapor (Pa)
pd = p - pv;                % p_sat(T) = Saturated vapor pressure (Pa, °C)
                            % Partial pressure of dry air (Pa)

T = T + 273.15;             % Conversion to Kelvin from °C

rho = (pd*Md + pv*Mv)/(R*T);

end
```

```
function viscosity = mu(T)

% The dynamic viscosity of an ideal gas as function of temperature.

% Sutherland, W. (1893), "The viscosity of gases and molecular force",
% Philosophical Magazine, S. 5, 36, pp. 507-531 (1893).

T = T + 273.15;             % Temperature conversion to K

T_ref = 273.15;             % Reference temperature (K)
mu_ref = 1.716*10^(-5);     % Viscosity at T_ref (kg/ms)
S = 110.4;                  % Sutherland temperature (K)

viscosity = mu_ref*(T/T_ref)^(3/2)*(T_ref + S)/(T + S);

end
```

```
function p = p_sat(T)

% Buck equation for saturated vapor pressure, over liquid water, T > 0 °C
% [T] = °C
% [p] = Pa
% Buck (1996), Buck Research CR-1A User's Manual, Appendix 1. (PDF)

p = 0.61121*exp((18.678 - T/234.5)*(T/(257.14 + T)));
p = p*1000;         % Unit conversion from kPa to Pa

end
```